1-1-2012

Experiments and Simulation for 6061-T6 Aluminum Alloy Resistance Spot Welded Lap Joints

Radu Stefanel Florea

Experiments and simulation for 6061-T6 aluminum alloy resistance spot welded lap joints

By

Radu Stefanel Florea

A Dissertation
Submitted to the Faculty of
Mississippi State University
in Partial Fulfillment of the Requirements
for the Degree of Doctor of Philosophy
in Mechanical Engineering
in the Department of Mechanical Engineering

Mississippi State, Mississippi

December 2012

Experiments and simulation for 6061-T6 aluminum alloy resistance spot welded lap joints

By

Radu Stefanel Florea

Approved:

Douglas J. Bammann Professor of Mechanical Engineering (Director of Dissertation)	Steve D. Daniewicz Professor of Mechanical Engineering (Committee Member)
Mark F. Horstemeyer Professor of Mechanical Engineering (Committee Member)	Youssef Hammi Assistant Research Professor of Center for Advanced Vehicular Systems (Committee Member)
Kiran N. Solanki Assistant Professor of School for Engineering of Matter, Transport, and Energy Arizona State University (Committee Member)	Kalyan K. Srinivasan Assistant Professor of Mechanical Engineering (Graduate Coordinator)
Sarah A. Rajala Professor and Dean of the Bagley College of Engineering	

Name: Radu Stefanel Florea

Date of Degree: December 15, 2012

Institution: Mississippi State University

Major Field: Mechanical Engineering

Major Professor: Douglas J. Bammann

Title of Study: Experiments and simulation for 6061-T6 aluminum alloy resistance spot welded lap joints

Pages in Study: 126

Candidate for Degree of Doctor of Philosophy

This comprehensive study is the first to quantify the fatigue performance, failure loads, and microstructure of resistance spot welding (RSW) in 6061-T6 aluminum (Al) alloy according to welding parameters and process sensitivity. The extensive experimental, theoretical and simulated analyses will provide a framework to optimize the welding of lightweight structures for more fuel-efficient automotive and military applications.

The research was executed in four primary components. The first section involved using electron back scatter diffraction (EBSD) scanning, tensile testing, laser beam profilometry (LBP) measurements, and optical microscopy(OM) images to experimentally investigate failure loads and deformation of the Al-alloy resistance spot welded joints. Three welding conditions, as well as nugget and microstructure characteristics, were quantified according to predefined process parameters. Quasi-static tensile tests were used to characterize the failure loads in specimens based upon these same process parameters. Profilometer results showed that increasing the applied welding

current deepened the weld imprints. The EBSD scans revealed the strong dependency between the grain sizes and orientation function on the process parameters.

For the second section, the fatigue behavior of the RSW'ed joints was experimentally investigated. The process optimization included consideration of the forces, currents, and times for both the main weld and post-heating. Load control cyclic tests were conducted on single weld lap-shear joint coupons to characterize the fatigue behavior in spot welded specimens. Results demonstrate that welding parameters do indeed significantly affect the microstructure and fatigue performance for these welds.

The third section comprised residual strains of resistance spot welded joints measured in three different directions, denoted as in-plane longitudinal, in-plane transversal, and normal, and captured on the fusion zone, heat affected zone and base metal of the joints. Neutron diffraction results showed residual stresses in the weld are approximately 40% lower than the yield strength of the parent material, with maximum variation occurring in the vertical position of the specimen because of the orientation of electrode clamping forces that produce a non-uniform solidification pattern.

In the final section a theoretical continuum modeling framework for 6061-T6 aluminum resistance spot welded joints is presented.

DEDICATION

I dedicate this to my family who supported me in countless ways.

ACKNOWLEDGEMENTS

I would like to thank Dr. Douglas J. Bammann for his assistance and guidance toward completion of this dissertation. Also, I would like to thank Dr. Daniewicz, Dr. Horstemeyer, Dr. Solanki and Dr. Hammi for their technical advice and for their helpful comments on the dissertation.

The author would like to thank the Center of Advanced Vehicular Systems (CAVS) and the U.S. Army-TARDEC for supporting this work. This material is based upon work supported by the U.S. Army TACOM Life Cycle Command under Contract No. W56HZV-08-C-0236, through a subcontract with Mississippi State University, and it was performed for the Simulation Based Reliability and Safety (SimBRS) research program. Any opinions, findings and conclusions or recommendations expressed in this material are those of the author(s) and do not necessarily reflect the views of the U.S. Army TACOM Life Cycle Command.

The author specifically acknowledges Camden Hubbard, Paris Cornwell, Brian Cady and Thomas Watkins of ORNL for their support.

Special thanks to James Cruz at Edison Welding Institute for his expertise in manufacturing coupons used in this study, and to Crawford Baird, Heather Wainwright, Will Wittington, Steven Horstemeyer and Andrew Yedell at CAVS for their help.

Also, the author expresses his appreciation to Dr.Yoni Adoni and Dr. Matthew Castanier for their technical expertise.

TABLE OF CONTENTS

LIST OF TABLES

LIST OF FIGURES

CHAPTER I

INTRODUCTION

Summary

This study offers a novel, comprehensive research approach to compare weld quality for different welding conditions in order to achieve optimal end-product results. More specifically, it is the first to quantify the fatigue performance, failure loads, and microstructure of resistance spot welding (RSW) in 6061-T6 aluminum (Al) alloy according to welding parameters and process sensitivity. The extensive experimental, theoretical and simulated analyses will provide a framework to optimize the welding of lightweight structures for more fuel-efficient automotive and military applications.

The research was executed in four primary components. The first chapter describes using electron back scatter diffraction (EBSD) scanning, tensile testing, laser beam profilometry (LBP) measurements, along with optical microscopy (OM) images to experimentally investigate failure loads and deformation of 6061-T6 aluminum alloy resistance spot welded joints. Three welding conditions, nugget and microstructure characteristics were quantified according to predefined process parameters. Quasi-static tensile tests were used to characterize the failure loads in specimens based upon these same process parameters. Profilometer results showed that increasing the applied welding current deepened the weld imprints. In addition, good correlation was obtained between

the EBSD scans and the welding conditions. The EBSD scans revealed the strong dependency between the grain sizes and orientation function on the process parameters.

Chapter 2 explains how the fatigue behavior of RSW in aluminum 6061-T6 alloy was experimentally investigated. Three welding conditions, denoted as “nominal,” low” and “high,” were studied to determine the microstructure of the weld nuggets. The process optimization included consideration of the forces, currents and times for the main weld and post-heating. After successive iterations were completed and “witness samples” collected, the optimum welding parameters were determined. Load control cyclic tests were then conducted on 2 mm-thick single-weld lap-shear joint coupons to characterize the microstructure and fatigue behavior of spot welded specimens, and thereby elucidate the influence of the process parameters. This work revealed that the welding process parameters indeed have a great influence on both the microstructure and fatigue life properties of the aluminum sheet resistance spot welds.

As revealed in Chapter 3, residual strains of resistance spot welded joints of 6061-T6 aluminum alloy sheets were measured in three different directions denoted as in-plane longitudinal, in-plane transversal, and normal. The welding process parameters were established to meet or exceed MIL-W-6858D specifications (i.e., approximately 5.7 mm weld nugget and minimum shearing force of 3.8 kN per weld confirmed via quasi-static tensile testing). EBSD and OM were performed to determine grain size and orientation. The residual stress measurements were taken at a series of points along the weld centerline at depths corresponding to the weld mid-plane and at both 1 mm below the top surface of the plate and 1 mm above bottom surface. The residual stresses were captured on the fusion zone (FZ), heat affected zone (HAZ), and base metal (BM) of the resistance

spot welded joint. Neutron diffraction results show residual stresses in the weld are approximately 40% lower than yield strength of the parent material. The maximum variation in residual stresses occurs, as expected, in the vertical position of the specimen because of the orientation of electrode clamping forces that produce a non-uniform solidification pattern. Despite the high anisotropy of the welding nugget and surrounding area, a significant result is that normal measured stress values are negligible in both the horizontal and vertical directions of the specimen.

In Chapter 5, a theoretical continuum modeling framework for 6061-T6 aluminum resistance spot welded joints is presented.

Intellectual Merit

This study will provide industry and academia a theoretical and experimental knowledge base for 6061-T6 aluminum resistance spot welded joints. The scientific contributions of this work include the quantification of the electrode imprint using laser profilometry as well as the establishment of consistency in failure loads as a function of different welding conditions. Furthermore, this study offers microstructure quantification of the spot welds as way to understand the effect of the welding parameters on the quasi-static tensile behavior of the resistance spot welded lap-joints.

This work is the first of its kind to quantify the fatigue performance, failure loads, and microstructure of RSW in 6061-T6 aluminum alloy according to the welding parameters and process sensitivity. Results demonstrate that welding parameters do indeed significantly affect the microstructure and fatigue performance for these welds.

Limited results are reported on residual stress measurements for this type of weld, and to the author's best knowledge, 6061-T6 aluminum resistance spot welded joints have not been studied by the scientific community.

Broader Impact

The automotive and military industries will be the primary beneficiary of this research work. The need for lightweight alloys and quality welding is a priority in these industries for improving ground vehicle fuel economy, but significant economic and technical barriers impede development of lightweight materials for this purpose. Therefore, the extensive experimental, theoretical and simulated analyses of this project will provide a framework to improve the welding of lightweight structures for more fuel-efficient automotive and military applications.

Dissertation Structure

Chapter 1 describes the motivation for this work and introduces the concept of the dissertation. Chapter 2 describes the failure loads and deformation for resistance spot welding (RSW) of 6061-T6 aluminum using quasi-static tensile tests, laser beam profilometry, and electron back scatter techniques. Chapter 3 is a study on fatigue life and microstructure in RSW single lap joints. Chapter 4 quantifies residual stresses in RSW'ed coupons via neutron diffraction measurements. Chapter 5 describes theoretical workframe and computational results. Chapter 6 is a summary of the work and recommendations for future research direction related to this topic.

CHAPTER II

RESISTANCE SPOT WELDING OF 6061-T6 ALUMINUM: FAILURE LOADS AND DEFORMATION

Introduction

This study offers a novel research approach to compare weld quality for different welding conditions in order to achieve optimal end-product results. Using electron back scatter diffraction (EBSD) scanning, tensile testing, and laser beam profilometry (LBP) measurements along with optical microscopy (OM) images, failure loads and deformation of 6061-T6 aluminum alloy, resistance spot welded (RSW) joints were experimentally investigated. Three welding conditions, nugget and microstructure characteristics were quantified according to predefined process parameters. Quasi-static tensile tests were used to characterize the failure loads in specimens based upon these same process parameters. Profilometer results showed that the larger the applied welding current, the deeper the weld imprints. In addition, good correlation was obtained between the EBSD scans and the welding conditions. A strong dependency was found between the grain size and orientation and the welding parameters.

Manufacturing industries currently seek to better understand the complicated microstructural changes that occur in crystalline materials during welding operations. These welding operations often involve high strains and deformation temperatures that result in microstructures which continually evolve away from that of the base material. A

non-homogeneous distribution of the material microstructure often exists due to the non-uniform distribution of temperatures and strains inherent during most joining operations, such as resistance spot welding (RSW). The residual microstructures present in crystalline materials post-welding influence the overall strength and performance of the manufactured components. Therefore, understanding the influence of welding process parameters, such as force, weld time, and current, on microstructural changes provides manufacturers with opportunities to optimize the welding processes in order to achieve the most desirable material properties and microstructures for their end-products.

Concurrent to manufacturing industries' efforts to optimize welding processes, transportation industries seek to address energy and emission concerns through wide-spread use of lightweight metals like aluminum alloys to decrease the weight of the vehicles they produce. Essential to maximizing the weight reduction derived from these lightweight components is decreasing welding post-processing costs, and specifically avoiding the necessity for excessive sanding and painting processes needed to ensure acceptable appearance of the final product. In fact, resistance spot welding produces sufficient joints to successfully mitigate the need for extensive post-processing.

Resistance spot welding (RSW) is a joining process for thin metal sheets during which, in contrast to other welding processes, no filler metals or fluxes are used. Instead, pressure exerted by electrodes joins the contacting metal surfaces via heat obtained from resistance to the electrical current flow**.** RSW provides accelerated speed and adaptability for automation in high-volume and high-rate production; however, the technique suffers from inconsistent quality between welds due to the complexity of the process itself and many variables involved in the joining process. Further implementation and improvement

of existing processes, including weld quality and time improvement, electrode life extension, maintenance cost reduction and development of new techniques for RSW, will greatly impact the above noted industries due to the large numbers of spot welds they perform in their manufacturing processes [1, 2].

The complexity of optimizing RSW process arises from the integration of mechanical, metallurgical, thermal and electrical phenomena. The interaction between thermal and metallurgical phenomena results in a continually evolving microstructure. Second, thermal and mechanical phenomena result in non-uniform thermal strains and residual stresses. Electrical and thermal effects strongly correlate and involve high temperature gradients and non-uniform weld strength. From metallurgy and mechanical perspectives, complex interactions between the base metal (BM), heat affected zone (HAZ) and fusion zone (FZ) involve non-homogeneous distribution of the material microstructure. The interactions between electrical and mechanical effects refer to contact conditions between electrodes and welding sheets. Considering these sometimes divergent factors, it is difficult to computationally simulate and measure the performance of RSW in different joints, materials and applications. However, experimental studies [3-5], have been executed on various engineering materials, and the influence of the welding time, current, and applied forces has been evaluated accordingly. In addition, numerical and FEA studies have been conducted [6-11] to explore methods and resolve the effect of various welding parameters. Despite progress made toward the complexities of the RSW process, we still lack a clear understanding of the phenomena that occur in RSW.

In order to maximize the use of RSW in high conductivity metals like aluminum, optimization of resistance spot welding (RSW) is needed to reduce production cost and to

enhance efficiency and quality. Notably, RSW of aluminum is more complex than it is with steel because of aluminum's higher thermal conductivity requires higher power and current requirements. As such, the experimental and modeling techniques for aluminum welding are more complex as well. This paper investigates the experimental RSW parameters for an aluminum 6061-T6 (AlMg1SiCu per ISO nomenclature) alloy spot welded in a lap-joint configuration. The scientific contributions of this work include the quantification of the electrode imprint using laser profilometry as well as the establishment of consistency in failure loads as a function of different welding conditions. Furthermore, this study offers microstructure quantification of the spot welds as way to understand the effect of the welding parameters on the quasi-static tensile behavior of the RSW'ed lap-joints.

Materials and Experiments

The wrought aluminum 6061-T6 alloy used in this study exhibits high yield strength and good ductility properties [3, 18-19]. Material thickness is 2 mm and each sheet comprises two pieces, 100 mm long and 35 mm wide. The uncoated sheets overlap 35 mm with one spot weld located in the center of the overlap. From a welding perspective, aluminum and magnesium are considered Group 1 materials [3, 13] and require special procedures for oxide coating removal, cleaning, fit-up and joint thickness. As such, prior to welding, each sheet of aluminum alloy was mechanically and chemically cleaned to remove the natural oxide layer. In order to provide relevant results for industry, lap-shear coupons were produced to meet or exceed MIL-W-6858D Military Specification [3, 13], where the minimum nugget size is 5.7 mm and minimum shearing force is 3.8 kN per weld.

A servo-gun with weld control was used to manufacture the specimens for this study, and copper-zirconium alloy electrodes were used to join the aluminum sheets. The power supply and current transformer had a mid-frequency direct current with 8V on the secondary voltage. Water was applied as a cooling agent at a rate of 4 liters/minute. Welded specimens of various nugget sizes were produced. Florea et al. [3, 17] described in detail the equipment used in this study, which is capable of the weld-and-forge operation for reducing the porosity and solidification cracking prevalent when aluminum alloys are RSW'ed. To meet the metallographic requirements, three iterations of welding were performed in order to identify the most suitable welding condition. To confirm the quality during specimen manufacturing, periodic peel tests were performed after each batch of 20 specimens. Following the production of the samples at "nominal" condition, the weld time and/or weld current were adjusted to "low" condition for producing slightly smaller (average 4.5 mm) and to "high" condition for slightly larger (average 6.5 mm) weld nuggets [3]. During the welding process, the electrodes were re-dressed at intervals of approximately every 100 welds. Table 2.1 lists the weld parameters for "low", "nominal", and "high" conditions.

Following each test cycle, a laser profilometer was used to non-destructively examine the welds on nine coupons, three at each welding condition. To assure measuring consistency, consecutive specimens were analyzed (for example coupon #96, #97 and #98). The samples were scanned in x- and y-directions, 20 mm by 20 mm at the top and bottom of the resistance spot welds. The measuring speed was 30 mm/second with 100 microns spacing and a resolution of 130-150 points. After proper focus, the z-coordinate was constantly maintained and the laser scan moved along the other two axes.

This technique provided information about the weld profiles and nugget areas, the volume of a dimple or a peak, as well as the 3D axonometric meshes.

Cross-sections of the weld nugget were made at each of the three conditions and were prepared for optical microscopy (OM) analysis. After cutting, the coupons were hot mounted in resin powder and then mechanically ground and polished. After polishing, the coupons were etched using Keller's reagent (95mL water, 2.5mL HNO3, 1.5mL HCl and 1.0mL HF). De-ionized water and ethanol were used to neutralize the coupons after etching. All samples were then cleaned for 20 minutes in an ultrasonic bath using ethanol, then dried and placed in a desiccator until microscopy analysis.

In order to quantify the microstructure of each set of welding parameters, electron back scatter diffraction (EBSD) mapping was performed. To reduce EBSD scan time, each cross section was analyzed by scanning half of the weld nugget in the longitudinal direction (in the rolling direction). "Grain dilution clean-up" function was performed with 5 degrees tolerance angle and 2 microns minimum grain size.

For tensile tests, a mechanical testing apparatus was used along with a laser extensometer at 50 mm at full-scale gage length. Force, displacement, and time were captured. The displacement rate was 0.01 mm/seconds, and failure was defined as a 20% drop in the peak load. Ten specimens were tensile tested as follows: three at nominal condition (30 kA current), four at low condition (26 kA), and three at high condition (38 kA). Complete failure of all specimens was observed.

Results and Discussion

Laser Beam Profilometry

One of the main objectives of this study was to quantify the weld indentation depths that occurred on specimens subjected to different forces and electric currents. In RSW, as the current increases, the indentation produced on the surface of the sheet deepens. In order to check the quality and the appearance of the welds, the maximum and mean average depths and heights of the indentations were measured using laser beam profilometry (LBP) for nine specimens at the three different welding conditions. The maximum average depth for the "high" weld condition was 0.128 mm, which is necessary to achieve the smooth profile required to avoid post-welding and pre-coating surface preparation.

Notably, the LBP technique is frequently used in corrosion science to measure weight loss of corrosive environments [14]; however, to the best of the authors' knowledge, it has not used in quantifying resistance spot welds. Nonetheless, using Talysurf profilometer scanning to determine whether a weld is acceptable or not, can be achieved without doing an expensive destructive test. Furthermore, as an alternative solution to ultrasonic testing (UT), LBP precludes the necessity for sample preparation. Specifically, in UT tests the transducer is typically separated from the test object by a medium such as oil. The oil film increases the efficiency of the process by reducing the losses in the ultrasonic wave energy because of the separation between the surfaces. LBP, on the other hand, does not require the oil film, which eliminates that cost as well as the chemical contamination of the welds. In addition, no further cleaning process is required

after LBP testing. Considering the economy and integrity of LBP, this technique proved adaptable for the examination of the RSW-joined specimens.

LBP analysis can provide useful information regarding not only RSW joint integrity and appearance, but also process optimization, particularly in regard to analyzing electrode efficacy and life expectancy. As William and Parker [1, 2] emphasized, life of the welding electrodes is, indeed, another important issue in RSW. Both the life span of the electrodes and the required shut-down times for their maintenance impact production efficiency and cost. Specifically, the greater the heat input, welding time, and electrode force, the shorter the electrode life expectancy, where deterioration of the electrodes is manifested by growth of electrode tip diameter. Furthermore, when more welds are performed under "high" condition, the electrodes will, in turn, need more frequent maintenance (re-dressing or replacing). Thus the LBP analysis can be used to determine when the electrodes require re-dressing and or maintenance through detection of weld deterioration and excessive spatter.

Figure 2.1 shows the axonometric meshes produced by the laser profilometer for 26 kA, 30 kA, and 38 kA electric current. The areas of dark blue indicate the depth of the welding imprint while the red areas indicate height. The top welds are illustrated in the left side of the figure, and the bottom welds are on right side. While the electrode forces used in the welding were identical for each of the specimens, the current ranged from 26 kA to 38 kA. Figure 2.1 also illustrates the maximum and mean heights and depths that were measured on three different specimens for each welding conditions. This technique generated 2D mapping plots and 1D profiles (cross-section cuts to capture maximum

depths and heights), and provided a valuable indication of critical stress concentration areas due to the irregularities in welded coupons.

Figure 2.2a reveals the trend of the mean average depth and heights for the top surface of the spot welds. The mean depth varies linearly, while the mean average height remains constant. This indicates that the depth of the indentation is directly proportional to the applied current when the electrodes are maintained at a constant force. The relationship of the mean depth and height of the bottom part of the joints (Figure 2.2b) displays a non-linear relationship with respect to current. The main explanation for this randomness is the irregular profile of the welding spatter from the joining process.

Figures 2.1 and 2.2 clearly demonstrate that the welding current is an important factor in the strength and appearance of welded joints. The higher the current, the higher the generated heat input. The input heat melts/softens the welding sheets and, if the electrode force remains constant, the imprint is deeper. Not surprisingly, the structural integrity of the joint may be affected if the electrical current is incorrectly increased to an excessively high value (40-45 kA) because of the creation of stress concentrators and the decreasing of the weld cross-sectional area. A spike in electrical current creates a large imprint and a potential burn-through effect on thin metal plates. Also, the appearance of the welds is important, particularly on the high condition where the spatter is excessive, which then leads to unwanted post weld processing, such as sanding, to eliminate weld imperfections [12].

Quasi-static Tensile Tests

Figure 2.3 presents the representative results of the lap-shear tests for the low, nominal, and high weld conditions. The results of the lap-shear tests on the specimens

representing the three weld conditions show that the static behavior is consistent from sample to sample at each condition. In regard to Military specifications [13], the results are satisfactory at "high" condition but poor at "low" condition. Specifically**,** the high condition welds were stronger than the nominal or low condition welds. The RSW coupons were observed to fail in an interfacial fracture mode for all three welding conditions. The interfacial fracture mode is consistent with experimental observations reported elsewhere [15, 16] and is likely a result of 6061 aluminum alloy's low ductility. Figure 2.4 shows the top surface of untested coupons along with representative fracture surfaces of the failed coupons. As shown in Figure 2.4, the RSW failure mode under static loading is characterized by a non-uniform surface area with no button visible. In addition, the fracture surface contains a distinctive granular surface over the entire weld area and no partial thickness fracture is visible. These fracture characteristics observed here are consistent with standard quasi-static fracture modes of RSW reported elsewhere [15, 22].

Electron Back Scatter Diffraction Results

Figure 2.5 shows the Electron Back Scatter Diffraction (EBSD) mapping of the grain size and orientation due to the recrystallization process for the fusion zones (FZ), heat affected zones (HAZ), and base metals (BM) of the specimens from each of the three welding conditions. From the scans, the grain orientation toward the center-line of the nugget is visible where the increased temperature and squeezing forces create the observed grain structure. In the FZ, the grain size decreases, but in the HAZ, the grain size increases. These changes in grain size are due to the high cooling rate during the transition from liquid metal to solid in the FZ, as opposed to the residual heat experienced

in the HAZ, which leads to grain growth. While the grain orientation had a uniform pattern for nominal and high conditions, it had a random pattern for the low condition due to insufficient heat input in the welding process at this condition. When the electric current has high values, the heat input is higher which is directly proportional to the square root of the current value. This in turns affects the cooling rate and consequentially the grain size.

The average grain size for each scanned area along with the entire microstructure differs significantly depending upon presented welding conditions, as shown in Figure 5. Figure 2.6 illustrates the dependency of grain size function on welding conditions. The dependency trend is linear for FZ, and a second order polynomial fits the trend for the HAZ. In the HAZ and FZ, the grain size and shape changed significantly with the heat input: the more heat in the FZ, the smaller the grains. In the high condition welding, grain size decreased to 7.82 microns in the FZ. The largest mean grain size is 29.45 microns and was measured in HAZ at the low welding condition. In addition, for the low welding condition, the transition between the different zones is not smooth, which decreases the weld quality and failure loads. For the BM, the mean grain size has only a slight variation, as expected, and was found to be approximately 16 microns. The measured average grain size in the BM is consistent with the literature for hot rolled 6061-T6 aluminum alloy [20]. Lastly, the standard deviation for these grain sizes measured from 8.2 to 29.0 microns (from low to high welding conditions), which is an indicator of the width of the distribution (scatter) of the average value, in this case grain size, for the different welding conditions and zones [23].

Conclusions

This study reveals that the welding process parameters have a great influence in the quality of the RSW joints. With successive iterations and collected "witness samples," the optimum current, force and time for resistance spot welding 6060-T6 aluminum alloy were determined.

Profilometer results clearly indicate that the larger the current, the deeper the weld imprints. As expected, the optimum quality of weld is at "nominal" condition. By slightly changing the process parameters from nominal, the profile appearances for the top and bottom of the produced welds are less than acceptable. Furthermore, it was found that the depth of the top part of the resistant spot welds varies linearly with respect to the applied electric current.

Based on the quasi-static tests, we can conclude that if the welding parameters are correctly established, consistency in static failure loads is achieved. As such, good correlation between the EBSD scans and the welding conditions were observed. The EBSD scans for welds show the strong dependency between the grain sizes and orientation function on the process parameters. Lower heat input created random microstructure and weaker welds, while the "nominal" and "high" conditions produced smooth transitions between the welding zones and larger failure loads. High values for the standard deviation in the "low" condition case indicate insufficient electric current and energy input to produce satisfactory welds.

Table 2.1 Weld parameters for “low”, “nominal”, and “high” conditions.

Welding condition	Electrode Force (kN)	Welding Time (sec)	Welding Current (kA)	Average Nugget Size (mm)
“Low”	3.8	0.115	26	4.5
“Nominal”	3.8	0.115	30	5.7
“High”	3.8	0.115	38	6.5

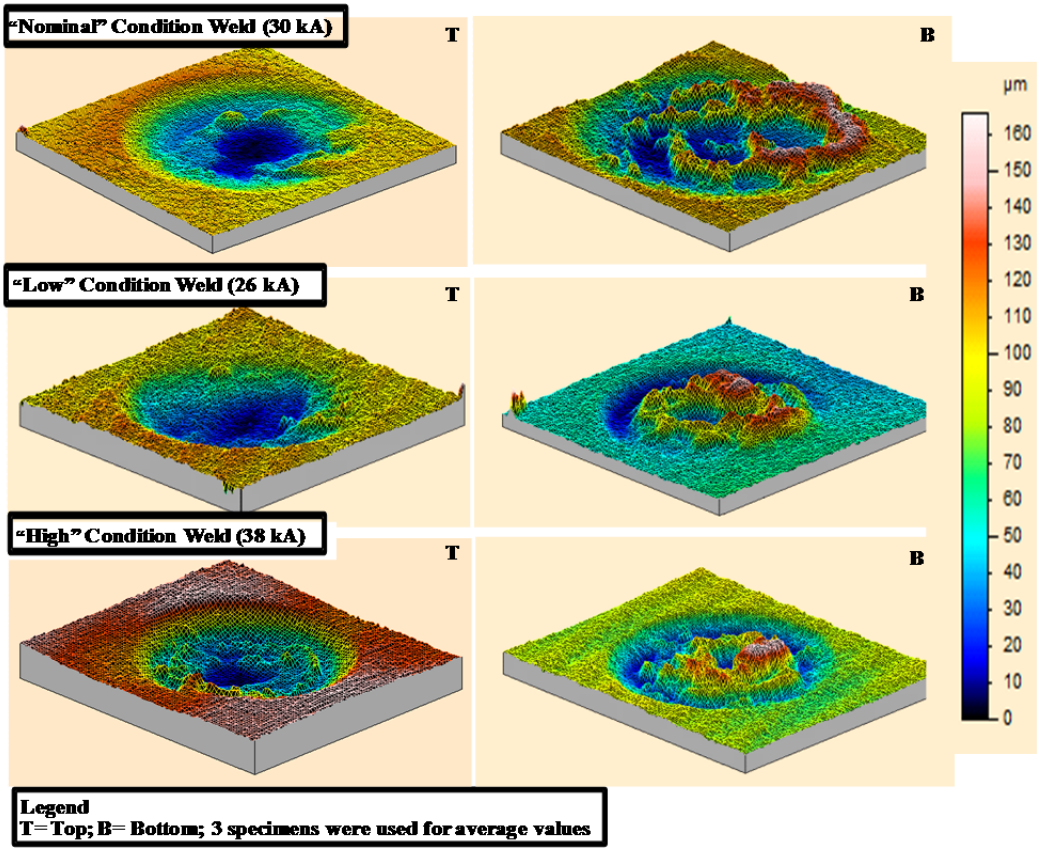

Figure 2.1 Axonometric 3D weld profiles for top and bottom welds at “nominal,” “low,” and “high” conditions.

The dark blue indicates depth, while the red and pink indicate height. The electrode depth imprint is the largest for the “high” condition weld. The scanned surface was 20 mm by 20 mm.

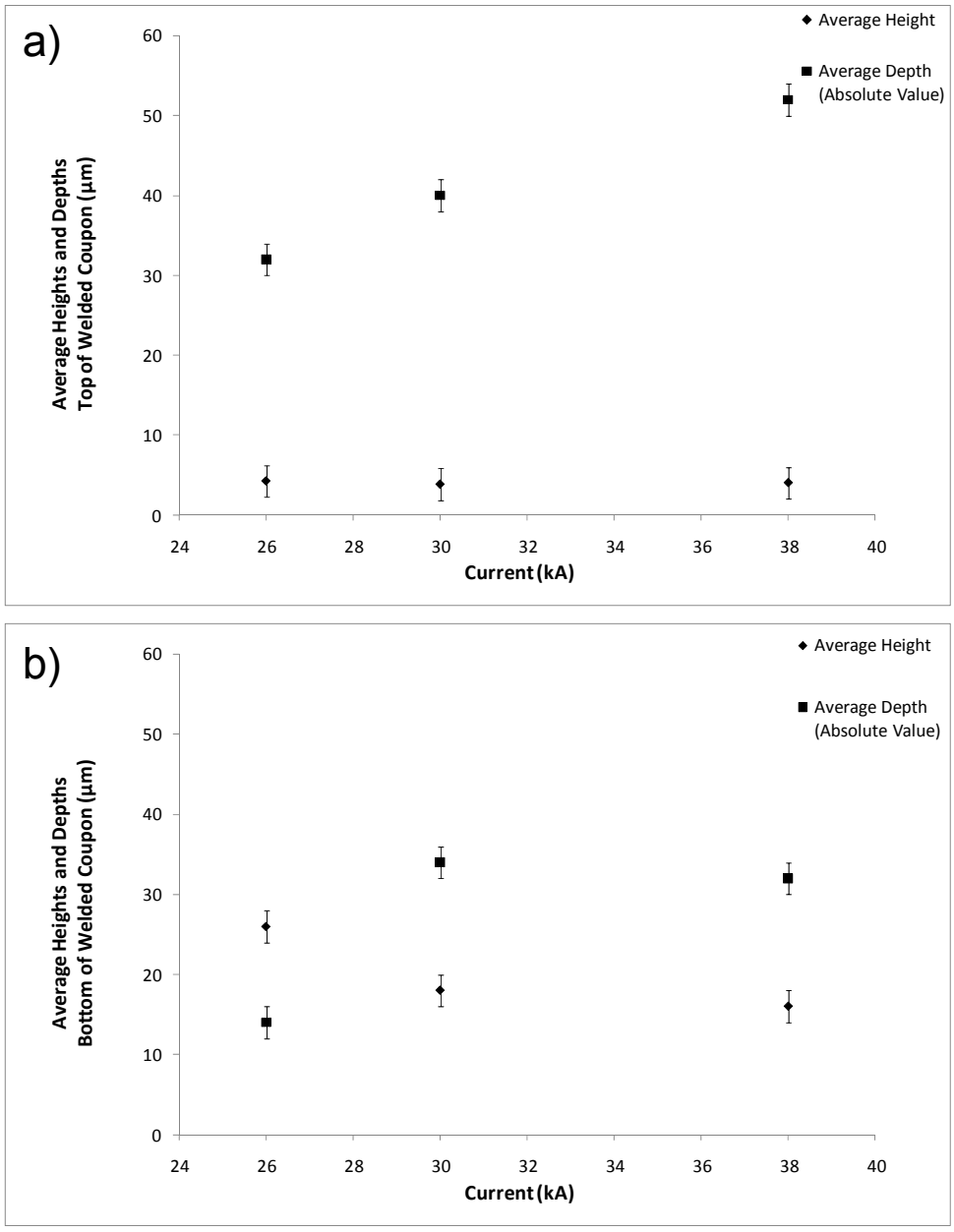

Figure 2.2 Average heights and depths for the different weld conditions

Mean averages were plotted for tops (a) and bottoms (b) of resistance spot welded joints as a function of current (kA). The indentation depth on the plot (a) is increasing linearly with respect to the applied amperage. The average height is almost constant (3-4 µm). Plot (b) cannot be described in a linear manner and presents a random tendency due to spatter from the weld process. The dependency trend is a second order polynomial fits.

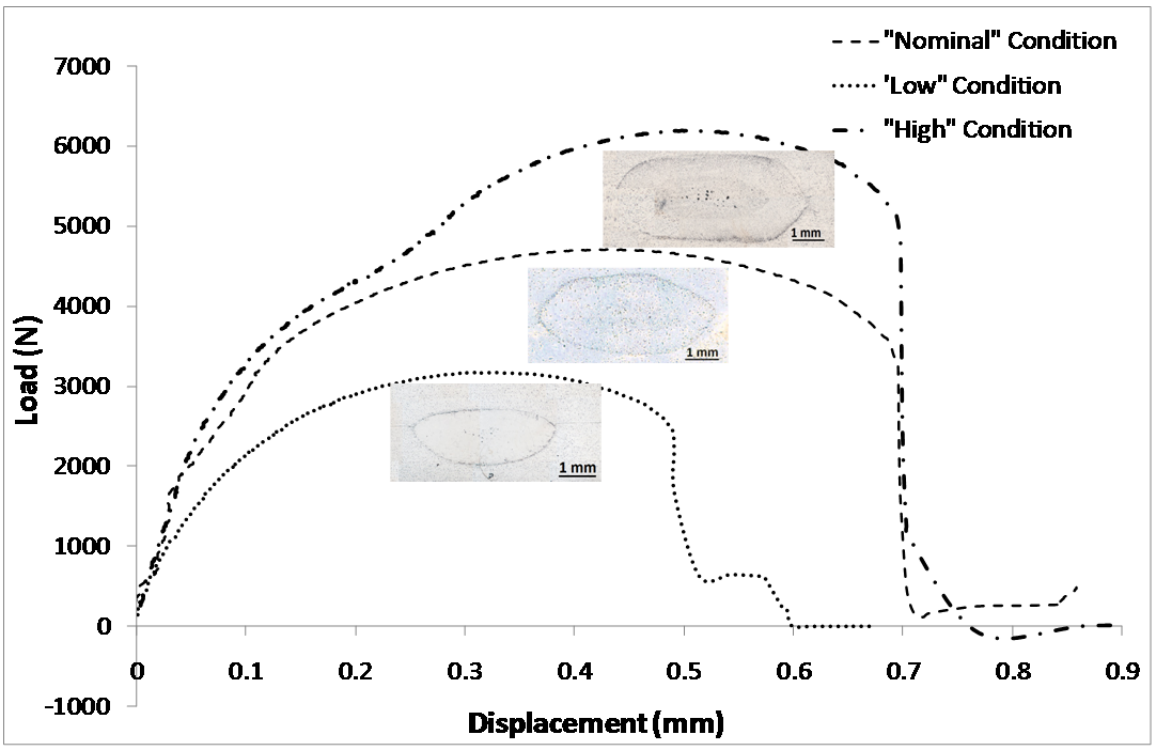

Figure 2.3 Load versus displacement graphs showing the consistency for "nominal," "low" and "high" conditions

The displacement rate was 0.01 mm/second and complete failure was observed at 20% of peak load "drop" setting. More welding defects were observed for the "high" condition, while for "low" condition, the nugget size and failure load did not meet MIL Specs. The "nominal" condition welds were acceptable and met MIL-W-6858D specifications (approximately 5.7 mm weld nugget and 3.8kN failure load).

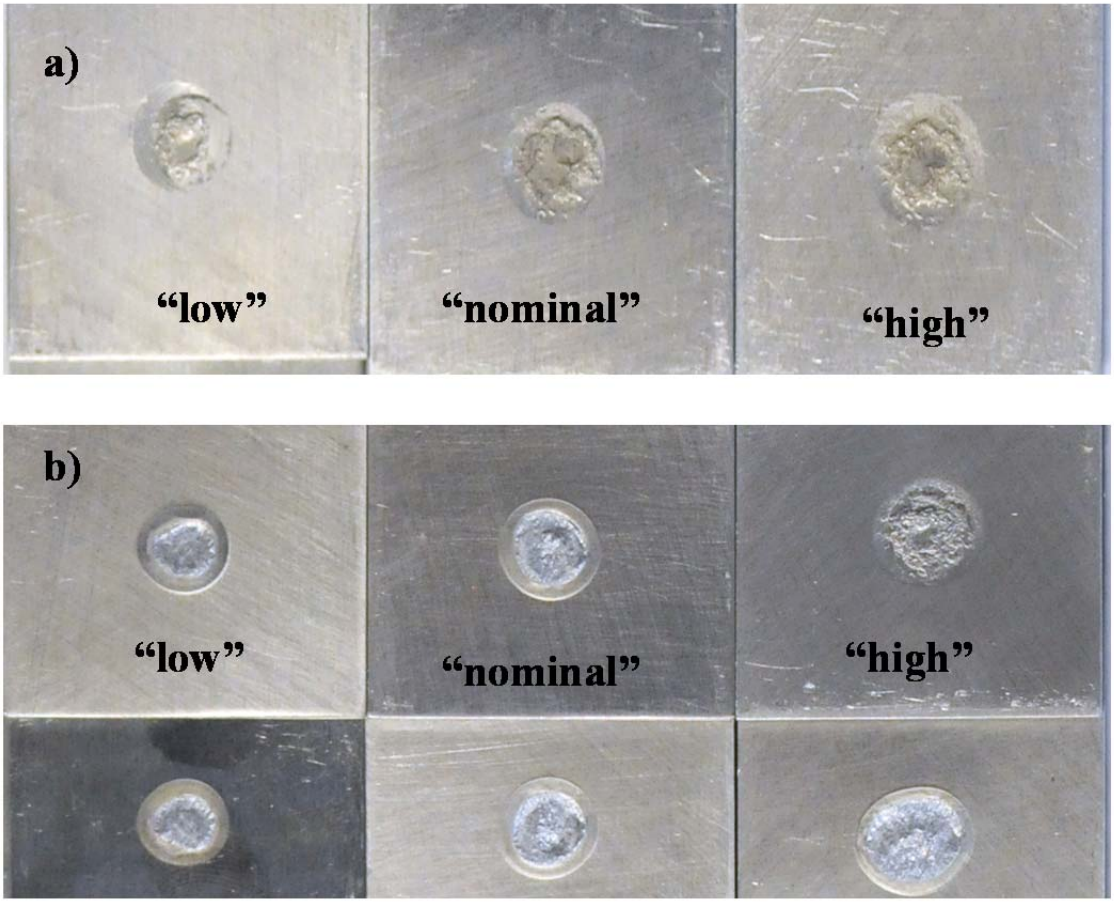

Figure 2.4 Welded specimens prior to quasi-static tensile testing (a) and fractured specimens (b)

It can be observed that the weld nugget diameter (b) increases from "low" condition to "high." All specimens failed in an interfacial fracture mode due to low ductility of 6061-T6 aluminum alloy.

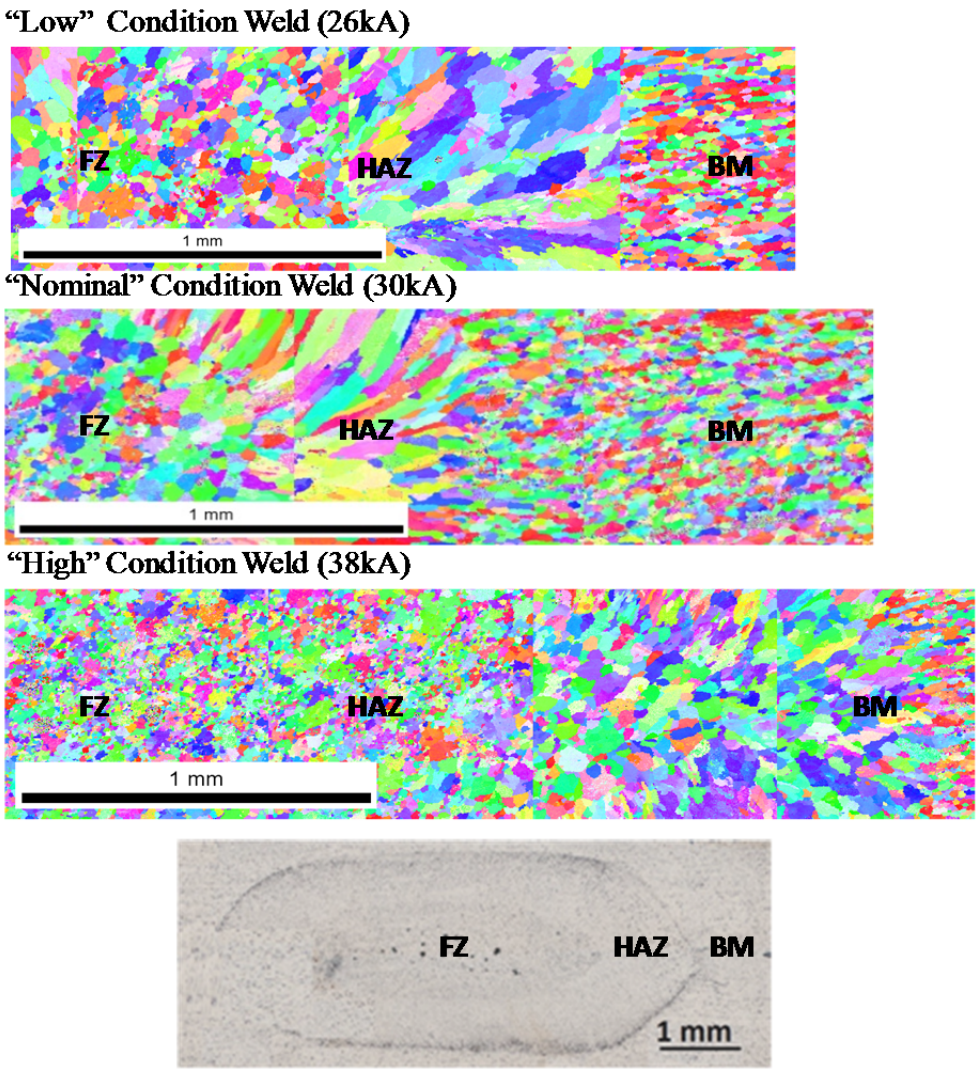

Figure 2.5 Fusion zone (FZ), heat affected zone (HAZ) and base metal (BM) are shown on Electron Back Scatter Diffraction (EBSD) grain size mapping plot along with the grain sizes in these regions

The quality of weld is poor for "low" condition, and the grain orientation is non-uniform because of insufficient heat input. The grain size in FZ and HAZ depends upon the amperage of the welding current. The microstructure is less uniform and the grain size transition less smooth at lower heat input.

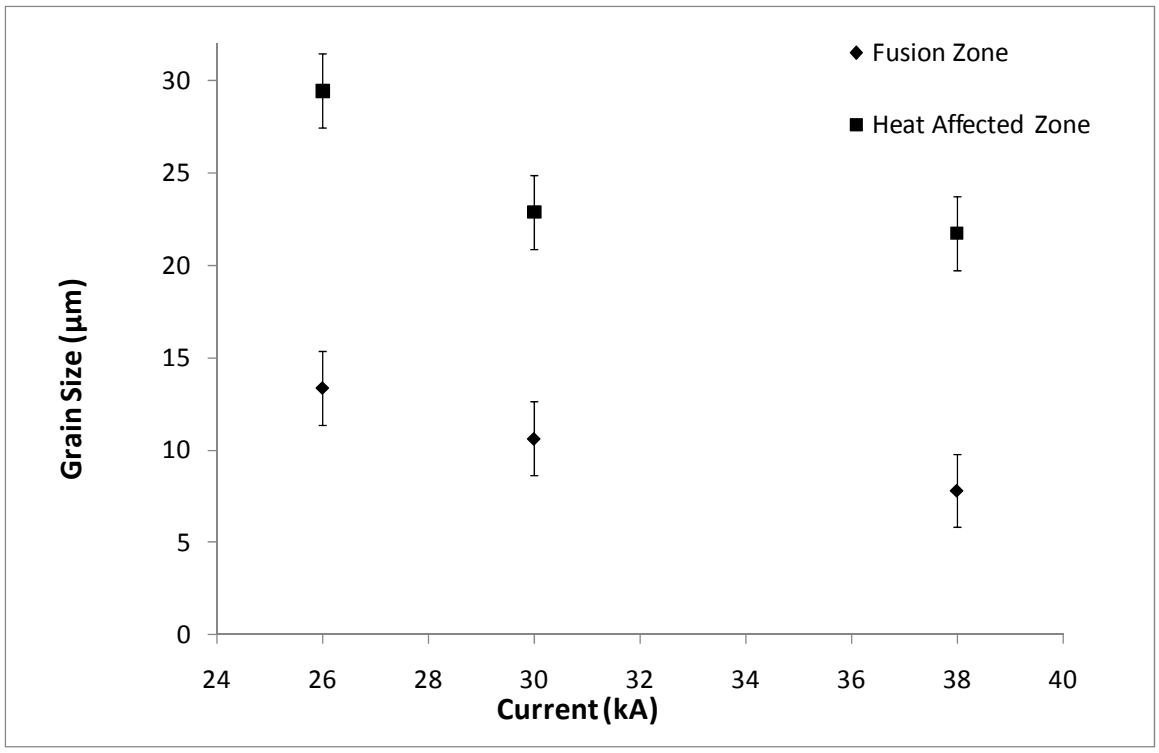

Figure 2.6 Average grain size as a function of welding conditions for the fusion zone (FZ) and heat affected zone (HAZ)

The welding conditions were: “low”, “nominal” and “high”.

References

[1] N. T. Williams, J. D. Parker. Review of resistance spot welding of steel sheets. Part 1: Factors influencing electrode life. International Materials Reviews 2004; 49: 45-75.

[2] N. T. Williams, J. D. Parker. Review of resistance spot welding of steel sheets. Part 2: Modeling and control of weld nugget formation. International Materials Reviews 2004; 49: 77-108.

[3] R. S. Florea et al. An experimental study of mechanical behavior of resistance spot welded aluminum 6061-T6 joints. ASME International Mechanical Engineering Congress and Exposition 2010: In Press.

[4] S. Aslanlar, A. Ogur, U. Ozsarac, E. Ilhan. Welding time effect on mechanical properties of automotive sheets in electrical resistance spot welding. Materials & Design 2008; 29: 1427-1431.

[5] M. Jou. Experimental investigation of resistance spot welding for sheet metals used in automotive industry. JSME International Journal, Series C-Mechanical Systems, Machine Elements and Manufacturing 2001; 44: 544-552.

[6] X. Sun, P. Dong. Analysis of aluminum resistance spot welding processes using coupled finite element procedures. Welding Research Supplement 2000; August: 215-221.

[7] E. Feulvarch, V. Robin, J. M. Bergheau. Resistance spot welding simulation: a general finite element formulation of electro thermal contact conditions. Journal of Materials Processing Technology 2004; 153-154: 436-441.

[8] H. Eisazadeh, M. Hamedi, A. Halvaee. New parametric study on nugget size in resistance spot welding using finite element method. Materials and Design 2010; 31: 149-157.

[9] ABAQUS Technology Brief. Welding simulation using ABAQUS. TB-05-WELD-1 2007; April: 1-3.

[10] J. A. Khan., L. Xu, Y-J Chao, K. Broach. Numerical simulation of resistance spot welding process. Numerical Heat Transfer 2000; 37: 425-446.

[11] J. A. Khan, L. Xu, Y-J Chao. Prediction of nugget development during resistance spot welding using coupled electrical-thermal-mechanical model. Science and Technology of Welding and Joining 1999; 4: 201-207.

[12] K. E. Weiss. Paint and Coatings: A mature industry in transition. Journal of Progress in Polymer Science 1994; 22: 203-245.

[13] MIL-W-6858D. Welding, resistance: spot and seam-This specification is approved for use by all Departments and Agencies of the Department of Defense, *Military specification; 28 March 1978:4-5.*

[14] H. Martin, M. F. Horstemeyer, P. Wang. Comparison of corrosion pitting under immersion and salt-spray environments on an as-cast AE44 magnesium alloy. Corrosion Science Elsevier 2010; 52: 7099-7108.

[15] C. Reichert and W. Peterson. Inspecting RSW Electrodes and Welds with Laser-Based Imaging. Welding Journal 2007; February: 38-45.

[16] R. B. Hirsch. Making Resistance Spot Welding Safer . Welding Journal 2007; February: 32-37.

[17] R. S. Florea et al. Failure Loads and Deformation in 6061-T6 Aluminum Alloy Spot Welds. TMS Supplemental Proceedings, Volume 2: Materials fabrication, properties and characterization; February-March, 2011: 213-220.

[18] Edison Welding Institute. Lab Services 2009: 1-6

[19] ALCOA Engineered Products. Understanding Extruded Aluminum Alloys-Alloy 6061. 2010 Brochure: 1-2.

[20] N. D. Hurley, W. H. Van Geertruyden, W. Z. Misiolek. Surface grain structure evolution in hot rolling of 6061 aluminum alloy. Journal of Materials Processing Technology 2009: 5990-5995.

[21] S. Brauser, L. A. Pepke, G. Weber, M. Rethmeier. Deformation behavior of spot-welded high strength steels. Materials Science and Engineering A 2010: 7099-7108.

[22] American Welding Society (ASW). Specification for Automotive Weld Quality; January 2007: 1-40.

[23] H. W. Coleman and W. G. Steele. Experimentation, Validation, and Uncertainty Analysis for Engineers, Third Edition. John Wiley & Sons, Inc., 2009:10.

CHAPTER III

WELDING PARAMENTERS INFLUENCE ON FATIGUE LIFE AND MICROSTRUCTURE IN RESISTANCE SPOT WELDING OF 6061-T6 ALUMINUM ALLOY

Introduction

The fatigue behavior of Resistance Spot Welding (RSW) in aluminum 6061-T6 alloy (AlMg1SiCu per International Standard Office nomenclature) was experimentally investigated. Three welding conditions, denoted as “nominal,” low” and “high,” were studied to determine the microstructure of the weld nuggets. The process optimization included consideration of the forces, currents and times for main weld and post-heating. By successive iterations and “witness samples” collected, the optimum welding parameters were determined. Load control cyclic tests were then conducted on single weld lap-shear joint coupons to study the microstructure and fatigue life properties. These tests were used to characterize the fatigue behavior in spot welded specimens to elucidate the influence of the process parameters. This work revealed that the welding process parameters have a great influence in the microstructure and fatigue life of the 2 mm-thick aluminum sheet resistance spot welded joints. Different fatigue failure modes were observed at several load ranges and ratios for a constant frequency and three welding currents.

Resistance Spot Welding (RSW) is a rapid joining technique extensively used to join thin shell assemblies in military and automotive applications. For example, one single automobile contains approximately 5,000 spot welds. The need for lightweight alloys and quality welds becomes a great interest in these industries for achieving improved fuel economy for ground vehicles. The resistance spot welding process bonds contacting metal surfaces via the heat obtained from resistance to an electrical current flow. In contrast to other welding processes, no filler metal or fluxes are used. Spot welding provides accelerated speed and adaptability for automation in high-volume and/or high-rate production. Despite these advantages, however, RSW suffers from inconsistent quality between welds. Further implementation and improvement of existing processes (weld quality and time improvement, electrode life extension, maintenance cost reduction) and development of new techniques for RSW will greatly impact the above noted industries due to the large numbers of spot welds they perform in their manufacturing processes [1, 2]. Therefore, understanding process parameters, such as weld size, weld indentation, sheet separation and weld residual stresses, will improve the weld quality during fabrications. Evaluating and predicting RSW performance in aluminum alloys is important for this technique's continued industrial integration.

In RSW, the experimental and modeling techniques integrate mechanical, metallurgical, thermal and electrical phenomena (Figure 3.1). The thermal and metallurgical interaction involves phase dependent thermal properties and the effects of latent heat and temperature history. Second, thermal and mechanical phenomena relate to thermal strains and residual stresses. Electrical and thermal effects are strongly correlated and involve temperature gradients, nugget formation and weld strength. From

a metallurgical and mechanical perspective, the process entails a complex interface between the base metal (BM), heat affected zone (HAZ), fusion zone (FZ), phase transformation, material hardening, and material anisotropy. The interaction between electrical and mechanical effects refers to contact conditions, electrode forces, overall geometrical dimensions, and the wear of welding electrodes.

The RSW process not only accommodates the interplay of all these factors but also requires satisfaction of demanding parameters (high current, high power, elaborate setups, robotic integration, sophisticated/specialized tooling, high productivity, short welding time, minimal thickness of metal sheets, etc.). Furthermore, aluminum welding is even more complex than steel welding because of the higher power and current requirements [3, 4]. Welded structures in these applications are smaller and lighter, thus emphasis is on the quality and number of welds as much as on the process itself. In practice, optimum welding parameters ensure consistent welds over a long production run, thereby defining the process' quality.

Regardless of the welding material used this interplay of phenomena and requirements renders computer-simulation and measurement of the performance/quality of RSW in different joints, materials, and applications significantly more difficult. Experimental studies [5-9] have been carried out on various engineering materials and the influence of the welding time, current and applied forces have been evaluated. It is a lack of experimental fatigue data in RSW especially for aluminum alloys due to the long testing time and complexity of the welding process. In an effort to address this data deficit, our study focused on fatigue behavior of Al 6061-T6 alloy resistance spot welded joints for three different welding conditions. The automotive industry seeks to decrease

the weight of vehicles to address energy and emission concerns. Furthermore, the automotive industry requires reduction of their production cost. Essential to realizing this goal is decreasing welding post-processing cost, specifically avoiding excessive sanding and painting processes to ensure acceptable appearance of the final product [10], and optimizing RSW is part of this effort.

This is the first paper of its kind to quantify the fatigue performance and microstructure of RSW in 6061-T6 aluminum alloy, depending on the welding parameters and process sensitivity (currents, forces, weld and post-heating times). Our results demonstrate that welding parameters do indeed significantly affect the microstructure and fatigue performance for these welds.

Materials

Coupon Fabrication

The wrought aluminum 6061-T6 alloy used in this study, produced by ALCOA/TW Metals Inc. [11-13], exhibits high yield strength and good ductility properties. Its chemical composition and mechanical properties are described in Tables 3.1 and 3.2 below. Specifically, 6061-T6's electrical resistivity is $4x10^{-6}$ ohm-cm, specific heat capacity is 0.896 J/g-°C, and thermal conductivity is 167 W/m-K. Each joint comprises two pieces, 100 mm long, 35 mm wide and 2 mm thick. The uncoated sheets overlap 35 mm with one simple weld joint in the middle. Wrought aluminum alloys typically display anisotropic plasticity and ductility behavior due to the manufacturing process (rolling, extrusion, etc.). From a welding perspective, aluminum and magnesium are considered Group 1 materials [14] and require special procedures for the involved equipment, oxide coating removal, cleaning, fit-up and joint thickness.

Lap-shear coupons were produced which met or exceeded MIL-W-6858D Military Specification [14], where the minimum nugget size was 5.7 mm and minimum shearing force was 3.8 kN per weld. This welding condition was denoted as “nominal”. Two other welding conditions were applied to produce specimens at other conditions: “low” and “high” conditions [15, 22- 23]. The lap-shear coupons were produced by Edison Welding Institute [16] and the geometry is illustrated in Figure 3.2. For this study, the natural oxide layer was removed from each sheet prior to welding. Additionally, the weld specimens were produced along the rolling direction of the metal sheet. Figure 3 shows weld parameter development for three welding conditions.

Optical Microscopy

Optical microscope images were captured for cross sections of the welds at the three conditions. Specimens were prepared for optical microscopy (OM) analysis of welds of the single-lap joint. After cutting, the coupons were cold mounted in resin powder and liquid and then mechanically ground and polished. After polishing, the coupons were etched using Keller’s reagent (95mL water, 2.5mL HNO3, 1.5mL HCl and 1.0mL HF). De-ionized water and ethanol neutralized the coupons after etching. All samples were then cleaned for 20 minutes in an ultrasonic bath using ethanol, then dried and placed in a desiccator until microscopy analysis. Typical optical micrographs for FZ, HAZ and BM are illustrated in Figure 3.3 along with the traces for the welding process.

Fatigue Tests and Scanning Electron Microscopy (SEM)

For the fatigue tests no special specimens were manufactured. The geometry for the welding coupons used is illustrated in Figure 3.2. After complete failure, post-process scanning electron microscope analysis was performed for different fracture surfaces.

A total of 36 specimens were cyclically tested under load control with a sinusoidal waveform at several different ratios (0.0, 0.1, 0.3 and 0.5) and 10 Hz frequency. The frequency was maintained at 10 Hz to visually monitor the tests and efficiently expedite the complete failures (maximum testing time was under 35 hours).

A median value for maximum load was chosen for maximum force at 2.0 kN based upon the static failure load stated by quasi-static measurements and endurance limit function ultimate tensile strength determined empirically for engineering materials [13, 15].

One load ratio (R=0.0) was chosen for three different welding conditions: “nominal”, “low” and “high”. For each condition 3 specimens were tested at 2.0kN maximum force while the frequency was maintained at 10 Hz.

Equipment and Experiments

Figure 3 indicates the process sensitivity development (“nominal”, “low” and “high” welding conditions) along with micrographs for all three cases. The left hand side of this Figure 3.3 shows electrical current and electrode force traces for main weld and post heating processes. The cuts were performed on weld center lines for rolling direction.

Figure 3.4 shows the process sensitivity development (“nominal”, “low” and “high” welding condition welds) along with micrographs for all three cases. Left hand

side of this figure shows electrical current and electrode force traces for main weld and post heating processes. The cuts were performed on weld center lines for rolling direction.

For weld cross section analysis, an AXIOVERT optical microscope (OM) with an inverted light was used to take images of the mounted coupons at 5X magnification. The welding equipment (manufactured by ARO Welding Technologies Ltd) with servo-gun and weld control was used to manufacture the specimens for this study, as shown in Figure 3.4. A Yokogawa scope-corder DL750 and Miyachi weld monitor recorded and monitored the welding process. Traces to capture welding current, electrode position, and force were utilized via ARONET 2006 software [17]. The power supply was a direct current (DC) type. The cooling water flow at room temperature was approximately 4 liters/minute. CMW-28 copper-zirconium based alloy weld cap electrodes were used. Fixtures were located along the 100 mm long pieces of aluminum in order to obtain consistent results over the entire process run. Periodically, an electrode re-dressing was performed. Figure 3.1(c) shows the periodic "witness peeling" samples (every 20 samples) tested during the welding process development.

Figure 3.5(a) shows the servo-hydraulic load frame (MTS 810 Material Test System) with the RSW coupon placed in the grips, and Figure 3.5(b) provides a closer view of the lower grip and the 2 mm thick shim placed behind one side of the specimen. An identical shim was also used in the upper grip. The coupons were gripped 40 mm from the center of the coupon. Thus, the grip-to-grip distance for each specimen was 80 mm with 60 mm long shims on top and bottom. Figure 3.6 shows the specimens for the

three process conditions, denoted as “nominal”, “high” and “low”. These RSW’ed coupons were used for fatigue testing.

Prior to this research, monotonic tests were performed in order to determine the quasi-static failure loads for the three different welding conditions [15]. Once the monotonic strength of the RSW coupons was determined, load levels for the fatigue tests were chosen based on standard fatigue assumptions and calculations. The tests were conducted at 10 Hz frequency to expedite failure and to be easily monitored during the experiments. Complete failure of the coupons was observed, and the results are summarized in Table 3.4. A total of 36 coupons were cyclically tested under load control condition with a sinusoidal waveform at 4 load ratios at “nominal” condition. Figure 3.7 shows the maximum load versus the number of cycles to complete failure. For the “low” and “high” welding conditions, just one load ratio was chosen to observe the fatigue life trend. The results are captured in Table 3.5. Figure 3.8 shows the average number of cycles for each of the welding conditions as described above. The formulas used for these calculations are:

$$R = \frac{P_{max}}{P_{min}} \tag{3.1}$$

$$\Delta P = P_{\max} - P_{min} \tag{3.2}$$

$$S_e = 0.5 \times \text{UTS} \tag{3.3}$$

For post-fatigue microstructure analysis, an EDAX Sapphire Scanning Electron Microscope (SEM) made by AMETEX was used, accompanied with a Smart SEM User Interface. The SEM is standard equipment for performing failure analysis and fractography. The SEM offers significantly superior resolution and depth of field as

compared to the OM, increasing the useful magnification range. Prior to scanning, the samples were cut and small coupons were extracted. To make the coupons conductive a Sputter Coater made by Polaron/EB Science apparatus was used to charge each specimen for approximately 25 seconds. Palladium/Gold coating was used. Compared to transmission electron microscopes, SEM allows the examination of relatively large samples, such as those used in this study, and produce images with a 3D character. SEM images were captured only for the interfacial failure mode at nominal condition (specimen #36). Other failure cases will be addressed in a future paper.

Results and Discussions

Process Development and Sensitivity Analysis

Welded specimens of various nugget sizes were produced in order to realize the correlation between the process parameters and the weld quality. The equipment used in this study was capable of the weld-and-forge operation that reduces the porosity and solidification cracking prevalent when aluminum alloys are resistance spot welded. The welding parameters that were used to produce welding nuggets are tabulated in Table 3.3 Changing process parameters improved the quality of welds that previously had interfacial failure, HAZ cracks and pitting to acceptable welds with no cracks. During the manufacturing process, periodic peel tests were performed after each batch of twenty specimens to check the quality of the welds. After the desired nugget diameter was obtained, a sample was prepared using standard metallographic and evaluation techniques to ensure optimal quality. Slight adjustments in weld current level and re-dressing the electrodes were performed to maintain the consistency of the specimen manufacturing process. Following the production of the samples at “nominal” condition, welding

parameters (weld time and/or weld current) were adjusted for producing slightly smaller (nominally 4.5 mm) and slightly larger (nominally 6.5 mm) weld nuggets. For all three welding conditions two welding steps were applied: main weld and post-heat. The time for main weld was maintained at 115 milliseconds, while the post heat was 150 milliseconds with a short 30 milliseconds transition time between welds. This action was required to allow weld nugget formation via electrode force and heat transfer due to applied high intensity electric current. Longer squeezing time was required to acquire solidification after metal melting and to prevent the mechanical response (excessive elastic and plastic deformation) for metal sheets. The force was larger during the post-heating process with respect to the main weld step.

Prior production welding, experiments with different weld parameters were performed to establish the correlation between those parameters and the weld quality, as tabulated in Table 3.3 [15, 22-23]. The time and the electrode forces were constantly maintained during this iterative process. For the first several welds, no post-heat current or force were applied. The first weld exceeded 5.7 mm standard nugget dimension. The current was lowered from 28 kA to 25 kA with no post heat, but the resulting weld was too small, and an interfacial failure was observed. The current was then increased to 26.5 kA, but the interfacial failure still occurred. For weld #6, the HAZ developed visible cracks and pits (see Figure 3.9a).

The second iteration included 35 kA current and 650 daN post-heat forces. Subsequently, the current was lowered to 32 kA and the resulting weld was acceptable. After this second iteration, the current was maintained at 30 kA and 31 kA and the welds were not acceptable. The electrodes buckled abnormally by increasing the electrode

forces to 500 daN and 800 daN, respectively. A proper electrode force is critical to eliminate expulsion [18-21]. This force will create a mechanical barrier around the molten metal to keep the material within the nugget area. When a spot weld is created, the aluminum heats up to melting temperature (for 6061-T6 alloy is between 582°C and 652° C). At the same time, the metal molecules are polarized in the same fashion for a very short time (milliseconds). This causes extremely strong magnetic field repulsion between these molten tiny droplets to launch them away from the weld area (in extreme cases metal expulsion can travel several feet). This is called expulsion and it is dangerous for working personnel. This also reduces the electrical resistance between the electrode and the welded sheet, lowering the surface heating under the electrode and creating insufficient molten state for the nugget. On other hand, if the electrode force is too large, the amount of heat created in the nugget region is reduced, and consequently, the weld strength compromised. In extreme cases this can totally eliminate fusion for welds with no weld button created. When the applied force was increased for weld #11, the welding electrodes abnormally buckled.

Weld #12 was denoted as “nominal” condition and the process included the main weld along with post heating. The maximum standard deviation for weld diameter was 0.5 mm, which is acceptable.

During this process, specimens were cross-sectioned and etched. Figure 3.9 shows weld #9 and weld #12. Significant pitting and cracks inside of the fusion zone were observed, as shown in Figure 3.9 a) while no cracks are detected as surface [23]. Thus, this weld is not acceptable per MIL-6858 specifications. Weld #12 has a much improved microstructure, as shown in Figure 3.9 b). The nugget is slightly shifted to the top of the

joint, which is characteristic of the DC power supply. This weld is acceptable from shape, dimensions and microstructural points of view.

The above set of process parameters were denoted as “nominal.” After the monotonic testing for this welding condition, the average shear strength was determined to be approximately 3.8 kN [15]. Approximately 150 coupons were manufactured at the “nominal” condition.

Following the production of the samples at “nominal” condition, the weld current was adjusted to “low” condition for producing slightly smaller (average 4.5 mm) and to “high” condition for slightly larger (average 6.5 mm) weld nuggets [15, 23]. Table 3.6 shows these details for described welding conditions including main weld and post-heating cycles.

Figure 3.3 shows the current and force traces for subsequent welding after “nominal” condition in order to produce welds at “high” and “low” conditions. These welding conditions helped to analyze the process sensitivity, mechanical and microstructure characteristics. The force and time steps were constant for all three conditions during the main welding and the post-heat process. The only variable changed was the applied electric current. This was the controlling factor for the amount of input heat, as described by Equation 4 (where Q is input energy, R_{Total} is total resistance of the electrode/sheet assembly, I is the input electric current and t is total welding time).

$$Q = \mathrm{R}_{Total} \times I^2 \times t \tag{3.4}$$

The total serial resistance is compounded by:

- Upper cooper electrode resistance

- Interface resistance between upper electrode and top aluminum sheet
- Resistance of aluminum top sheet
- Resistance of the bottom one
- Interface resistance between bottom sheet and lower cooper electrode
- Lower cooper electrode resistance

By changing the electric current, the microstructure and weld nugget sizes were significantly changed, as shown in Figure 3.3 micrographs. Subsequent tests show this from welding joint mechanical performances. The authors quantified in previous research the quasi static performances [15], and this study is focused on fatigue testing for mentioned three welding conditions.

Fatigue Testing and Post-Fracture SEM Analysis

The number of cycles for complete failure of "nominal" condition welded coupons varied from 12,230 cycles to 1,238,101 cycles. For 1.5 kN maximum load, at all analyzed ratios the fatigue life can be considered infinite for practical applications (over 1 million cycles). The maximum time for complete failure exceeded 34 hours at 10 Hz frequency. Figure 3.7 shows maximum load versus number of cycles to complete failure for different load ratios. The consistency of data for the same loads and ratios is remarkable.

Next set of data were captured at 2.0 kN maximum load, R=0.0 ratio for 3 different conditions. Following the trend of quasi-static testing, the fatigue life was maximum for "high" welding condition and minimum for "low" condition case. But, in this testing, the fatigue life dramatically decreased (more than one order of magnitude) at the "low" condition. For the quasi-static case, the failure force decreased from 6,000 N at

"high" condition to 3,000 N at "low" condition [15, 16]. For the "nominal" condition these values are in agreement with MIL-W-6858D specifications (approximately 3,800 N failure load and 5.7 mm weld nugget). In cyclic loading, the trend was a reduction from approximately 120,000 cycles to approximately 6,000 cycles. Figure 3.8 illustrates average number of cycles to complete failure for the three different welding conditions denoted as process 1, 2, and 3 respectively. A very interesting point is that the average life is similar for processes 2 and 3. Therefore, the fatigue life is not improved from process 2 to process 3, while the reported quasi-static failure forces are increased [16].

On fatigue tests for the "nominal" weld condition welds, failure modes were observed. Figure 3.10 shows the fractured resistance spot welding specimens, having the following modes of failure:

- Interfacial. It is characterized by a non-uniform surface area and no button and partial thickness visible fractures
- Partial thickness with button pull plus base material partial width failure
- Interfacial with button-pull with partial thickness
- "Button pull" fracture
- Failure over entire thickness of one plate without removal of weld button on one plate. This failure occurred on base material around the weld

Figure 3.11 shows the fractured specimens for the different welding conditions tested at one load ratio. Three failure modes were observed. The fatigue process sensitivity data demonstrated the critical importance of welding parameters on mechanical performance of RSW. At the "nominal" condition all 3 specimens were fractured under mode 5: small button area in comparison to fusion zone along with

complete severing of aluminum top sheet. At the “low” condition, failure mode 1 was observed. While at the “high” condition, all coupons failed with a combination of mode 1 and 5. American Welding Society standard AWS D8.1 [4] describes in detail the failure modes for resistance spot welds for steels. Our results were similar to this standard. The main difference is described in failure mode 5, which indicated failure over the entire thickness through the weld.

Post-fatigue microstructure analysis indicated various fatigue site initiations. Welding spatter is one of the reasons of starting of fatigue cracks. This shows the importance of correctly establishing the welding parameters in order to avoid the initiation of this kind of defect. Also cleaning of the welds by removing the spatter (by sanding prior to further processing, such as coating and painting) is critical for resistance spot welding, as well as for the other welding processes: shielded metal arc, gas tungsten arc, flux core arc welding, etc.

Porosity was observed during the welding process development and on fatigue fracture surfaces for specimen #36. Figures 3.12 a) and 3.12 c) show an overall image of the fractured surfaces for the top and bottom plates with microstructure details at the center of the welds. Large porosities (approximate 60 microns in diameter) were observed in the samples shown in Figure 3.12 b), while Figure 3.12 d) presents a nodular type surface. These are defects (similar to ones observed in castings) produced by rapid solidification during welding process.

Fatigue in metals presents classical microscopic features called striations. Striations are microscopic grooves or furrows that delineate a local crack after cyclic loading. Figure 3.13 shows SEM fractography of a fatigue resistance spot welding of

specimen #36 top plate at the “nominal” condition. Four sites of fatigue failure were identified as shown in detailed images a1) through d1) for Figure 3.13. The most visible striations were observed on Figure 3.13 a1). The spacing between them is approximately 30 microns. At the end of specimen life final fracture occurred (shiny region through the center of the weld).

Conclusions

Experiments revealed that the welding process parameters have a great influence upon the quality of the RSW of aluminum 6061-T6 alloy. From successive iterations and “witness samples” collected, the optimum current, force and welding time were determined. Process sensitivity was studied and summarized. The MIL-W-6858D Military Specification was met or exceeded for “nominal” and “high” welding conditions. Fatigue S-N curves is novel for this research field and was used to characterize mechanical behavior for a 6061-T6 aluminum alloy welding joint at coupon level. The numbers of cycles to complete failure of a 2 mm lap joint were consistent at the same loading forces and ratios. Fatigue failure modes were the same when the loading conditions remained constant, but these modes changed significantly when the forces and loading ratios were changed.

The welding current had a large influence on welding nugget dimensions and lap joint mechanical behavior. On “low” welding condition the fatigue life was decreased by an order of magnitude, which is a dramatic change in mechanical properties under cycling loading. The number of cycles to failure ranged from approximate 6,000 to 2,000,000 cycles.

No fatigue initiation sites were observed in the porous area formed from rapid solidification in the center of the welds. All four fatigue initiation sites were experienced at the outside in the welding button. Very visible striations next to the crack initiation sites were observed on this study. Brittle failure occurred through the center of the weld area at the end of specimen life.

The reported results are unique for aluminum resistance spot welded joints and have value for both academia and industry. American Welding Society and Military standards can use data obtained from this study to extend the data base of 6061-T6 aluminum alloy resistance spot welding.

The authors are currently studying the influence of corrosive environments on RSW fatigue life. In the future, we plan to develop FEA simulation incorporating a coupled thermal-electrical-mechanical process (a model was created and preliminary results were obtained) in order to further investigate the effect of process parameters on the weld quality.

Table 3.1 Chemical composition of 6061-T6 aluminum alloy

Chemical composition (in wt.%)		Si	Fe	Cu	Mn	Mg	Cr	Zn	Ti	Other Each	Other Total	Al
Alloy 6061-T6	Max	0.8	0.7	0.4	0.15	1.2	0.35	0.25	0.15	0.05	0.15	Balance
	Min	0.4	-	0.15	-	0.8	0.04	-	-	-	-	Balance

Table 3.2 Mechanical properties specification limits of 6061-T6 aluminum alloy

Tempered	Direction	Limit	UTS (MPa)	YTS (MPa)	Elongation (%)	Density (g/cm^3)
Alloy 6061-T6	Longitudinal/Transversal	Minimum Value	290	255	12	2.7

Table 3.3 Weld Parameter Development

Weld ID	Main Weld			Post-Heat			Average Weld Nugget Diameter (mm)	Standard Deviation Value (mm)	Observation
	Time (mS)	Force (daN)	Current (kA)	Time (mS)	Force (daN)	Current (kA)			
1	115	380	28	0	0	0	7.0	0.16	Trial and Error Weld (First Weld)
2	115	380	25	0	0	0	4.5	0.00	Interfacial Failure
3	115	380	26.5	0	0	0	5.2	0.00	Interfacial Failure
4	115	380	27	0	0	0	5.4	0.08	Weld Does Not Meet MIL Specs
5	115	380	28	0	0	0	5.7	0.05	Weld Marginally Meets MIL Specs
6	115	380	29	0	650	0	6.4	0.25	Visible Cracks and Pits in HAZ
7	115	380	35	0	650	0	7.0	0.00	Weld Meets MIL Specs (Second Trial and Error Iteration)
8	115	380	32	0	650	0	6.7	0.08	Weld Meets MIL Specs (Third Trial and Error Iteration)
9	115	380	30	0	650	0	5.3	0.00	Weld Does Not Meet MIL Specs
10	115	380	31	0	650	20	5.7	0.00	Small Visible Cracks in HAZ
11	115	500	30	150	800	18	5.7	0.00	The Electrodes Abnormally Buckle
12	115	380	30	150	700	16	6.6	0.49	Acceptable Weld ("Nominal")

Table 3.4 Experimental fatigue results of RSW coupons

Specimen ID (#)	Frequency (Hz)	ΔP (kN)	Max P (kN)	Min P (kN)	R (Ratio)	No. of cycles for final failure (Nf)	Time to failure (hours)
1	10	1.35	1.5	0.15	0.1	325,915	9:03:13
2	10	1.35	1.5	0.15	0.1	348,498	9:40:15
3	10	1.35	1.5	0.15	0.1	324,122	9:00:14
4	10	1.80	2.0	0.20	0.1	130,356	3:37:17
5	10	1.80	2.0	0.20	0.1	145,979	4:03:18
6	10	1.80	2.0	0.20	0.1	102,369	2:50:38
7	10	2.25	2.5	0.25	0.1	12,230	0:20:24
8	10	2.25	2.5	0.25	0.1	12,504	0:20:52
9	10	2.25	2.5	0.25	0.1	17,201	0:28:42
10	10	1.4	2.0	0.6	0.3	211,490	5:51:30
11	10	1.4	2.0	0.6	0.3	259,283	7:12:10
12	10	1.4	2.0	0.6	0.3	265,985	07:23:20
13	10	1.75	2.5	0.75	0.3	56,993	1:35:00
14	10	1.75	2.5	0.75	0.3	39,407	1:05:42
15	10	1.75	2.5	0.75	0.3	34,358	0:57:16
16	10	1.05	1.5	0.45	0.3	1,028,369	28:33:59
17	10	1.05	1.5	0.45	0.3	1,136,335	31:33:21
18	10	1.05	1.5	0.45	0.3	1,238,101	34:23:31
19	10	0.75	1.5	0.75	0.5	1,537,403	42:42:21
20	10	0.75	1.5	0.75	0.5	1,936,342	53:47:14
21	10	0.75	1.5	0.75	0.5	1,719,783	47:46:18
22	10	1.0	2.0	1.0	0.5	499,480	13:52:29
23	10	1.0	2.0	1.0	0.5	413,234	11:28:44
24	10	1.0	2.0	1.0	0.5	575,815	15:59:42
25	10	1.25	2.5	1.25	0.5	151,291	04:12:10
26	10	1.25	2.5	1.25	0.5	156,959	04:21:37
27	10	1.25	2.5	1.25	0.5	167,862	04:39:47
28	10	1.5	1.5	0.0	0.0	197,765	05:29:37
29	10	1.5	1.5	0.0	0.0	209,323	05:48:52
30	10	1.5	1.5	0.0	0.0	278,515	07:44:12
31	10	2.0	2.0	0.0	0.0	121,321	03:22:13
32	10	2.0	2.0	0.0	0.0	141,175	03:55:18
33	10	2.0	2.0	0.0	0.0	117,794	03:16:19
34	10	2.5	2.5	0.0	0.0	13,804	0:28:01
35	10	2.5	2.5	0.0	0.0	19,825	0:33:03
36	10	2.5	2.5	0.0	0.0	16,071	0:26:48

Table 3.5 Experimental fatigue results of RSW coupons for 3 different welding conditions at R=0.0

Specimen ID (#)	Frequency (Hz)	ΔP (kN)	Max P (kN)	Min P (kN)	R (Ratio)	No. of cycles for final failure (Nf)	Time to failure (hours)
138(37)	10	2.0	2.0	0.0	0.0	121,321	03:22:13
139 (38)	10	2.0	2.0	0.0	0.0	141,175	03:55:18
140 (39)	10	2.0	2.0	0.0	0.0	117,794	03:16:19
6 “Big” (40)	10	2.0	2.0	0.0	0.0	113,596	03:09:20
7 “Big” (41)	10	2.0	2.0	0.0	0.0	186,887	05:11:29
8 “Big” (42)	10	2.0	2.0	0.0	0.0	103,348	02:52:05
63 “Small” (43)	10	2.0	2.0	0.0	0.0	5,594	00:09:19
64 “Small” (44)	10	2.0	2.0	0.0	0.0	6,893	00:11:30
65 “Small” (45)	10	2.0	2.0	0.0	0.0	5,602	00:09:21

Table 3.6 Welding conditions (processes) of 6061-T6 aluminum alloy

Welding condition	Electrode Force (kN) Main Weld/Post-Heat	Welding Time (sec) Main Weld/Post-Heat	Welding Current (kA) Main Weld/Post-Heat	Average Nugget Size (mm)
“Low”-Process 1	3.8/7.0	0.115/0.150	26/16	4.5
“Nominal”-Process 2	3.8/7.0	0.115/0.150	30/16	5.7
“Nominal”-Process 3	3.8/7.0	0.115/0.150	38/16	6.5

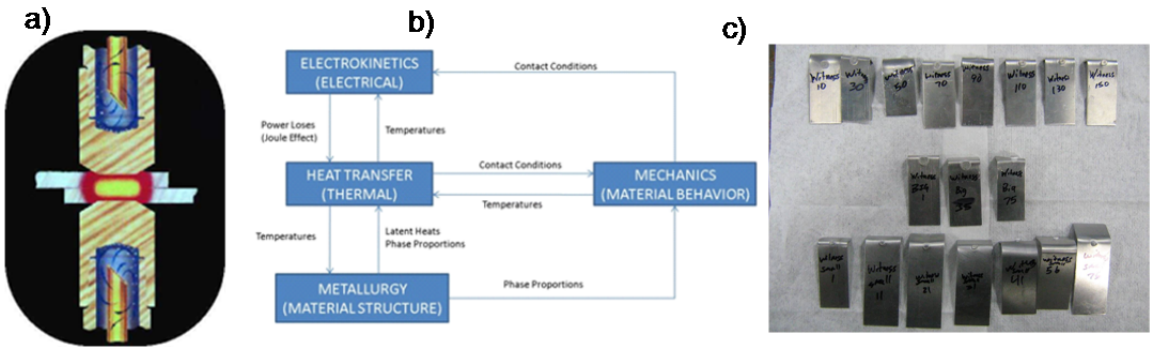

Figure 3.1 RSW process overview.

It is shown (a) electrodes with work pieces [21], (b) overview of phenomena involved [21-23] and (c) “witness peeling” samples tested during the welding process development.

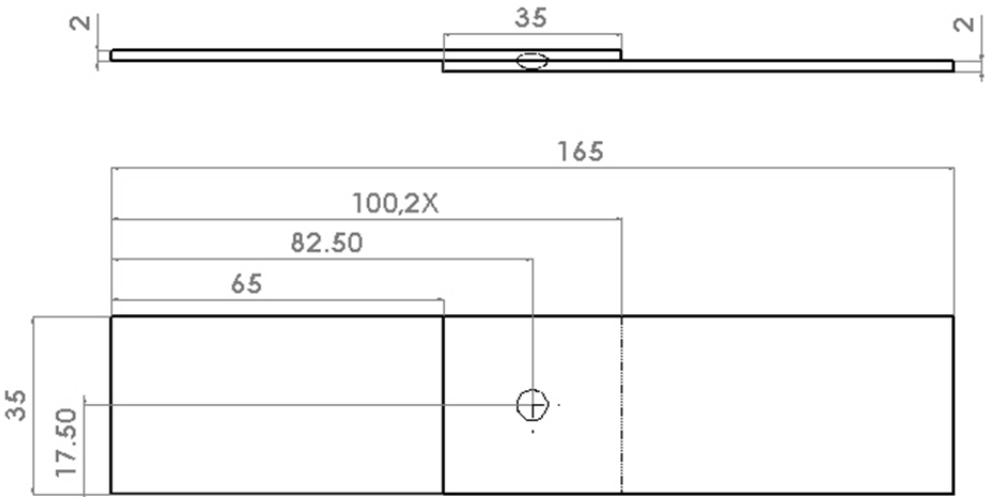

Figure 3.2 Geometry of Al 6061-T6 resistance spot weld lap-shear coupon.

Welding parameters were adjusted to achieve the process quality. Dimensions are in millimeters.

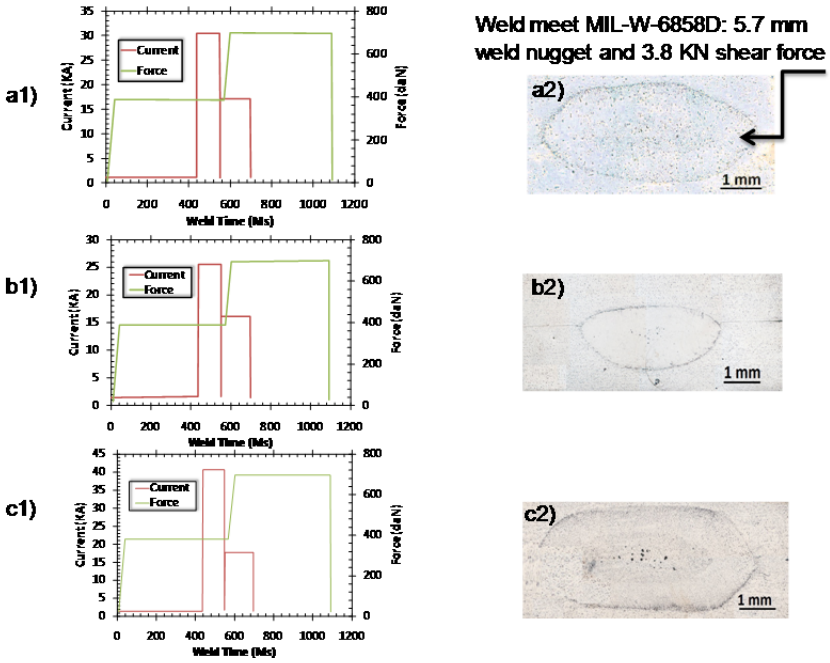

Figure 3.3 Weld parameter development (current and force traces) with corresponding microstructures for a1, 2) “nominal”, b1), b2) “low” and c1), c2) “high” conditions.

Main weld and post-heating process were performed to manufacture the specimens. Lap-shear coupons were produced by Edison Welding Institute to meet or exceed MIL-W-6858D Military Specification for “nominal condition [3, 4], where the minimum nugget size is 5.7 mm and minimum shearing force is 3.8 KN per weld. “Nominal” condition was acceptable but the “low” condition was not. Significant cracks and pits were observed for 3rd welding case. Left hand side figures are snap-shots from welding monitor.

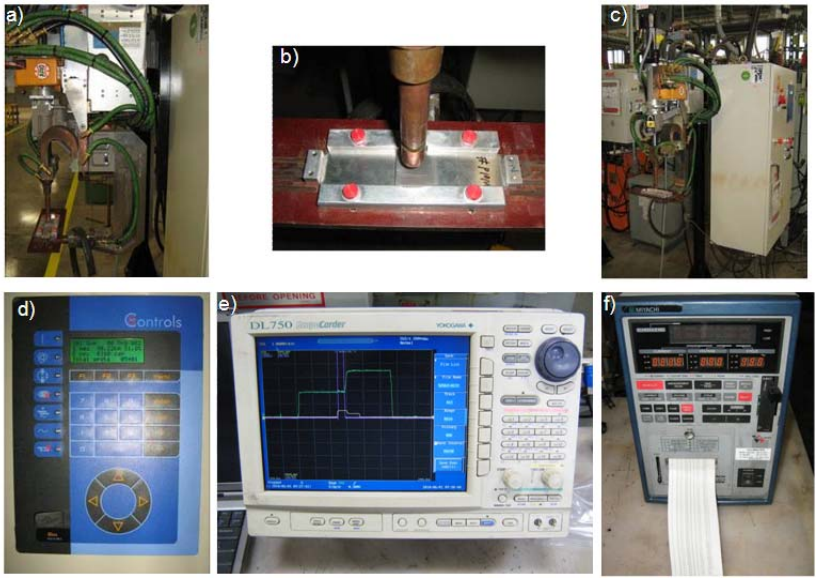

Figure 3.4 Welding equipment used to produce welds at three nugget sizes.

It is shown: a) and c) ARO equipment with servo-gun, b) locating fixture used to assure the specimen geometrical consistency, d) weld control, e) Yokogawa DC 750 scope-corder, and f) Miyachi weld monitor. Periodically an electrode re-dressing was performed to assure the weld quality over the entire production run. These welds were produced at Edison Welding Institute.

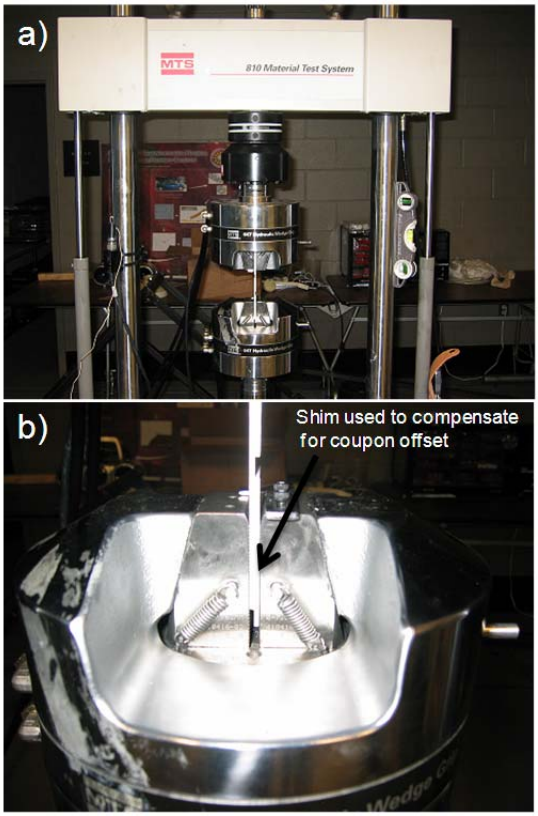

Figure 3.5 Fatigue testing set-up.

(a) A servo-hydraulic load frame shown with the resistance spot weld coupons tested under cyclic loading conditions. (b) A magnified view of the lower grips of the RSW test setup illustrating the use of the shim to compensate for specimen offset. A 2 mm thick shim made by same material was installed on lower grip, as highlighted. An identical sized shim was also used in the upper grip (not shown).

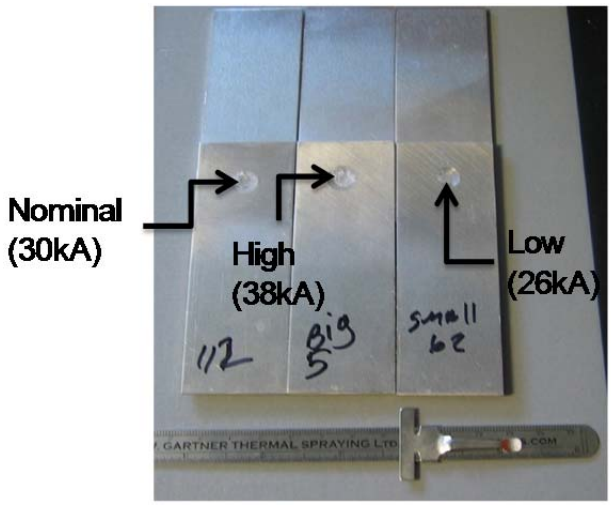

Figure 3.6 Resistance spot welding specimens for 3 process conditions denoted as "nominal", "high or big" and "low or small."

It can be observed that welding nuggets are dependent on applied electric current.

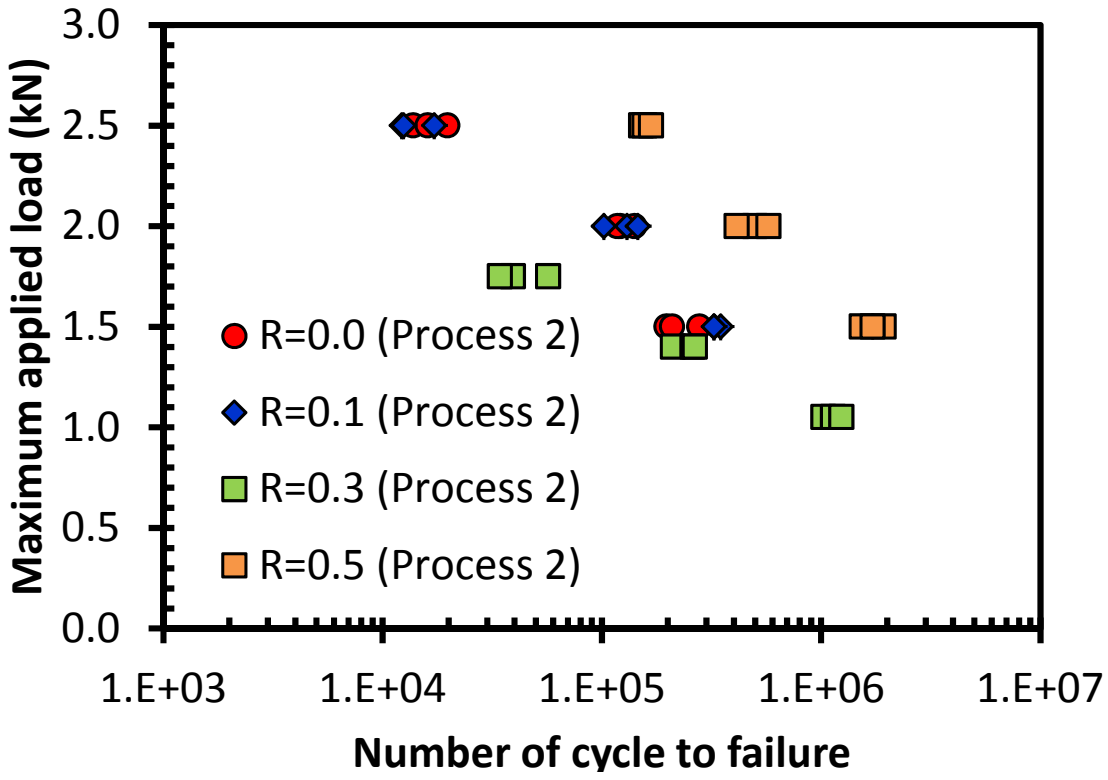

Figure 3.7 Graph shows maximum load versus number of cycles to complete failure for different load ratios.

All these data are for "nominal" condition welds.

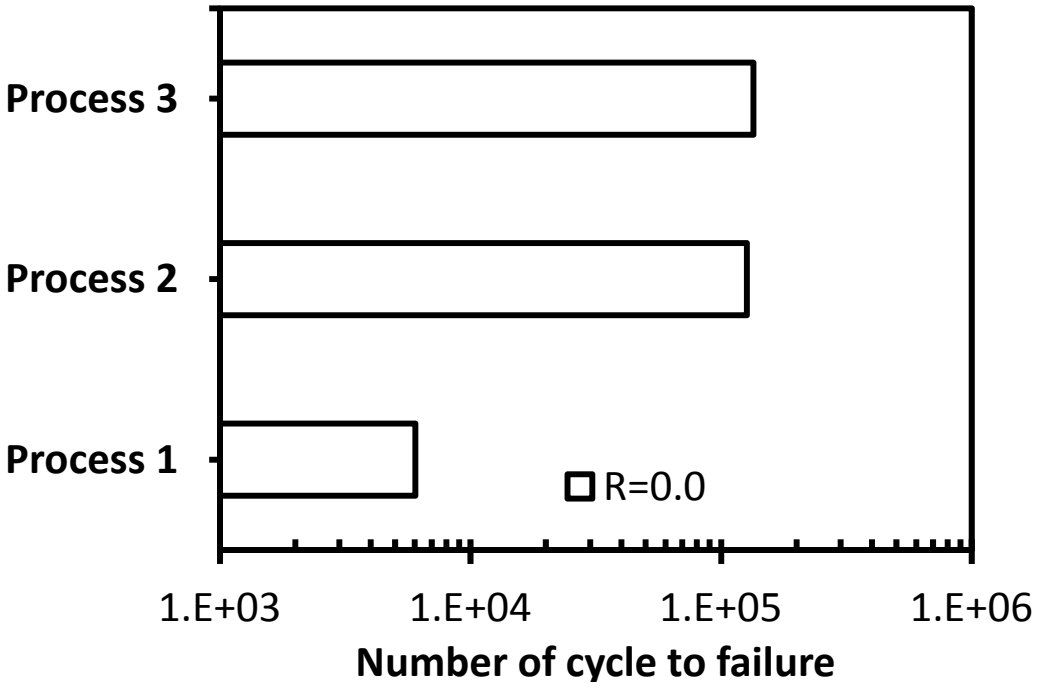

Figure 3.8 Graph shows number of cycles to complete failure for different welding conditions denoted as “nominal”, low” and “high”.

All these data are for ratio R=0.0.

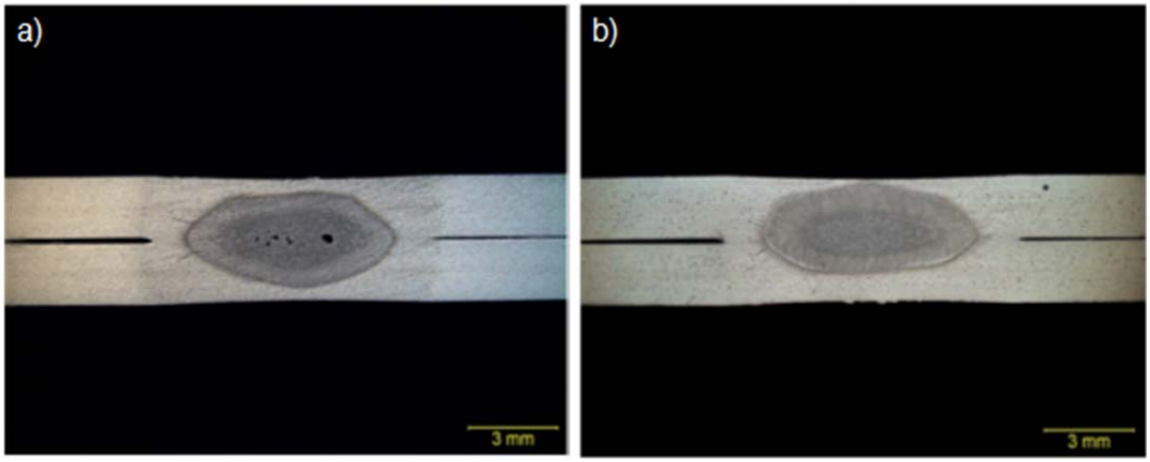

Figure 3.9 Macrographs of welds obtained during process parameter development.

It is shown: (a) weld #9 with significant pitting and cracks, but no cracks to surface (defect in MIL-6858) and (b) weld #12 with much improved microstructure and this is the baseline for “nominal” condition.

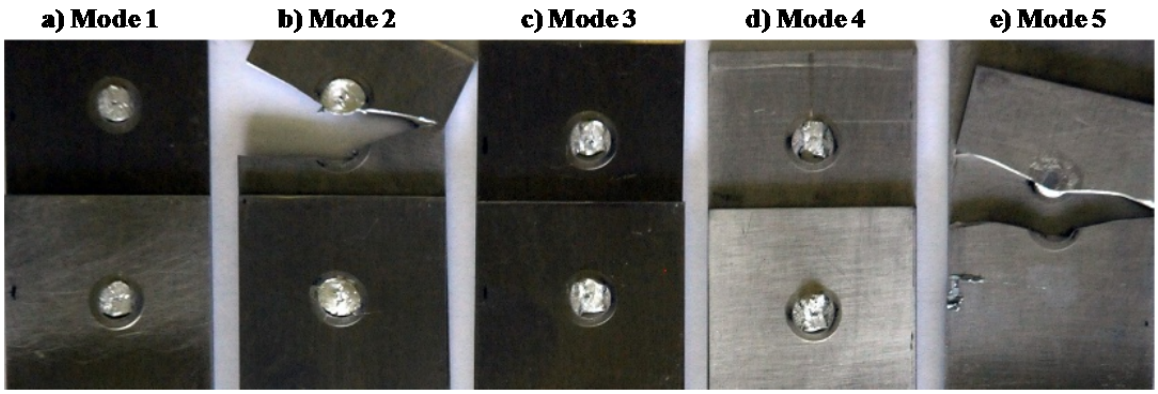

Figure 3.10 Fractured fatigue resistance spot welding specimens.

These specimens were tested at four different load ratios and nominal condition.

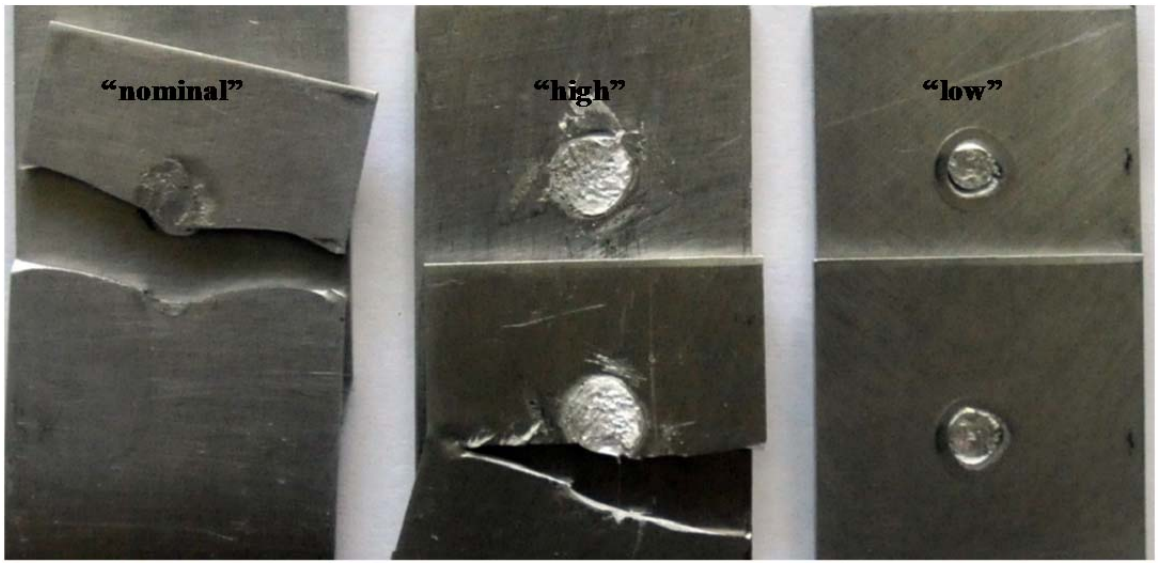

Figure 3.11 Fractured fatigue resistance spot welding specimens. These specimens were tested at one load ratio (R=0.00) and three welding conditions denoted as “nominal”, “low” and “high”.

The maximum load was 2.0 kN for all nine tests on process sensitivity fatigue study. The failure modes are different for the presented welding conditions.

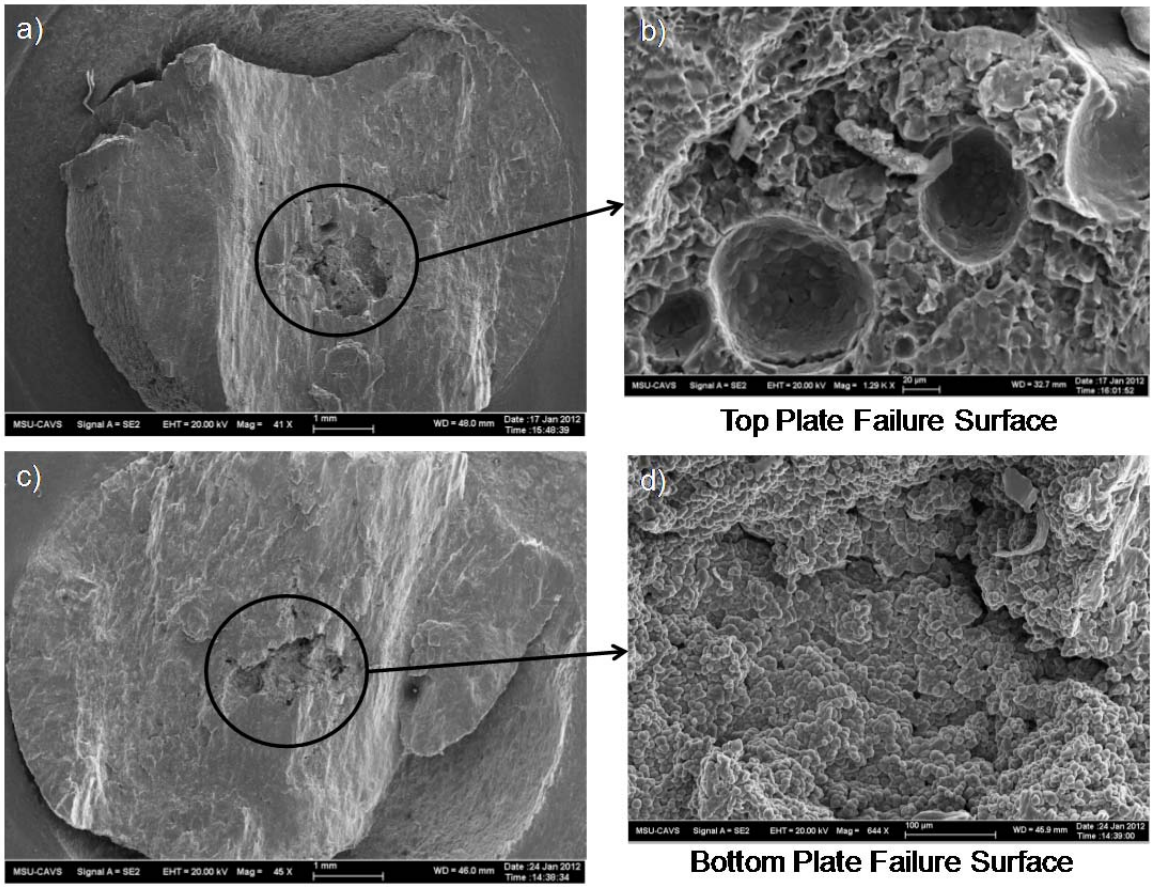

Figure 3.12 Scanning Electron Microscopy showing top and bottom of weld #36 for "nominal" condition.

The failure occurred as an interfacial mode.

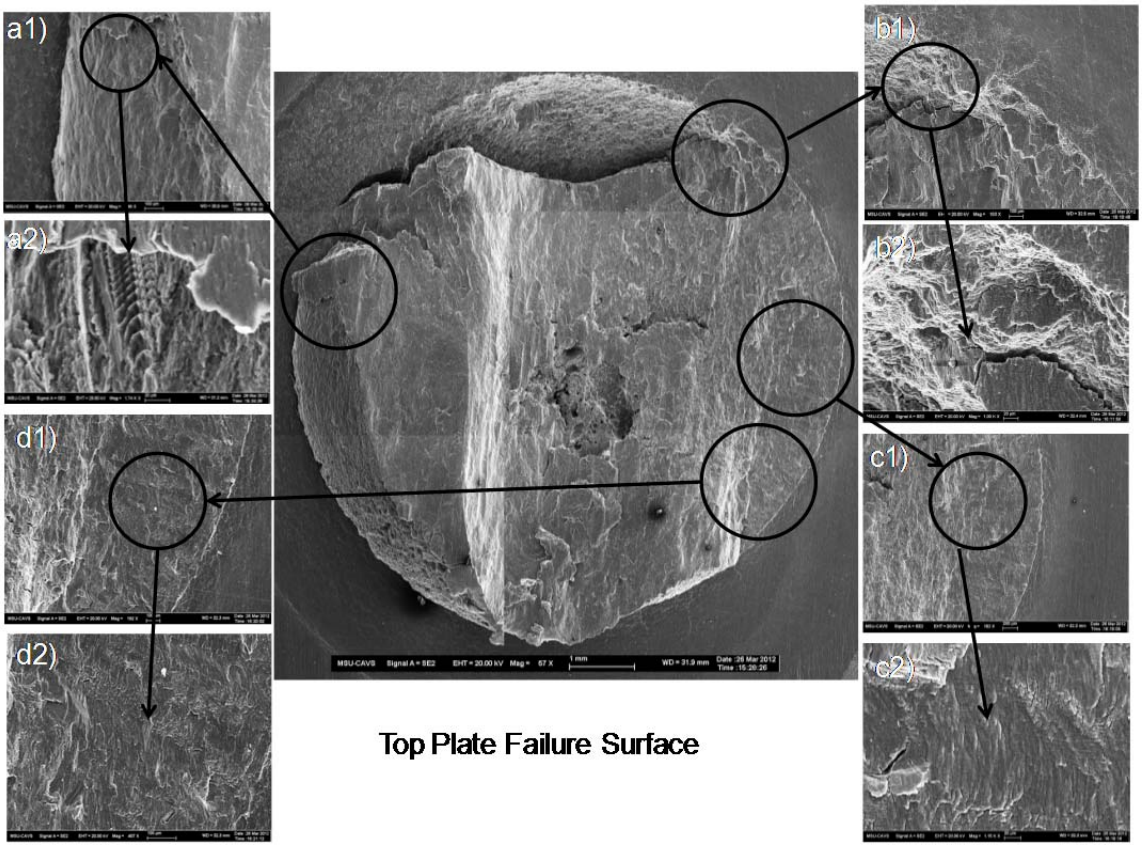

Figure 3.13 Scanning electron microscope fractography of a fatigue resistance spot welding of specimen #36 top plate at “nominal” condition.

Four sites of fatigue failure were identified as shown in images a1) through d1).

References

[1] N. T. Williams, J. D. Parker. Review of resistance spot welding of steel sheets. Part 1: Factors influencing electrode life. International Materials Reviews 2004; 49: 45-75.

[2] N. T. Williams, J. D. Parker. Review of resistance spot welding of steel sheets. Part 2: Modeling and control of weld nugget formation. International Materials Reviews 2004; 49: 77-108.

[3] R. A. Lindenburg, N. R. Braton. Aluminum Welding. Welding and other joining processes, Allyn and Bacon, Inc. 1976: 105-109.

[4] American Welding Society (ASW). Specification for Automotive Weld Quality-Resistance Spot Welding of Steel; January 2007: 1-40.

[5] T. Hong, T. Wei, L. G. Hector, P. D. Zavattieri. Uniaxial tensile and simple shear behavior of resistance spot-welded dual-phase steel joints. Journal of Materials Engineering and Performance 2008; 17(4): 517-534.

[6] M. Marya, K. Wang, L. G. Hector, X. Gayden. Fracture modes in single and multiple weld specimens in dual-phase steels. Journal of Manufacturing Science and Engineering 2006; 128: 287-298.

[7] M. Jou. Experimental investigation of resistance spot welding for sheet metals used in automotive industry. JSME International Journal 2001; 44: 544-552.

[8] S. Aslanlar, A. Ogur, U. Ozsarac, E. Ilhan. Welding time effect on mechanical properties of automotive sheets in electrical resistance spot welding. Materials & Design 2008; 29: 1427-1431.

[9] S. Aslanlar. The effect of nucleus size on mechanical properties in electrical resistance spot welding of sheets used in automotive industry. Materials & Design 2006; 27(2): 125-131.

[10] K. E. Weiss. Paint and Coatings: A mature industry in transition. Journal of Progress in Polymer Science 1994; 22 (2): 203-245.

[11] ALCOA Engineered Products. Understanding Extruded Aluminum Alloys-Alloy 6061; 2010 Brochure: 1-2.

[12] D. J. Spinella, J. R. Brockenbrough, J. M. Fridy. Trends in aluminum resistance spot welding for the auto industry. American Welding Society/ALCOA Technical Center‘s Development Laboratories, ALCOA Center, PA 2005.

[13] J. Marin. Mechanical Behavior of Engineering Materials. Prentice-Hall, Englewood Cliffs, N.J. 1962: 224.

[14] MIL-W-6858D 1978. Welding, resistance: spot and seam-This specification is approved for use by all Departments and Agencies of the Department of Defense, Military specification; 28 March 1978:4-5.

[15] R. S. Florea et al. Resistance Spot Welding of 6061-T6 Aluminum Alloy-Failure Loads and Deformation. Materials & Design 2012; 34: 624-630.

[16] Edison Welding Institute; Lab Services 2009: 1-6.

[17] R. S. Florea, C. R. Hubbard, K. N. Solanki, D. J. Bammann, W. R. Whittington and E. B. Marin. Quantifying Residual Stresses in Resistance Spot Welding of 6061-T6 Aluminum Alloy Sheets via Neutron Diffraction Measurements. Journal of Materials Processing Technology 2012; doi: 10.1016/j.jmatprotec.2012.06.024.

[18] C. Reichert and W. Peterson. Inspecting RSW Electrodes and Welds with Laser-Based Imaging. Welding Journal 2007; February: 38-45.

[19] R. B. Hirsch. Making Resistance Spot Welding Safer . Welding Journal 2007; February: 32-37.

[20] MEDAR. Welding Technology Corporation; website: www.medar.com.

[21] Miller Electric Manufacturing Corporation. Handbook for Resistance Spot Welding 2005:003 335A.

[22] R. S. Florea, K. N. Solanki, D. J. Bammann, J. B. Jordon and M. T. Castanier. Failure loads and deformation in 6061-T6 aluminum alloy spot welds. 2011 TMS Annual Meeting; 2: 213-220.

[23] R. S. Florea, K. N. Solanki, Y. Hammi, D. J. Bammann, and M. T. Castanier. An Experimental Study of Mechanical Behavior of Resistance Spot Welded m6061-T6 Joints. 2010 ASME Conference Proceedings, Mechanics of Solids, Structures and Fluids; 9: 37-43.

CHAPTER IV

QUANTIFYING RESIDUAL STRESSES IN RESISTANCE SPOT WELDING OF 6061-T6 ALUMINUM ALLOY SHEETS VIA NEUTRON DIFFRACTION MEASUREMENTS

Introduction

Residual strains of resistance spot welded joints of 6061-T6 aluminum alloy sheets were measured in three different directions denoted as in-plane longitudinal (σ_{11}), in-plane transversal (σ_{22}), and normal (σ_{33}). The welding process parameters were established to meet or exceed MIL-W-6858D specifications (i.e., approximately 5.7 mm weld nugget and minimum shearing force of 3.8 kN per weld confirmed via quasi-static tensile testing). Electron backscatter diffraction (EBSD) and optical microscopy (OM) were performed to determine grain size and orientation. The residual stress measurements were taken at a series of points along the weld centerline at depths corresponding to the weld mid-plane and at both 1 mm below the top surface of the plate and 1 mm above bottom surface. The residual stresses were captured on the fusion zone (FZ), heat affected zone (HAZ) and base metal (BM) of the resistance spot welded joint. Neutron diffraction results show residual stresses in the weld are approximately 40% lower than yield strength of the parent material. The maximum variation in residual stresses occurs, as expected, in the vertical position of the specimen because of the orientation of electrode

clamping forces that produce a non-uniform solidification pattern. Despite the high anisotropy of the welding nugget and surrounding area, a significant result is that measured stress values are negligible in both the horizontal and vertical directions of the specimen. Consequently, microstructure-property relationships characterized here can indeed inform continuum material models for application in multiscale models.

Resistance spot welding (RSW) is a rapid joining technique extensively used to bond thin metal sheets for military and automotive applications. In their critical efforts to address energy and emission concerns, improve fuel economy, and reduce production costs, these industries require lightweight alloys and quality welding to decrease the weight of their ground vehicles. Essential to realizing this goal is decreasing welding post-processing costs, which can be achieved through optimization of welding processes such as RSW.

The welding process bonds contacting metal surfaces via the heat generated by resistance to the flow of an electrical current. In contrast to other welding processes, no filler metal or fluxes are used. Spot welding provides accelerated speed and adaptability for automation in high-volume and/or high-rate production. Despite these advantages, however, RSW suffers from inconsistent weld quality. Further implementation and improvement of existing steps in the RSW process, such as weld quality and time improvement, electrode life extension, maintenance cost reduction, as well as development of new techniques for RSW will greatly impact these industries due to the large numbers of spot welds they perform in their manufacturing processes (e.g., a single automobile contains approximately 5,000 spot welds). Williams and Parker described the advancement in RSW in conformance to standards of the American Welding Society [1-

3]. Their review summarizes that understanding RSW process parameters, such as weld size, weld indentation, sheet separation and weld residual stresses, will facilitate improvements in weld quality during fabrications. Evaluating and predicting RSW performance in aluminum alloys is essential for this technique's continued and expanded industrial integration.

The RSW process integrates mechanical, metallurgical, thermal and electrical phenomena. The thermal and metallurgical interaction involves metallurgical transformations, phase dependent thermal properties, and the effects of latent heat and temperature history. The thermal and mechanical phenomena relate to thermal strains and residual stresses. Electrical and thermal effects are strongly correlated and involve temperature gradients, nugget formation and weld strength. From a metallurgical and mechanical perspective, the process entails a complex interface between the base metal (BM), heat affected zone (HAZ), fusion zone (FZ), phase transformation, material hardening, and material anisotropy. The interaction between electrical and mechanical effects depends on contact conditions, electrode forces, overall geometrical dimensions, and the wear of welding electrodes. The RSW process not only incorporates the interplay of all these factors, but it also requires satisfaction of demanding parameters (e.g., high current, high power, elaborate setups, sophisticated/specialized tooling, high productivity, robotic integration, short welding time, minimal thickness of metal sheets). In practice, optimum welding parameters ensure consistent welds over a long production run, thereby defining the process' quality. Notably, RSW of aluminum is even more complex than it is with steel because of the higher power and current requirements; however, welded structures in aluminum applications are beneficial because they can be smaller and lighter

than their steel counterparts. Thus, for RSW of aluminum, emphasis is on the quality and number of welds as much as it is on the process itself.

Regardless of the type of welding material used, this interplay of phenomena and requirements renders computer-simulation and measurement of the performance/quality of RSW in different joints, materials, and applications significantly more difficult. Experimental studies have evaluated the influence of the welding time, current, and applied forces on various engineering materials, but a better understanding of the relationship between input parameters and residual stress fields could lead to further optimization of RSW practice and modeling. Aslanlar et al. investigated the welding time effect on mechanical properties of automotive sheets in RSW [4]. Florea et al. quantified via laser profilometry the influence of the welding current in the electrode imprint of the 6061-T6 aluminum alloy RSW'ed joints, while safety of the process was studied by Hirsch [5-7].

In their review papers, Withers and Bhadeshia described types of residual stresses as macro-stresses (which vary over large distances) or micro-stresses (which vary over the grain or atomic scale). Macro-stresses are induced by peening, bending or welding. Micro-stresses include thermal, transformation and intergranular stresses[8, 9]. In many cases, residual stresses are detrimental to the material; however, toughening of glass or shot peening, for example, can be advantageous. There are various methods, both destructive and non-destructive, to measure residual stresses. Destructive methods include hole-drilling and curvature measurements. Non-destructive methods include X-ray diffraction and infrared imaging as described by Reichert and Peterson [10]. Furthermore, for measurement techniques, Winholtz used hard X-rays as well as neutron,

ultrasonic and magnetic-based techniques. Nonetheless, while these analytical, experimental, and computational techniques can provide an estimation of the stress to which a component is loaded in service, most of them are not truly reliable for prediction because they lack sufficient means to account for unexpected failure due to residual and service stresses, which combine to significantly shorten component service life [11].

As an alternative to more traditional stress analysis tools, neutron scatter diffraction is the most effective non-destructive "bulk" or in-depth technique available. This Nobel Prize-winning technique was developed by Shull and Brockhouse in their exploration of ways to use the neutrons produced by nuclear reactors to probe the atomic structure of materials [12]. In neutron diffraction, a beam of neutrons is directed at a given material. The neutrons are scattered (bounce off) by atoms of the material and change direction depending upon the location of the atoms they hit. A diffraction pattern of the atoms' positions can thus be obtained. To know where and how atoms are situated in a material and how they interact with one another is the key to understanding the material's structural properties. For engineering, this technique is advantageous over X-rays because it allows penetration depth into materials in the order of many centimeters. In fact, the penetrating power of neutrons has been applied successfully for scanning welds, forgings, extrusions, bearings and laser engineered net shaping (LENS) deposition manufacturing. The main disadvantages of this method are the limited access to the required nuclear equipment, complex experimental set-ups, and low data acquisition rates. Pratt et al. (2008) used this technique to quantify residual stresses of LENS for AISI 410 thin plates [13]. Sutton et al. focused their research on friction stir welds (FSW)

of 2024-T4 aluminum alloy [14]. Woo et al. used the same technique to analyze stresses and temperature fields in FSW of 6061-T6 aluminum alloy [15].

Finite element work on residual stresses prediction for thin wall aluminum weld structures was performed by Asle-Zaeem et al., but this study was limited experimentally to measuring only the distortion of the "T" joint [16]. In addition, for high strength steels, the correlation between the weld process conditions and residual stresses was presented by James and al. [17, 18].

To obtain reliable residual stress measurements for this study, electron backscatter diffraction (EBSD) and optical microscopy (OM) were performed in order to determine how the grain structure varies in different positions of the RSW nugget and surrounding areas. These microstructural measurements provide information regarding required sampling volume size.

A weld joint stress gradients are the results of a complex thermal history which means the strain measurements and their conversion to stress can complicated.

The objective of this research is to evaluate the three-dimensional residual stress fields, denoted in-plane longitudinal (σ_{11}), in-plane transversal (σ_{22}), and normal (σ_{33}), for an RSW'ed 6061-T6 aluminum alloy. A neutron diffraction analysis of the joint section was conducted to map the elastic strain fields and associated statistics. An understanding of the spatial variation and the corresponding residual stress distributions of the RSW'ed 6061-T6 aluminum alloy will provide insight into the relationship between RSW process parameters and strength of welded joints.

Materials

Coupon Fabrication and Quasi-static Failure Loads

The wrought aluminum 6061-T6 alloy used in this study, produced by ALCOA/TW Metals Inc., exhibits high yield strength and good ductility properties. Its chemical composition and mechanical properties are described in Tables 4.1 and 4.2. Specifically, 6061-T6's electrical resistivity is $4x10^{-6}$ ohm-cm, specific heat capacity is 0.896 J/g-°C, and thermal conductivity is 167 W/m-K.

As depicted in Figures 4.1 and 4.2, the lap-shear coupons manufactured by Edison Welding Institute for this study were comprised of two uncoated sheets of the alloy, each 100 mm long, 35 mm wide and 2 mm thick and bonded with one simple weld joint in the middle, creating an overlap of 35 mm.

Aluminum and magnesium are considered Group 1 welding materials and require special procedures during RSW to accommodate the involved equipment, oxide coating removal, cleaning, fit-up and joint thickness. Accordingly, the lap-shear coupons were produced to meet or exceed the MIL-W-6858D Military Specification, where the minimum nugget size must be 5.7 mm and the minimum shearing force must be 3.8 kN per weld [19]. Three iterations of welding were performed in order to identify the most suitable welding condition for meeting these "nominal" metallographic requirements. See Table 3.1 for the list of weld parameters.

To confirm the quality during specimen manufacturing, periodic peel tests were performed after each batch of 20 specimens (Figure 4.1b). During the welding process, the electrodes were re-dressed at intervals of approximately every 100 welds.

Specimens Preparation for Grain Size and Orientation Analysis

The cross-section of a weld nugget was prepared for optical microscopy (OM) analysis. After cutting, the coupon was hot mounted in resin powder and then mechanically ground and polished. After polishing, the coupon was etched using Keller's reagent (95mL water, 2.5mL HNO3, 1.5mL HCl and 1.0mL HF). De-ionized water and ethanol were used to neutralize the coupons after etching. The sample was then cleaned for 20 minutes in an ultrasonic bath using ethanol, then dried and placed in a desiccator until microscopy analysis.

In order to quantify the microstructure, OM and electron backscatter diffraction (EBSD) mapping were performed. To reduce EBSD scan time, the specimen cross-section was analyzed by scanning half of the weld nugget in the longitudinal direction (rolling direction). "Grain dilution clean-up" function was performed with 5° tolerance angle and 2 microns minimum grain size.

Specimens for Residual Stress Measurements

Residual stress measurements require two types of specimens: those that are "stress free" and those with stresses "built-in" after the manufacturing process, which in this case is RSW. Coupons used in this experiment are described in section 2.1. One set of eleven, 3 mm-diameter cylinders were extracted from the welded lap joint in order to obtain stress-free specimens (Figure 4.2). The cylinders were extracted from the FZ, HAZ and BM along lines for the vertical and horizontal directions. Electron Discharge Machining (EDM) technique was used for miniature specimen extraction in order to minimize the stresses induced from the cutting operation. This cutting operation is effective because of its high tolerance precision and the low amount of heat it induces.

The RSW specimen with built-in stresses due to the welding process was mounted just above the stress-free cylinders and both measured in the same experiment.

Equipment and Experimental Details

Welding Equipment used to Fabricate Coupons, Testing Set-up to Analyze Failure Loads and Microstructure Analysis Software

Resistance spot weld equipment by ARO with servo-gun and weld control was used to manufacture the specimens for this study. A Yokogawa scope-corder DL750 and Miyachi weld monitor recorded and monitored the welding process. Traces to capture welding current, electrode position, and force were utilized as well. The cooling water flow at room temperature was approximately 4 liters/minute. CMW-28 copper-zirconium based alloy weld cap electrodes were used. Proper fixtures located the 100 mm long pieces of aluminum in order to obtain consistent results over the entire process run. Figure 4.3 illustrates the welding equipment and corresponding data acquisition instruments used to manufacture and analyze these coupons.

For tensile tests, a mechanical testing apparatus was used along with a laser extensometer at 50 mm at full-scale gage length. The displacement rate was 0.01 mm/seconds, and failure was defined as a 20% drop in the peak load.

For weld cross section analysis, an AXIOVERT optical microscope with an inverted light was used to take images of the mounted coupons at 5X magnification. For EBSD mapping, a Zeiss Supra40 Scanning Electron Microscope (SEM) was used, accompanied with TSL OIM Analysis 5 software. Figures 4.4 and 4.5 are showing samples that were analyzed to verify welding quality according to the described specifications.

Experimental Details for Residual Stress Measurements

Neutron diffraction (atomic strain gauge) is often used for stress measurement because it is generally non-destructive, thus making it possible to measure the sub-surface stresses without cutting or sectioning. At reactor-based neutron facilities, this method uses a monochromatic beam of neutrons of known wavelength scattered from a monochromator crystal.

For this study, the residual strains in resistance spot welded joints were measured via neutron diffraction in two-beam cycles on the Second Generation Neutron Residual Stress mapping Facility (NRSF2) at the HB-2B beam line on the High Flux Isotope Reactor (HFIR) at Oak Ridge National Laboratory (ORNL). With U-235 enriched uranium as fuel, this reactor operates as an 85 MW steady-state source with a peak thermal flux of $2.6\times10^{15} cm/s^2$. The HFIR is a beryllium-reflected, light-water-cooled and moderated flux-trap-type reactor. ORNL has the capability to conduct these measurements using a HIFR, which provides the source of neutrons for condensed matter research to 15 different instruments. The neutron residual stress mapping instrument was used for this work.

The sizes of the gauge volumes were necessarily quite small due to the geometry of the RSW joints. Table 4.4 lists the slit sizes used, and counting times were from 12 to 30 minutes per location. The positional accuracy can be important in neutron diffraction mapping if there are high gradients of strain or large changes of chemistry in some measurement locations. The latter situation is not important for this study because the welded joint sheets are the same material and no filler metal was involved in the process.

Calibration of the diffractometer and its position-sensitive detectors was accomplished using a series of powder standards. The NRSF2 data collection system and sample positioner are controlled by a set of powerful tools developed using LabView 7.0. The software provides automated instrument control with data collection option, system calibration, and post collection with real-time data processing.

Due to occasional service on the instrument, such as changes in detectors or repairs to the monochromator motor and switches, the NRSF2 instrument is realigned and calibrated using the set of reference powders at the beginning of each HFIR cycle. From the calibration, the neutron wavelength for each monochromator setting is determined.

For the neutron diffraction method, the sample must be mounted twice on the goniometer and the location of measurements determined with sufficient accuracy to avoid significant errors in calculated strains due to choosing an inappropriate stress-free d-spacing. Figure 4.6 shows the neutron scatter diffraction equipment used to measure residual stresses, including overall set-up and details for the optical alignment of specimens. Two fixture arrangements, made of high strength aluminum, were used to mount the welded coupon and stress-free cylindrical (comb) specimens. Figure 6a shows aluminum fixtures along with primary and secondary slits, while 6b illustrates a detailed view of a welded coupon with zero stress specimens (cylinders). Optical alignment devices (theodolites) used for precise alignment of all specimens is illustrated in Figures 4.6c and 4.6d. The set of eleven cylinder specimens were attached to the fixture using "Starkey Chemical Process" rubber cement (which conforms to ASTM D-4236 specification). The fixtures were then attached to the NRSF2 sample positioner. James et

al. also described laboratory set-ups for the neutron and synchrotron strain scanning in their experimental work [17, 18].

In strain scanning, "gauge volume" is defined by the intersection of the incident and scattered beams. The scattering collimator, having the same size range, was set close to the measured specimen. The location of the collimator controls the size of the gauge volume and also defines the translation range over which the specimen can be scanned. Measurements for the 6061-T6 aluminum RSW joint were performed in one beam cycle at NRSF2 using a gauge volume defined by incident and diffracted slits to be 1 mm x 1 mm x 2 mm tall. The 1x1 diamond in the horizontal plane corresponded to through thickness direction, while the 2 mm tall length was parallel to the sheets.

Figure 4.7 shows data acquisition for neutron scatter diffraction, including a data collection panel, a Gauss model for signal intensity, and a d-spacing illustration for measured location within the welded coupon and stress free combs. This technique was also used by Wang et al. in developing the theory of the peak shift anomaly due to partial burial of the sampling volume in neutron diffraction residual stress measurements. The aluminum alloy (311) diffraction peak was used in this study [20].

The diffraction peak for the Si331AF monochromator is located at approximately 90 degrees. The aluminum reference bar (Figures 4.6a, b), the center of the weld, and the stress-free cylinder #1 were measured beginning, end and middle of every experimental run for assessment of stability and accuracy. The wavelength and scattering angle are $\lambda = 1.73182\ \overset{0}{A}$ and $2\theta = 90^{\circ}$, respectively. These reference measurement points verified d-spacing and full width-half-maximum (FWHM) consistency (good repeats) over the

entire scan time. Furthermore, these measurements served to validate the experimental set-up and obtained results.

For this particular application, a scan for mid-thickness was the next step following set-up. This preliminary scan provides valuable information about the mounting accuracy as well as distortion of the welding joint in y-direction. We performed extrapolated scan shifts in y-direction when the y-direction measurement difference exceeded $\pm 0.1mm$ .The mid-thickness scan (y-scan) precedes all measurements for residual stresses in-plane transverse, normal and in-plane longitudinal. To capture "in-depth" residual stresses, three sets of thicknesses were measured as follows: in the center section of the welded joint, 1 mm up and 1 mm down with respect to the mid-plane. We denoted them as middle, top and bottom, respectively. The generated plots follow this nomenclature. For the 13 points along the horizontal and vertical sample lines (Figure 4.2) at the three depths, the neutron diffraction strain scanning required approximately 15 hours per direction.

The d-spacing (d_{hkl} lattice spacing and *h, k, l* are Miller indices) can be determined through wave length λ and diffraction angle θ_{hkl} using Bragg's law of diffraction (Eq. 1). The atomic planes of a certain crystallographic orientation $\{hkl\}$ diffract the neutrons at a given scattering angle:

$$\lambda = 2d_{hkl} \sin\theta_{hkl} \tag{4.1}$$

$$Q = q_{incident} - q_{diffracted} \tag{4.2}$$

where Q is the scattering vector, while $q_{incident}$ and $q_{diffracted}$ are the neutron beam vectors in the direction of the incoming and diffracted neutrons. The measured strain direction is parallel to the scattering vector. From the sets of scaled d-spacings for the welded joints and corresponding strain free reference cylinders, the strains were then determined (Eq. 3) from the change in inter-planar spacing for each location and for the each of the three orientations:

$$\sigma_{ii} = \frac{\varepsilon_{ij} E_{hkl}}{(1+\nu)} + \frac{\varepsilon_{kk} \nu \delta_{ij} E_{hkl}}{(1+\nu)(1-2\nu)} \tag{4.3}$$

where ε_{hkl} is the elastic residual strain and $d_{hkl}{}^{0}$ is the inter-planar spacing of the stress free reference. All diffraction strain measurements were defined with respect to a reference value of the stress-free condition.

As shown in Figure 4.2, we denoted horizontal as the rolling direction, while vertical was the transverse (against rolling) direction. The aluminum sheets were cut and RSW'ed coupons were manufactured according to this coordinate system. The determination of residual stress from measurement of residual strains requires measurement of strain in at least three orthogonal strain directions. In order to calculate the strain tensor, six independent measurements are needed, including the shear stresses. In this work, however, only three orthogonal strain measurements were obtained, and no shear stresses were measured. Sutton et al. studied FSW on 2024-T4 aluminum alloy and reported similar results limited to values for three orthogonal stresses [14]. Pratt et al. measured the residual stresses of laser-engineered net shaping AISI 410 thin plates,

taking calculated strain values as principal strains while the shear contributions to the strain tensor were negated [13].

Our assumption that strains measured are in the principal axis directions was based upon the geometry of the coupons (σ_{11} in the rolling direction) and the fact no filler metal was involved in welding process. This means no significant change in chemistry and lattice parameter (d-spacing measurement errors) occurred. In addition, subsequent (#3 and #4) welded coupons were selected for d-spacing and stress free d-spacing measurements in order to minimize the errors from a specimen to another because of changing in welding conditions over the entire production run.

Assuming negligible plastic deformation, Hooke's law (isotropic and homogeneous form) was used to transform the strain measurements to residual stresses:

$$\varepsilon_{hkl} = \frac{d_{hkl} - d_{hkl}^{\,0}}{d_{hkl}^{\,0}} \tag{4.4}$$

where E_{hkl} is the *hkl* specific diffraction elastic constants. Young's modulus of elasticity (E_{311} = 69 MPa) and Poisson's ratio (0.33) were used to convert strains to stresses based upon the equations developed by Noyan and Cohen [21]. The *k* is a dummy suffix summing over all *k (*i.e., $\varepsilon_{kk} = \varepsilon_{11} + \varepsilon_{22} + \varepsilon_{33}$), and δ_{ij} is the Kronecker delta. Structural polycrystalline materials contain imperfections that influence the intensity of the Bragg reflections distributions. No significant variation in peak-profiles intensity was observed that would be indicative of significant textures, despite the $\pm 4^{\circ}$ in omega oscillation. The neutron data supported the use of elastic constants for the case of random grain orientation. A propagation of errors approach was used to calculate an

Estimated Standard Deviation (ESD) of the strains and stresses using the ESDs for d-spacing from profile fitting and the scale factors. In this error analysis, sample repositioning and weld nugget anisotropy were not included.

Results and Discussions

Process Development and Microstructure Analysis

The complex microstructure and continuous variations of mechanical properties developed during the RSW process arise from the integration of mechanical, metallurgical, thermal and electrical phenomena. Electron backscatter diffraction (EBSD) measurements were carried out on the plane transverse to the welding direction. It was assumed that spatial variations of the microstructure (strain and temperature), from base material to solidified nugget, are akin to the time-dependent variations for a point in the weld nugget during welding. Figure 4.5 shows the EBSD mapping of the grain size and orientation due to the recrystallization process for the FZ (10.63μm), HAZ (22.90μm) and BM (16.62 μm) of the specimen. From the scans, the grain orientation toward the centerline of the nugget is visible where the increased temperature and squeezing forces create the observed grain structure.

In the FZ, the grain size decreases, but in the HAZ, the grain size increases. These changes in grain size are due to the high cooling rate during the transition from liquid metal to solid in the FZ, as opposed to the residual heat experienced in the HAZ that leads to grain growth. These results helped to further determine the neutron diffraction residual stress measurement parameters and set-up conditions. It was valuable to understand the microstructure of a processed RSW joint in order to best perform the neutron diffraction tests. The results indicated a significant degree of anisotropy of

material in the FZ, HAZ and sheet's interface induced by the RSW process. These results from microstructure analysis indicate a refined grain structure, which assures that good statistical measurements can be obtained using neutron diffraction and sampling volume sizes of 1 mm x 1 mm x 2 mm.

Residual Stress Measurements Results

The results were fit using a peak fitting Gaussian algorithm. In this work, three directions were measured in order to determine bulk residual stresses in Al6061-T6 nominal condition resistance spot welding joints, as described above. Four sets of stress results are plotted in Figures 4.8 through 4.11, following the steps described in Section 3.2. The origin of these plots is the center of the weld, and an x-coordinate represents the distance from the measured point to the origin in both longitudinal and vertical directions. The in plane-longitudinal stress component σ_{11} in the horizontal and vertical stress directions are shown in Figure 4.8. As expected, in horizontal direction the values are positive (tensile), while in vertical direction the stresses vary from ±100 MPa. The in plane-transversal stress component σ_{22} of the specimen is mostly positive. At the transition between HAZ and BM (away from the weld), the horizontal component of the residual stress (Figure 4.9a) becomes slightly compressive but very similar in value for all three depths measured. The transverse stresses in the vertical direction, illustrated in Figure 4.9b, have a linear trend due to the constantly applied electrode forces during main weld and post-heat cycles.

Figure 4.10 illustrates the normal (through thickness) or σ_{33} residual stresses. Notably, this stress is almost negligible; thus, the RSW specimens essentially exhibit

"plane stress." We consider the post-heating process to be responsible for this stress relief created at this direction along with the geometry effect (2 mm thin sheets welded).

Under the assumption that the residual shear stresses are negligible, von Misses stresses are illustrated in Figure 4.11. The plots notably have irregular shapes. This is caused by a complex stress field generated due to the mechanical force induced by electrodes and melting-solidification-recrystallization process and high temperature gradient. As shown in the EBSD scans, the grain size and orientation are irregular. The anisotropy created in the weld is proved also by the different stress values observed. The values are in 30-120 MPa range, which is significantly lower than base material yield or ultimate stresses.

For clarity, intermediate plots (strains, RSW d-spacings, and stress free d-spacings) are presented at the end of this section. Figures 4.12, 4.13, and 4.14 illustrate details about directly measured values and calculated strains using equation #3.

Conclusions

The welding process parameters were correctly determined to meet MIL-W-6858D specifications, and the minimum shearing force of 3.8 kN was confirmed via quasi-static tensile testing. Microstructure (EBSD and OM) and neutron diffraction measurements were performed to characterize the microstructure-property relationship of resistance spot welded Al6061-T6 aluminum alloy joints. The EBSD and OM scans for welds show the grain size and orientation for the fusion zone, heat affected zone, and base metal. The above results were used to create a strong foundation for residual stress measurements of an acceptable resistance spot welded joint in compliance with mentioned specifications. The neutron diffraction residual stress (NDRS) measurements

were successfully accomplished. The values of stresses did not exceed 120 MPa, which is less than half of 6061-T6 aluminum yield stress. It is significant to note that there were no significant values for residual stresses in the normal component (plain stress condition at the surface) and little variation in through thickness. Therefore, this stress component is not an engineering concern. This result is important because NDRS is a limited access, cost prohibitive, non-destructive technique which provides information about all three stresses. Although few, if any other techniques can determine σ_{33}, for this resistance spot welding application, only in-plane stress components (σ_{11}, σ_{22}) are significant. Thus, these stress components can be measured by alternate, less expensive techniques such as X-ray diffraction. No shear stresses were measured in this study.

We summarize that measurements of three-dimensional residual stresses in aluminum 6061-T6 resistance spot welded joints were performed. These reported results are unique for aluminum resistance spot welded joints due to the method used to determine bulk ("in-depth") residual stresses. Being negligible, σ_{33} stress can be disregarded in weld joint design. The results are indeed valuable to both industry and academia.

Table 4.1 Chemical composition of 6061-T6 aluminum alloy

Chemical composition (in wt.%)		Si	Fe	Cu	Mn	Mg	Cr	Zn	Ti	Other Each	Other Total	Al
Alloy 6061-T6	Max	0.8	0.7	0.4	0.15	1.2	0.35	0.25	0.15	0.05	0.15	Balance
	Min	0.4	-	0.15	-	0.8	0.04	-	-	-	-	Balance

Table 4.2 Mechanical properties specification limits of 6061-T6 aluminum alloy

Tempered	Direction	Limit	UTS (MPa)	YTS (MPa)	Elongation (%)	Density (g/cm^3)
Alloy 6061-T6	Longitudinal/Transversal	Minimum Value	290	255	12	2.7

Table 4.3 Welding conditions of 6061-T6 aluminum alloy.

Welding condition	Electrode Force (kN) Main Weld/Post-Heat	Welding Time (sec) Main Weld/Post-Heat	Welding Current (kA) Main Weld/Post-Heat	Average Nugget Size (mm)
"Nominal"	3.8/7.0	0.115/0.150	30/16	5.7

Table 4.4 Experimental Set-up.

Incident Slit Width (mm)	Incident Slit Height (mm)	Incident Slit Offset (mm)	Diffracted Slit Width (mm)	Diffracted Slit Offset (mm)	Step Size (mm)
1.5	2	40	1.5	50	0.25

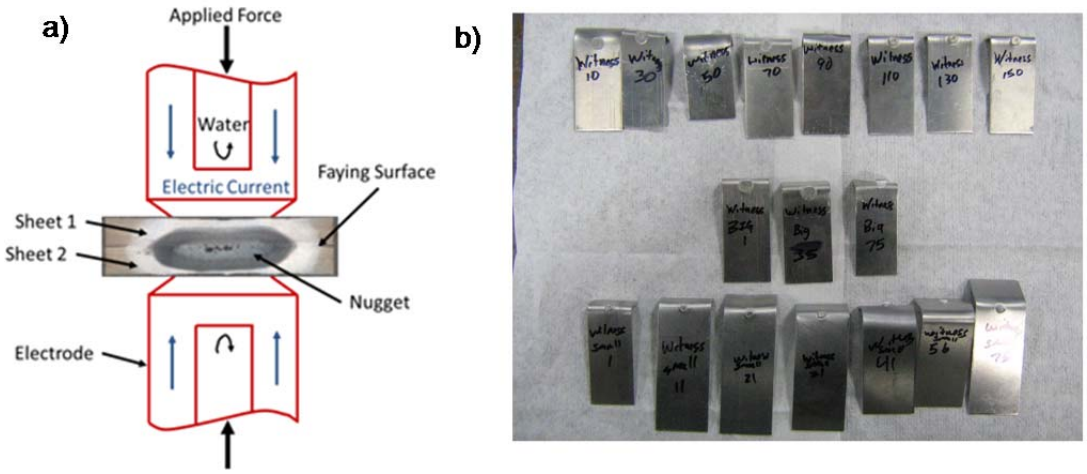

Figure 4.1 Overall view of resistant spot welding (RSW) with destructive testing

a) Schematic drawing of RSW and b) "witness peeling" samples tested during the welding process development by Florea et al. [5, 6].

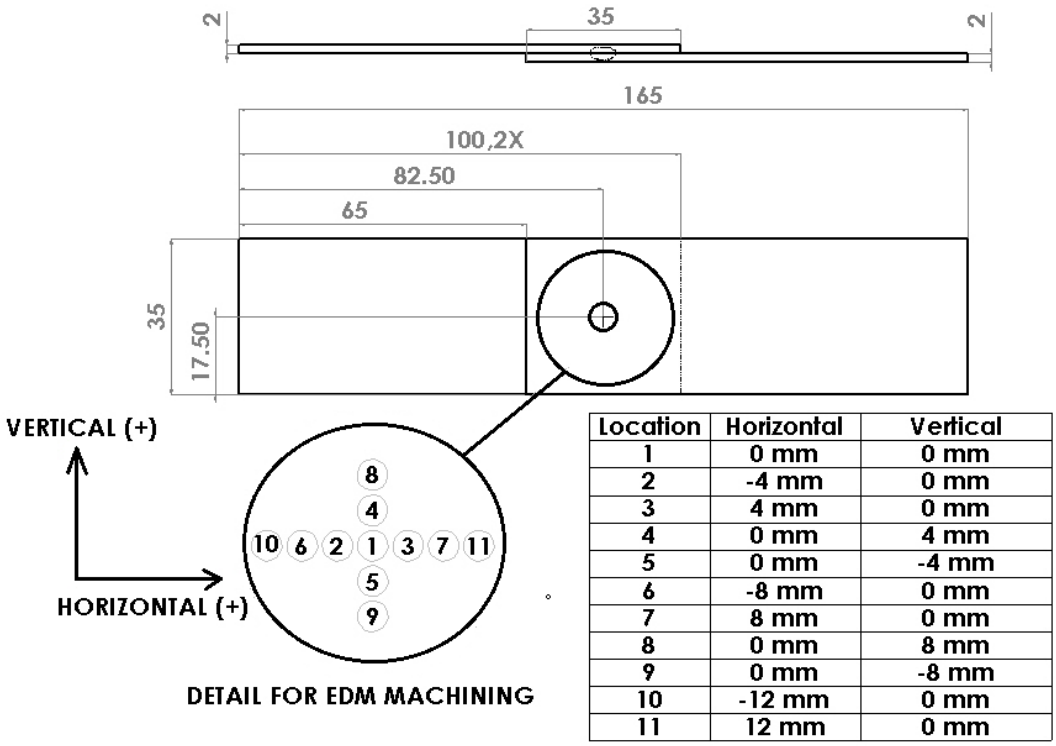

Location	Horizontal	Vertical
1	0 mm	0 mm
2	-4 mm	0 mm
3	4 mm	0 mm
4	0 mm	4 mm
5	0 mm	-4 mm
6	-8 mm	0 mm
7	8 mm	0 mm
8	0 mm	8 mm
9	0 mm	-8 mm
10	-12 mm	0 mm
11	12 mm	0 mm

Figure 4.2 Geometry of Al 6061-T6 resistance spot welded lap-shear coupon

Welding parameters were adjusted to achieve desired process quality. The horizontal axis corresponds to the rolling direction along the welded plate, while the vertical axis is against rolling direction. Dimensions are in millimeters.

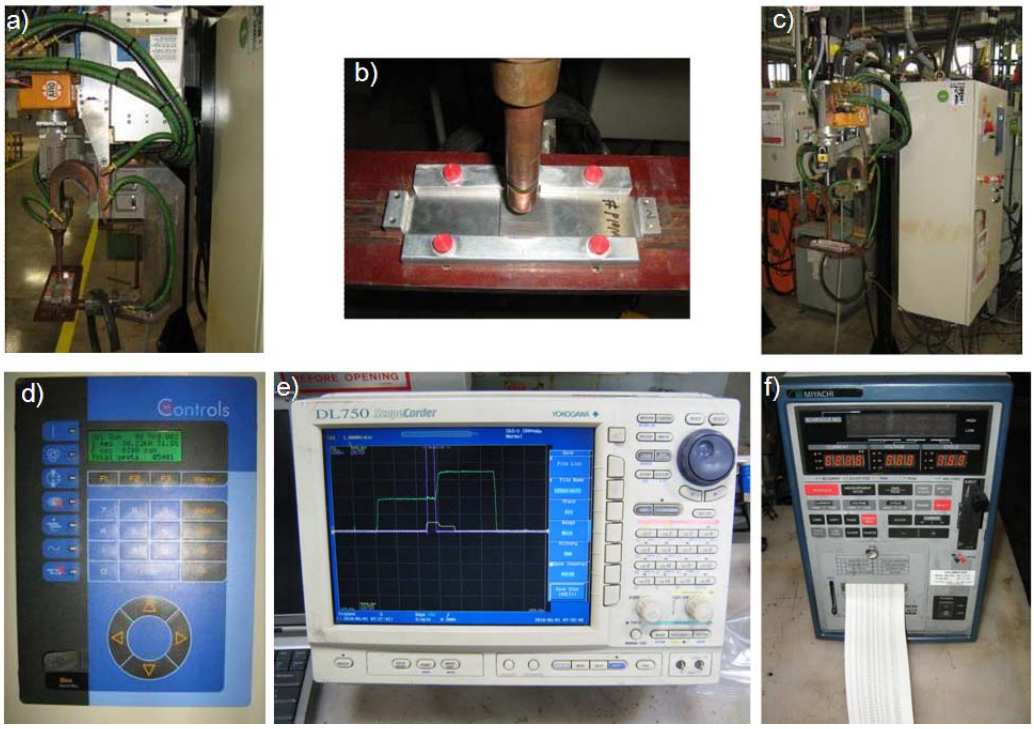

Figure 4.3 Overall view of the welding equipment

It is shown: a) and c) ARO equipment with servo-gun, b) locating fixture used to assure the specimen geometrical consistency, d) weld control, e) Yokogawa DC 750 scope-corder, and f) Miyachi weld monitor. Periodically, an electrode re-dressing was performed to assure the weld quality over the entire production run. These welds were produced at Edison Welding Institute.

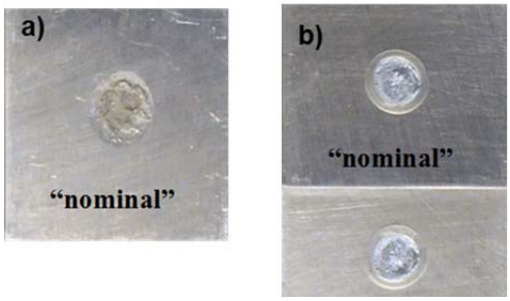

Figure 4.4 (a) An RSW'ed specimen prior to quasi-static tensile testing, and (b) subsequent fractured specimen after the quasi-static tensile test.

The failure load was about 3.8 kN with a nugget diameter of 5.7 mm.

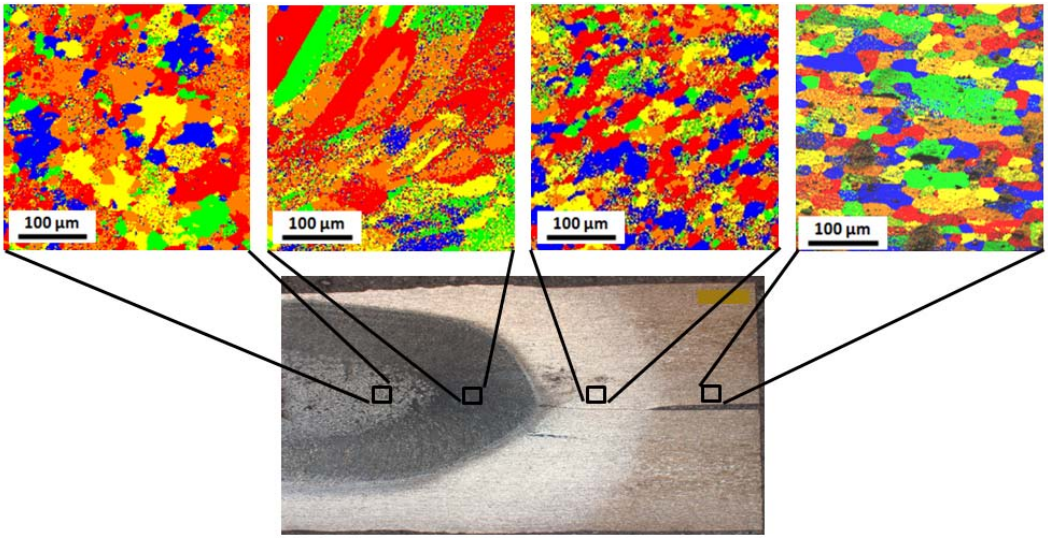

Figure 4.5 EBSD data shows grain size evolutions in the weld region.

Thermo-mechanical welding operations often involve high strains and deformation temperatures that significantly alter the materials behavior and geometrical dimension, resulting in microstructures which continually evolve away from the base of the material.

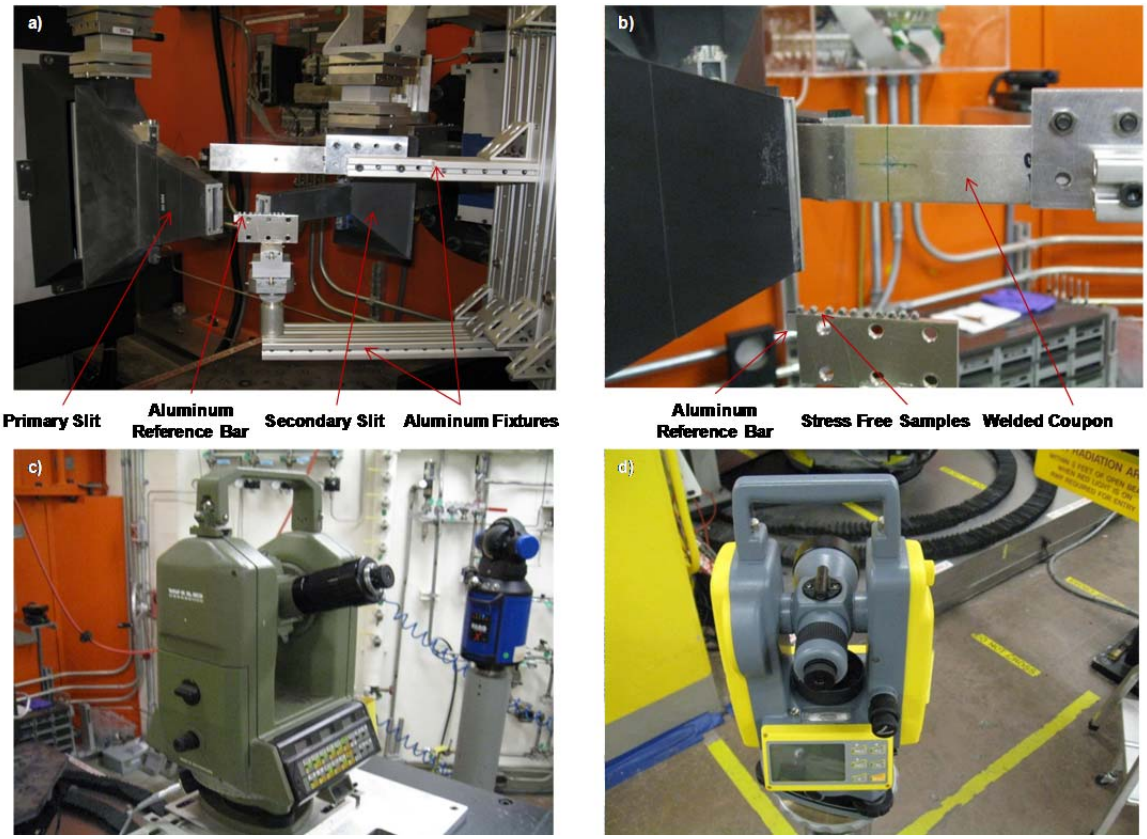

Figure 4.6 Neutron scatter diffraction equipment used to measure residual stresses

It is shown: (a) overall set-up with fixtures used to assure the specimen location, (b) detail view with welded coupon and free-stress cylinder samples and (c, d) theodolites, i.e., optical alignment devices. These measurements were carried out on the Second Generation Neutron Residual Stress Facility (NRSF2) at the HB-2B beam line on the High Flux Isotope Reactor (HFIR) at Oak Ridge National Laboratory (ORNL).

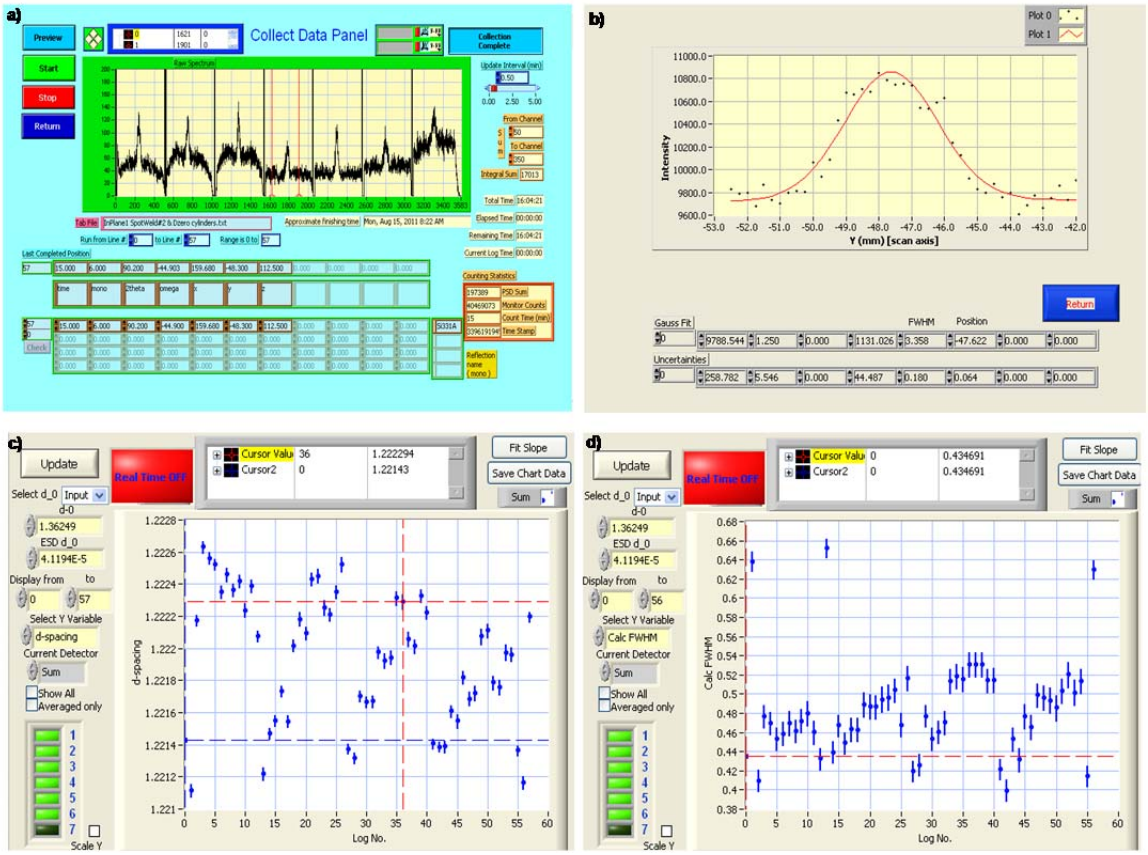

Figure 4.7 Data acquisition for neutron scatter diffraction

It is shown: (a) data collection panel; (b) Gaussian fit for mid plate coordinate location; (c, d) d-spacing illustration for measured locations within the welded coupon and zero-stress combs. Error bars, generated by programming algorithm are used for standard deviation.

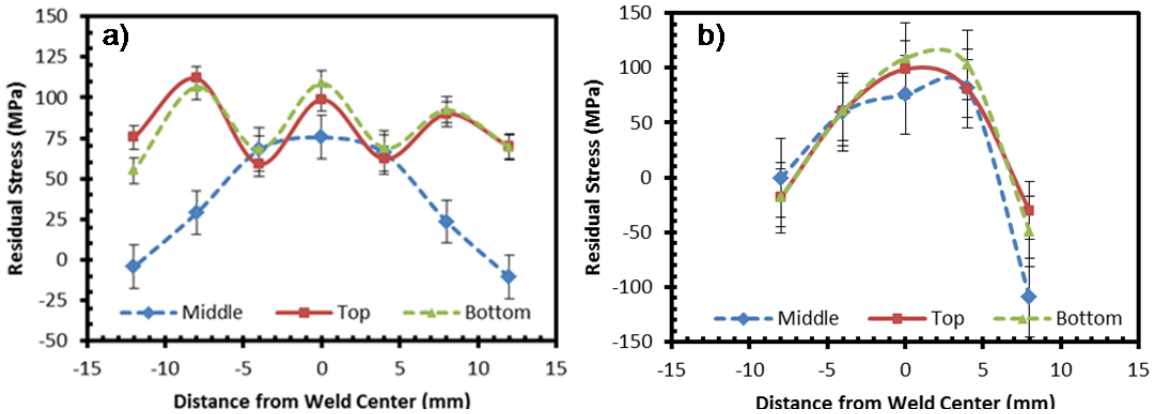

Figure 4.8 In-plane longitudinal (σ_{11}) stresses in (a) horizontal direction of the welded plate and (b) vertical direction.

This figure illustrates σ_{11} residual stresses for the three sets of thicknesses measured as follows: in the center section of the welded joint (middle), 1 mm up (top) and 1 mm down (bottom) w. r. t. the mid-plane. Total thickness of the specimen is 4 mm, and the origin of the coordinate system is the center of the weld.

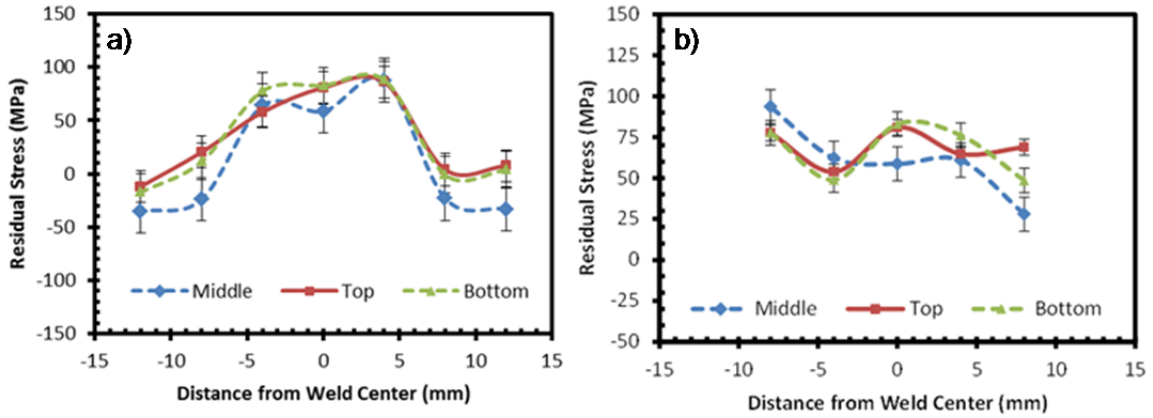

Figure 4.9 In-plane transversal (σ_{22}) stresses in (a) horizontal direction of the welded plate and (b) vertical direction.

This figure illustrates σ_{22} residual stresses for the three sets of thicknesses measured as follows: in the center section of the welded joint (middle), 1 mm up (top) and 1 mm down (bottom) w. r. t. the mid-plane. Total thickness of the specimen is 4 mm, and the origin of the coordinate system is the center of the weld.

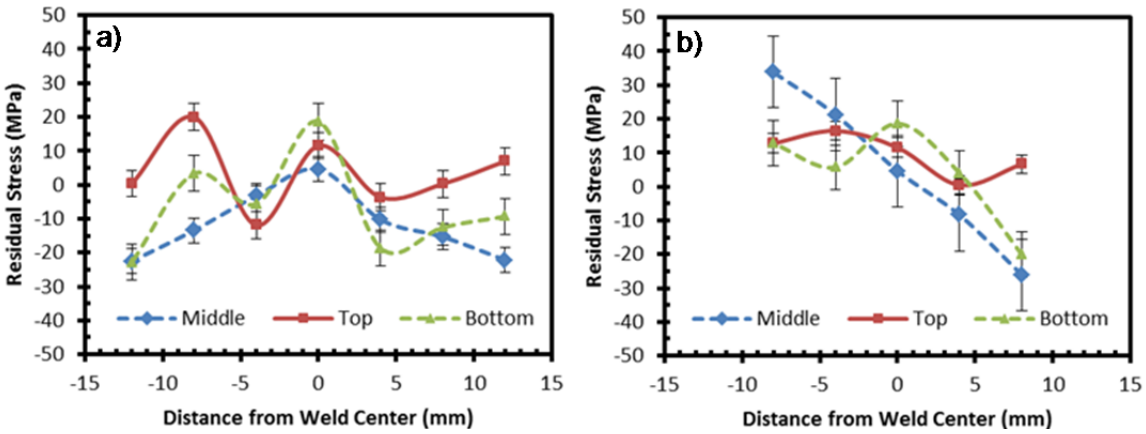

Figure 4.10 Normal (σ_{33}) stresses in (a) horizontal direction of the welded plate and (b) vertical direction.

This figure illustrates σ_{33} residual stresses for the three sets of thicknesses measured as follows: in the center section of the welded joint (middle), 1 mm up (top) and 1 mm down (bottom) w. r. t. the mid-plane. Total thickness of the specimen is 4 mm, and the origin of the coordinate system is the center of the weld.

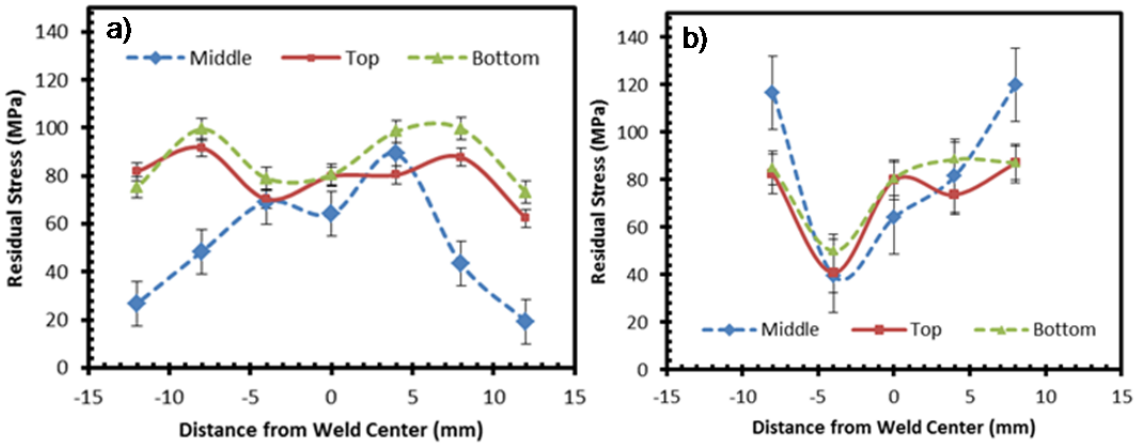

Figure 4.11 von Mises stress measurements in (a) horizontal direction of the welded plate and (b) vertical direction.

This figure illustrates "in-depth" residual stresses for the three sets of thicknesses measured as follows: in the center section of the welded joint (middle), 1 mm up (top), and 1 mm down (bottom) w. r. t. the mid-plane. Total thickness of the specimen is 4 mm, and the origin of the coordinate system is in the center of the weld.

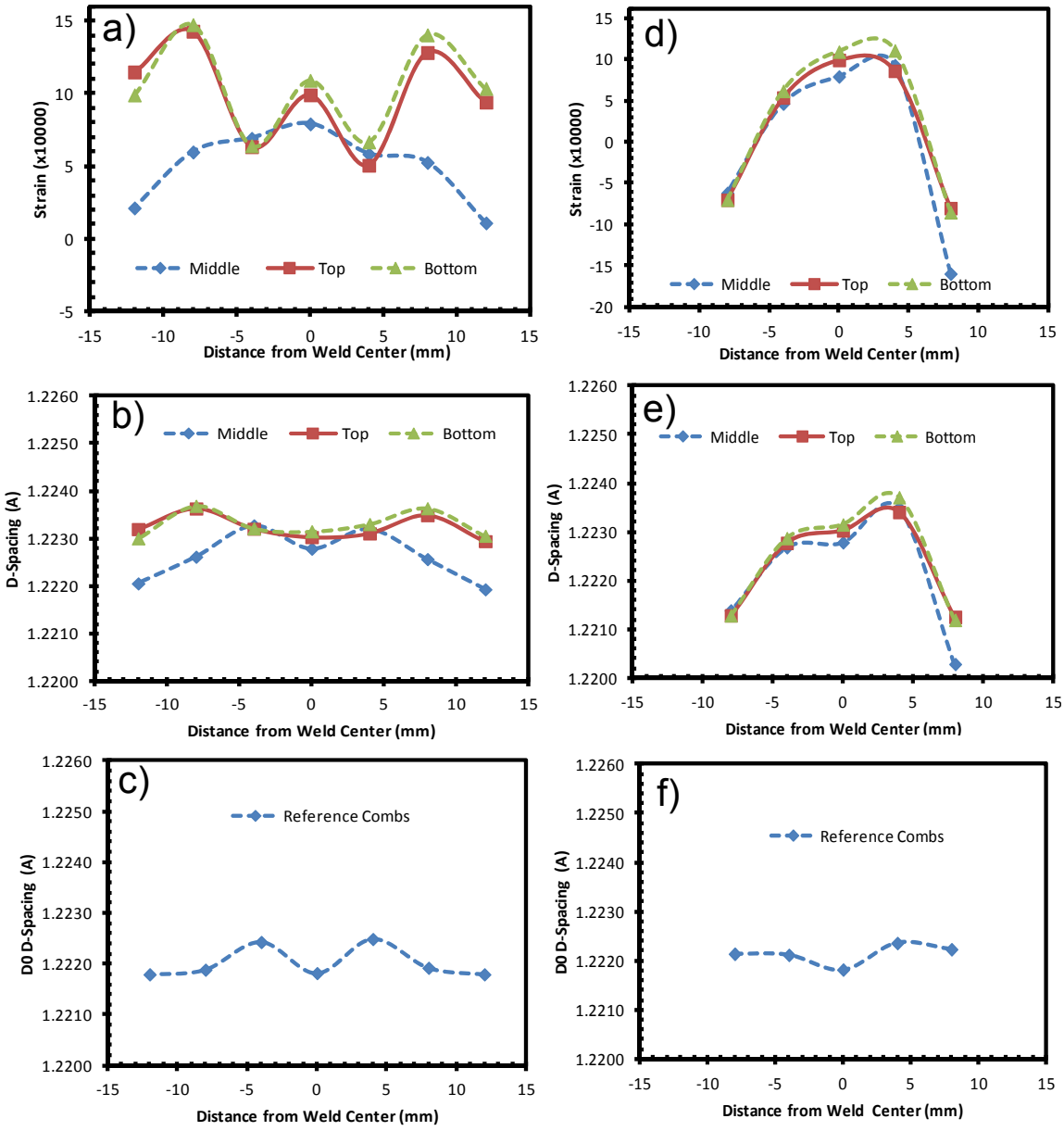

Figure 4.12 Intermediate plots for in-plane longitudinal (σ_{11}) stresses in (a-c) horizontal direction of the welded plate and (d-e) vertical direction, respectively.

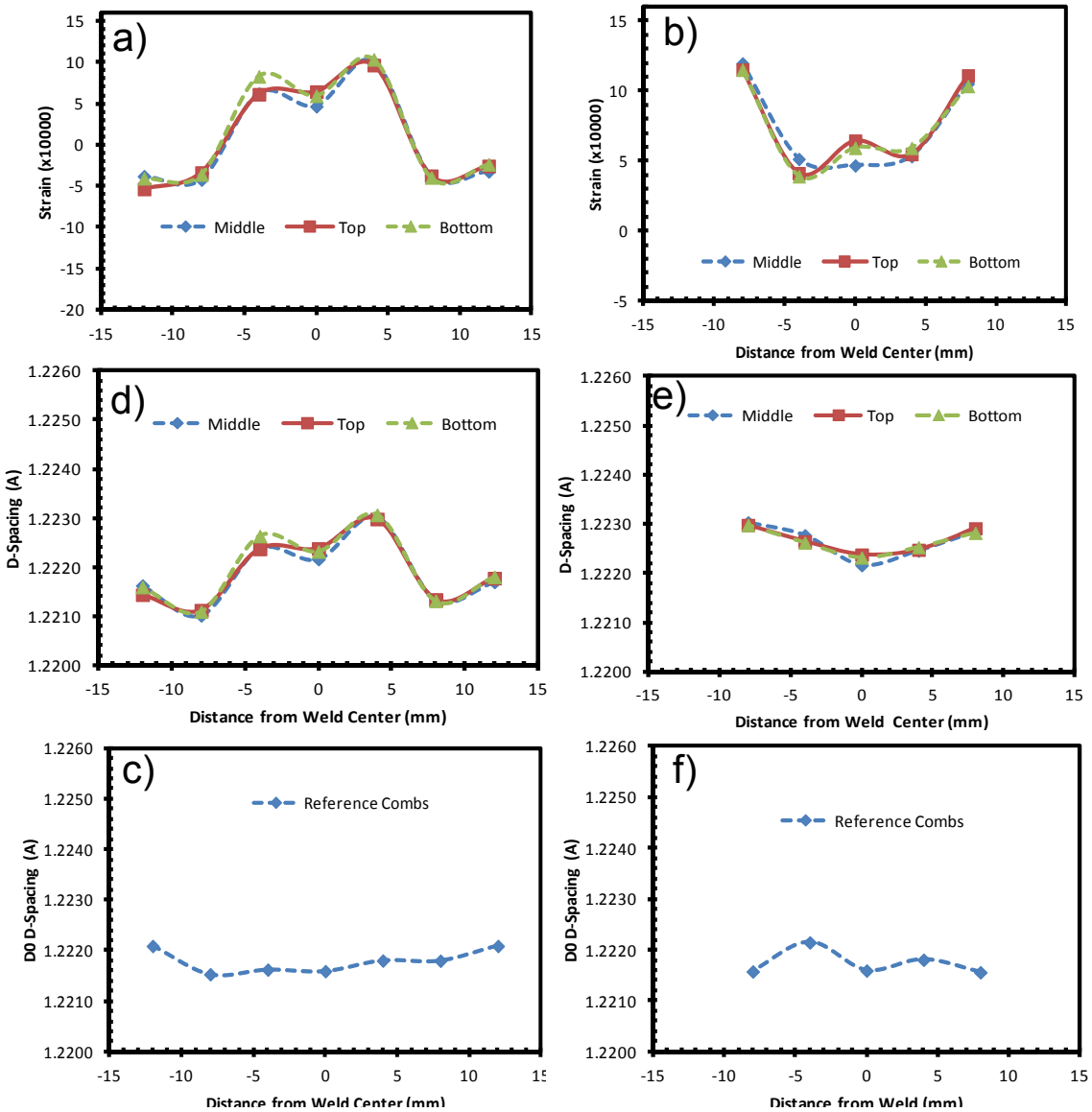

Figure 4.13 Intermediate plots for in-plane transversal (σ_{22}) stresses in (a-c) horizontal direction of the welded plate and (d-e) vertical direction, respectively.

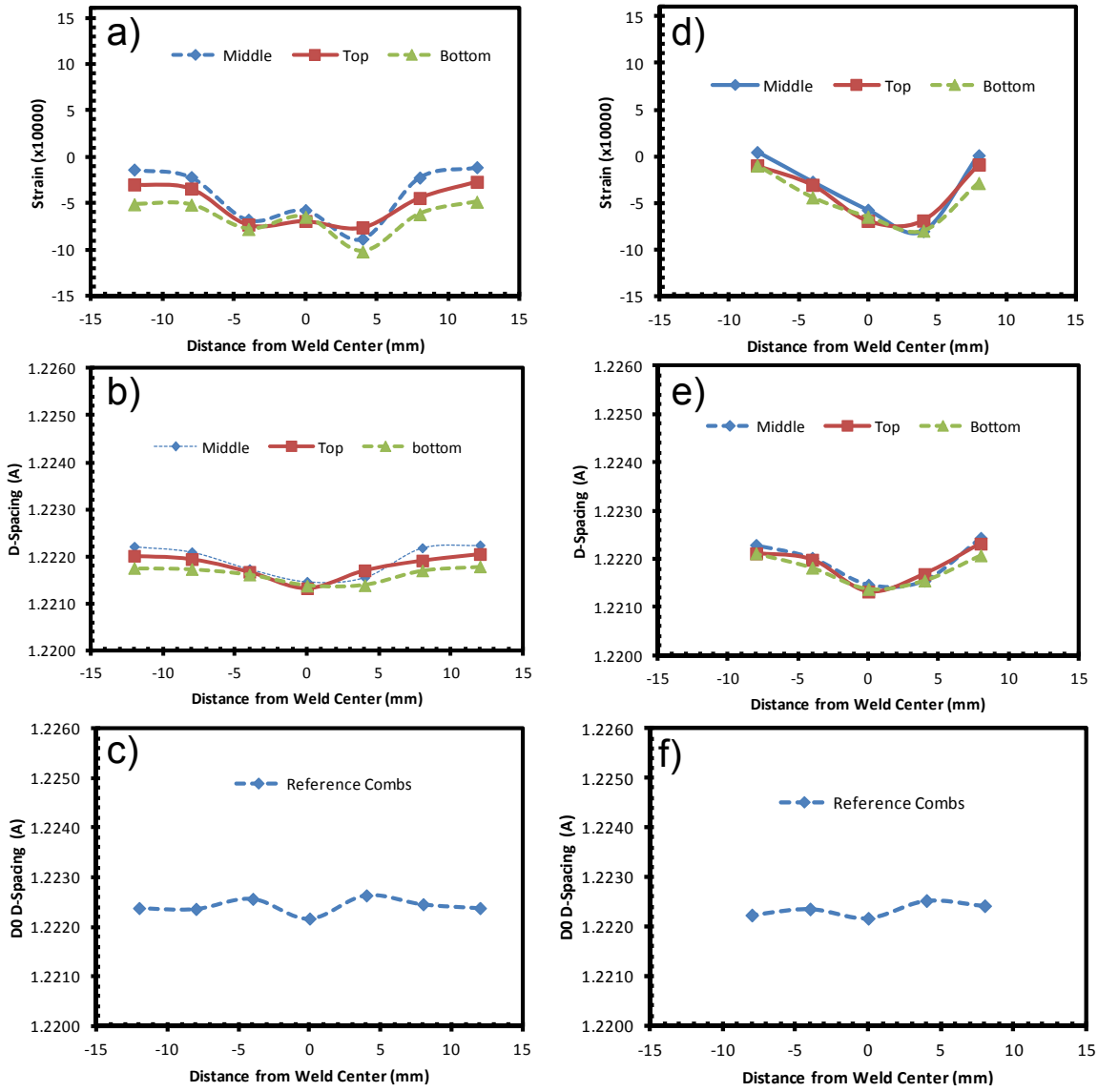

Figure 4.14 Intermediate plots for normal (σ_{33}) stresses in (a-c) horizontal direction of the welded plate and (d-e) vertical direction, respectively.

References

[1] N. T. Williams, J. D. Parker. Review of resistance spot welding of steel sheets. Part 1: Factors influencing electrode life. International Materials Reviews 2004; 49: 45-75.

[2] N. T. Williams, J. D. Parker. Review of resistance spot welding of steel sheets. Part 2: Modeling and control of weld nugget formation. International Materials Reviews 2004; 49: 77-108.

[3] American Welding Society. Specification for Automotive Weld Quality, January 2007: 1-40.

[4] S. Aslanlar, A. Ogur, U. Ozsarac, E. Ilhan. Welding time effect on mechanical properties of automotive sheets in electrical resistance spot welding. Materials & Design 2008; 29: 1427-1431.

[5] R. S. Florea, K. N. Solanki, D. J. Bammann, J. C. Baird, J. B. Jordon, M. T. Castanier. Resistance spot welding of 6061-T6 aluminum alloy-Failure loads and deformation. Materials & Design 2012; 34: 624-630.

[6] R. S. Florea, K. N. Solanki, D. J. Bammann, J. B. Jordon, M. T. Castanier. Failure loads and deformation in 6061-T6 aluminum alloy spot welds. TMS Annual Meeting 2011: 2: 213-220.

[7] R. B. Hirsch. Making resistance spot welding safer. Welding Journal February 2007: 32-37.

[8] P. J. Withers, K. D. H. Bhadeshia. Residual stress Part 1-Measurements techniques. Materials Science and Technology 2001; 17: 355-365.

[9] P. J. Withers, K. D. H. Bhadeshia. Residual stress Part 2-Nature and origins. Materials Science and Technology 2001; 17: 366-375.

[10] C. Reichert, W. Peterson. Inspecting RSW electrodes and welds with laser-based imaging. Welding Journal, February 2007: 38-45.

[11] R. A. Winholtz. In analysis of residual stress by diffraction using neutron and synchroton radiation. M.E. Fitzpatrick and A. Lodini, eds., Taylor and Francis 2003: 60-77.

[12] C. G. Shull, E. O. Wollan. X-Ray, Electron and neutron diffraction. Science 1948; 108: 69-75.

[13] P. Pratt, S. D. Felicelli, L. Wang, C. R. Hubbard. Residual stress measurement of laser-engineered net shaping AISI 410 thin plates using neutron diffraction. Metallurgical and Materials Transactions A 2008; 39A: 3155-3163.

[14] M. A. Sutton, A. P. Reynolds, D. Q. Wang, C. R. Hubbard. Residual stress analysis in 2024-T3 aluminum friction stir butt weld by neutron diffraction. Journal of Engineering Materials and Technology 2002; 124: 215-221.

[15] W. Woo, Z. Feng, W. L. Wang, D. W. Brown, B. Clausen, K. An, H. Choo, C. R. Hubbard, S. A. David. In-situ neutron diffraction measurements of temperature and stresses during friction stir welding of 6061-T6 aluminum alloy, Science Technology of Welding and Joining 2007; 12: 298-303.

[16] M. Asle Zaeem, M. R. Nami, M. H. Kadivar. Prediction of welding buckling distortion in thin wall aluminum T joint. Computational Materials Science 2007; 38: 588-594.

[17] J. A. James, J. R. Santisteban, L. Edwards, M. R. Daymond. A virtual laboratory for neutron and synchroton strain scanning. Physica B: Condensed Matter 2004; 350: 743-746.

[18] M. N. James, P. J. Webster, D. J. Hughes, Z. Chen, N. Ratel, S.-P. Ting, G. Bruno, A. Steuwer. Correlating weld process conditions, residual strain and stress, microstructure and mechanical properties for high strength steel-the role of diffraction strain scanning. Materials Science and Engineering A 2006; 427: 16-26.

[19] MIL-W-6858D 1978. Welding, resistance: spot and seam-This specification is approved for use by all Departments and Agencies of the Department of Defense, Military specification 28 March 1978: 4-5.

[20] X.-L. Wang, S. Spooner , C. R. Hubbard. Theory of the peak shift anomaly due to partial burial of the sampling volume in neutron diffraction residual stress measurements. Journal of Applied Crystals 1998; 30: 52-59.

[21] I. C. Noyan, J. B. Cohen. Residual stress measurements by diffraction and interpretation, Springer-Verlag, New York 1987: 27.

CHAPTER V

THEORETICAL AND MODELING FRAMEWORK OF 6061-T6 RESISTANCE SPOT WELDED JOINTS

Introduction

Experimental data regarding properties and behavior of various materials is necessary as input to accurately calibrate and validate models for simulating resistance spot welding. Once a computational model for a material is validated, and it can be implemented into various multiple applications, thereby eliminating the need for costly experimental iteration techniques and reducing manufacturing production costs. Accordingly, experimental results for different engineering materials have been reported by Florea, Jou, and Aslanlar [1-5], referring to the influence of the welding time, current, and applied forces. Meanwhile, Khan, Sun, Eisazadeh, and Feulvarch [6-10] used numerical and finite element analysis (FEA) methods to investigate these welding phenomena. All of these researchers faced the inherent complexities of resistance spot welding (RSW), but none gained a complete understanding of the phenomena that occurs in that welding process. Different welding processes and materials were investigated by various investigators using FEA software [11-28]. To date, the experiments, numerical solutions, and finite element calculations have yet to satisfactorily converge.

This study investigates RSW'ed joints using two commercial FEA packages: ABAQUS and COMSOL MULTIPHYSICS. Figure 5.1 illustrates the coupled problem for resistance spot welding process.

ABAQUS Preliminary Calculations

Computer-based simulations were performed using ABAQUS [29] finite element analysis (FEA) package. The ABAQUS model was made of 15,692, eight-node linear coupled thermal-electrical brick elements (DC3D8E). The coupled thermal-electrical elements are provided in ABAQUS/Standard for use in modeling the Joule heating that arises when an electrical current flows through a conductor. The coupling arises from two sources: temperature-dependent electrical conductivity and the heat generated in the thermal problem by electric conduction. Therefore, the coupled thermal-electrical elements have both temperature and electrical potential degrees of freedom. A surface current load was applied on the outer surface of the electrodes to simulate the welding process. Thermal and electrical conductivities were considered along with Joule heat fraction, material specific heat, and density. The film properties were input considering the surface interactions, gap heat generation, and gap thermal and electrical conductance. ABAQUS software describes in detail the constitutive relations for heat generation caused by electric current. Therefore, a fully coupled mechanical-electrical-thermal simulation using ABAQUS has not yet been developed.

We compared the nugget size formation with a simple ABAQUS thermal-electrical simulation (preliminary work is shown in Figure 5.2). The nugget shapes obtained by the FEA calculations are qualitatively comparable to the experimental results. The correlation between nugget shape (temperature gradients at the end of

welding time) and the cross sections of the welds at nominal condition are shown in Figure 5.3. The length of the weld nugget for the longitudinal cutaway is the same as the result obtained from the FEA simulations. The heat affected zone (HAZ) and the fusion zone (FZ) have approximately the same lengths and shapes for both the FEA simulation and the experimental results. The HAZ and FZ are more dependent upon thermo-electrical conditions than mechanical conditions, such as electrode forces or applied pressure periods. Therefore, a thermo-electrical simulation reasonably approximates only the shape of the welding nugget. Figure 5.3c shows the transversal cross section of the weld which is, as expected, smaller in length than the longitudinal one. The transversal cutaway is free of welding defects. Figure 5.3b illustrates a 1,000 micron long crack containing voids and pits in the middle of the weld. Temperatures from ABAQUS results are higher in the middle of the weld, which correlates with the same region where the welding defects were observed, as illustrated in Figure 5.3b. Trapped air at the interface of the metal parts will expand faster with temperature increments, which creates these defects. These welds are unlikely to fail, however, due to this defect because the crack is not connected to the outer part of the weld or the interface of the aluminum sheets, where most weld failures occur. Both cross sections show a good weld nugget shape and penetration. In Figure 5.3b, the weld is fused completely, from the top to the bottom plates. Understanding the temperature gradients and the influence of heating/post heating cycles on cooling rates could be used to develop resistance spot welds with minimal defects and good penetration. Thus, our future plan is to extend our FEA simulation capability by a coupled thermal-electrical-mechanical process in order to further investigate the effect of process parameters on the weld quality.

Coupled thermal-electrical-structural elements are used when a solution for the displacement, electrical potential, and temperature degrees of freedom must be obtained simultaneously. In these types of problems, coupling between the temperature and displacement degrees of freedom arises from temperature-dependent material properties, thermal expansion, and internal heat generation, which is a function of inelastic deformation of the material. The coupling between the temperature and electrical degrees of freedom arises from temperature-dependent electrical conductivity and internal heat generation (Joule heating), which is a function of the electrical current density. Coupled thermal-electrical-structural elements (Q3D8 in ABAQUS nomenclature) have displacement, electrical potential, and temperature degrees of freedom. In second-order elements the electrical potential and temperature degrees of freedom are active at the corner nodes. The main problem is that a user material model (UMAT) is not compatible at this point with these elements.

COMSOL MULTIPHYSICS Software Overview

The COMSOL software environment facilitates all steps in the modeling process by defining your geometry, meshing, specifying your physics, solving, and then visualizing your results [30]. Material properties, boundary conditions and source terms can be arbitrary functions of the dependent variables. Model set-up is quick, because this software has a number of predefined physics interfaces for applications ranging from fluid flow and heat transfer to structural mechanics and electromagnetic analyses. Predefined multi-physics-application modules can solve many common problem types. When the problem becomes more complex, additional equations are needed. COMSOL

has the capability to specify your own partial differential equations (PDEs) and link them with other equations and physics.

COMSOL gives the user complete control over definitions and use of your material properties through the Model Builder and Material Browser. Each material is represented by referenced property functions for as many as 24 key properties, dependent on temperature. These functions can be inspected by plotting and the user can add terms to them. These functions can then be used in any coupling to other physics simulations.

The LiveLink for computer aided design (CAD) software delivers the integration of CAD and finite element analysis (FEA). A change of a feature in the CAD model automatically updates the geometry in COMSOL, while retaining physics settings. All parameters specified in a CAD package can be interactively linked with your FEA geometry.

Modeling procedure using this finite element analysis package includes:

- Choose physics
- Create geometry
- specify materials
- Set sources & boundary conditions
- Mesh and solve
- Visualize or export results

The basic package includes the following modules:

- Heat transfer (convection, conduction and radiation)
- Chemical reactions (reactors, filtration and separation, mixing, reaction kinetics and complex mass transport)

- Structural analysis (linear and non-linear stress-strain analysis, thermal stresses, contact analysis and friction, buckling, creep, etc.)
- Electro-magnetics (actuators, sensors, accelerometers, transducers and piezoelectric devices)
- Computational fluid dynamics (laminar, multiphase, porous media, compressible and visco-elastic flows)
- Acoustics (speakers, microphones, transducers and mufflers)
- Customs PDE's and ODE's (the equations can be typed on designated fields with no recompiling or programming)
- AC/DC (capacitors, inductors, motors, generators, cables, sensors, etc.)

The meshing procedures in COMSOL are very well developed including different techniques:

- Various mesh algorithms (free, mapped, swept and boundary layer)
- Interactive meshing (it is the physics moving the mesh)
- Different features on meshing (copy, import, statistics, visualization, assembly and extrude/revolve of 2D meshes)

COMSOL has different ways to solve the systems matrix by direct or iterative solvers. The studies can be stationary, time-dependent (with the option to adjust time steps and tolerances). The main strengths of this software are the approach to solve a finite element problem as a multiphysics approach by:

- Coupling between different sets of equations
- Different types of couplings (segregated, weak fully coupled, fully coupled, etc.)

- Adding ordinary differential equations and coupling variables

As concluding remarks, this software can provide a good tool to analyze a multiphysics problem but has its limitations:

- There is no way to completely avoid all modeling errors
- The modular physics input has its own set of governing equations and boundary conditions
- These equations and boundary conditions approximate, usually very well, some physical case
- It is the responsibility of the user to choose a boundary condition that is a good approximation to reality
- The analyst should find and estimate the magnitude of the errors and to judge their effects upon the outcome

Theoretical Framework

The equations governing the RSW coupled thermo-electrical-mechanical multi-physics phenomena are described below. This model is used in the RSW application. To develop this theoretical framework, Bammann internal state variable constitutive model was used and RSW specific boundary conditions were applied [31-36]. These constitutive equations are part of the modular form for a thermo-electrical-mechanical analysis This model has been successfully utilized in the prediction of both the deformations and residual stresses resulting from Gas Tungsten Arc (GTA) welding simulations [37], solidification cracking during GTA welding [38] and resistance welding (both AC and DC currents) [39]. These analyses required the development of a coupled thermal-

mechanical-diffusion (carbon) code in ABAQUS, as well as an extension of the constitutive model to predict the effects of the phase transformation and the influence of carbon on the associated transformation kinetics [40]. As the first approximation Governing equation can be written as

$$\rho \frac{\partial^2 \boldsymbol{u}}{\partial^2 t} - \nabla \cdot \boldsymbol{\sigma} = \mathbf{0} \tag{5.1}$$

The prescribed displacement equation can be written can be written as

$$\boldsymbol{u} = \bar{\boldsymbol{u}} \tag{5.2}$$

Fixed constraint (zero displacement) bottom electrode can be written as

$$\boldsymbol{u} = \mathbf{0} \tag{5.3}$$

Based on the geometry of the electrodes the force (traction vector) is applied as a faced load and described by

$$\sigma \cdot \boldsymbol{n} = \boldsymbol{F} \tag{5.4}$$

Based upon a multiplicative decomposition of the deformation gradient into elastic and plastic parts, and assuming linear isotropic elasticity with respect to the natural configuration associated with this decomposition, the assumption of linear elasticity can be written as

$$\dot{\boldsymbol{\sigma}} - \boldsymbol{W^e \sigma} + \boldsymbol{\sigma W^e} = \lambda(T) tr(\boldsymbol{D^e})\mathbf{1} + 2\mu(T)\boldsymbol{D^e} + \frac{\boldsymbol{\partial \lambda(T)}}{\boldsymbol{\partial T}} \dot{T} tr(\boldsymbol{E_e})\mathbf{1} + \frac{\boldsymbol{\partial \mu(T)}}{\boldsymbol{\partial T}} \dot{T} \boldsymbol{E_e}\mathbf{1} \tag{5.5}$$

where, $\boldsymbol{D^e}$ is the elastic strain rate tensor, $\boldsymbol{C}$ is the elastic stiffness, and λ and μ the elastic Lame constants, and the Cauchy stress tensor $\boldsymbol{\sigma}$ is convected with the elastic spin $\boldsymbol{W^e}$ as

$$\widehat{\boldsymbol{\sigma}} = \dot{\boldsymbol{\sigma}} - \boldsymbol{W^e\sigma} + \boldsymbol{\sigma W^e} \tag{5.6}$$

The importance of the rate of change with elastic moduli with temperature has been clearly demonstrated for welding problems [41] due to the extremely rapid cooling that occurs during these problems. These terms are neglected since only a very qualitative solution is attempted in this work. Any quantitative simulation will require consideration of these terms, as well as similar terms in the evolution of the internal state variables (equations 5.14 and 5.15). The inclusion of these terms seriously complicates the implementation and is best resolved by casting the model into dimensionless form using temperature dependent scaling parameters [42].

Decomposing the total strain rate $\boldsymbol{D}$ into elastic and plastic parts, the elastic relation can also be written:

$$\boldsymbol{D^e} = \boldsymbol{D} - \boldsymbol{D^p} - \boldsymbol{D^{th}} \tag{5.7}$$

$$\boldsymbol{D^{th}} = \beta(T)\dot{T}\mathbf{1} \tag{5.8}$$

All bolded letters are second order tensors except the elastic stiffness, while other values on the equations are scalars.

The plastic flow rule is defined by the hyperbolic sine functional form:

$$\boldsymbol{D^p} = \begin{cases} f(T)\sinh\left[\frac{\|\boldsymbol{\sigma}-\boldsymbol{\alpha}\|-\kappa-Y(T)}{V(T)}\right]\boldsymbol{n} & if\ \|\boldsymbol{\sigma}-\boldsymbol{\alpha}\|-\kappa-Y(T)\geq 0 \\ 0 & if\|\ |\boldsymbol{\sigma}-\boldsymbol{\alpha}|\|-\kappa-Y(T)<0 \end{cases}, \tag{5.9}$$

Where $\boldsymbol{n}$ the plastic normal tensor defined by:

$$\boldsymbol{n} = \frac{\boldsymbol{s}-\boldsymbol{\alpha}}{\|\boldsymbol{\sigma}-\boldsymbol{\alpha}\|} \tag{5.10}$$

The definition of this plastic flow rule leads to a von Mises type yield function defined by

$$f = \|\boldsymbol{\sigma} - \boldsymbol{\alpha}\| - \kappa - Y(T) - V(T)\sinh^{-1}\left[\frac{\bar{d}_p}{f(T)}\right] = 0 \tag{5.11}$$

where $Y(T)$, $f(T)$ and $V(T)$ are temperature dependent functions and are related to yielding with an Arrhenius-type temperature dependence. The function $Y(T)$ is the rate-independent yield stress, the function $f(T)$ determines when the rate-dependence affects initial yielding, and the function $V(T)$ determines the magnitude of rate-dependence on yielding.

The evolution of the plasticity internal state variables is prescribed in the hardening-minus recovery format. The hardening may be defined as the increase in yield stress due to plastic deformation. Figure 5.4 illustrates the isotropic and kinematic hardening mechanisms. For hardening materials, the yield surface will evolve in space in one of three ways:

- Isotropic hardening reflects the effect of the global dislocation density. For isotropic hardening, the yield surface grows in size while the center remains at a fixed point in stress space.
- Kinematic hardening also called Bauschinger effect reflects the effect of anisotropic dislocation density. For kinematic hardening, the center of the yield surface translates in stress space, while the size remains fixed. For both isotropic and kinematic hardening, the orientation of the yield surface remains fixed.

- Mixed hardening where both isotropic and kinematic hardening characteristics are evident. For mixed hardening, the orientation (not considered here) of the yield surface may also change as well.

Although isotropic hardening is the most common form of yield surface evolution assumed in finite element models for metal forming simulation, it is not necessarily the most accurate. The mixed hardening model is most likely the most accurate of the three models. The kinematic hardening internal state variable $\boldsymbol{\alpha}$, representing the directional hardening, is defined by the evolution equation:

$$\dot{\boldsymbol{\alpha}} = h(T)\boldsymbol{D}^p - \left[r_d(T)\bar{d}_p + r_s(T)\right]\|\boldsymbol{\alpha}\|\boldsymbol{\alpha} \tag{5.12}$$

The isotropic hardening is described by

$$\dot{\kappa} = H(T)\bar{d}_p - \left[R_d(T)\ \bar{d}_p + R_s(T)\right]\kappa^2 \tag{5.13}$$

Finally,$\bar{d}_p$, equivalent plastic strain rate defined by

$$\bar{d}_p = \sqrt{\boldsymbol{D}^p : \boldsymbol{D}^p} \tag{5.14}$$

$$\|\boldsymbol{\alpha}\| = \sqrt{\frac{3}{2}\boldsymbol{\alpha} : \boldsymbol{\alpha}} \tag{5.15}$$

The temperature dependence of the hardening functions $H(T)$ and $h(T)$ should in general be proportional to the temperature dependence of shear modulus. The terms $r_s(T)$ and $R_s(T)$ are scalar functions describing the diffusion-controlled static or thermal recovery, and $r_d(T)$ and $R_d(T)$ are the functions describing the dynamic recovery. The temperature-dependent functions are defined in Table 5.1.

BCJ Implementation for COMSOL MULTIPHYSICS Finite Element Software

Mechanical Component (Solid Mechanics Module via ODE and DAE Mathematical Interfaces)

The input parameters for this model are described in Table 5.1. The model introduces these nine terms or functions to describe the inelastic response. Table 5.2 describes the material parameters for working plates and electrodes at room temperature. In COMSOL, each material has its representative properties dependent on temperature. These terms can be organized into three basic types: those associated with the initial yield, the hardening, and the recovery ones. The temperature dependence of the yield functions are described above.

The next two hardening mechanisms are illustrated in the same table and the recovery can be grouped into two basic types: dynamic and static.

The implementation of these equations in COMSOL was done in several steps using the mathematics module three times.

The model parameters are inputted in COMSOL at the beginning of the implementation followed by the equations written in component form under the small deformations assumption. The equations are for flow rule, isotropic and kinematic hardening, respectively.

The plastic strain rate in scalar form is defined by

$$\dot{\bar{\varepsilon}}_p = f(T)\sinh\left[\frac{\|\boldsymbol{\sigma}-\boldsymbol{\alpha}\|-\boldsymbol{\kappa}-Y(T)}{V(T)}\right] \tag{5.16}$$

The evolution equations for isotropic hardening in scalar form can be written as

$$\dot{\kappa} = H(T)\dot{\bar{\varepsilon}}_p - \left[R_d(T)\,\dot{\bar{\varepsilon}}_p + R_s(T)\right]\kappa^2 \tag{5.17}$$

The stress norm can be written as

$$\|\boldsymbol{\alpha}\| = \sqrt{\frac{3}{2}(\alpha_{11}^2 + \alpha_{22}^2 + \alpha_{33}^2 + 2\alpha_{12}^2 + 2\alpha_{13}^2 + 2\alpha_{23}^2)} \tag{5.18}$$

The evolution equations for conjugate variable kinematic hardening in scalar form can be written as

$$\dot{\beta}_{11} = \dot{\varepsilon}_{11}^p - \left[r_d(T)\dot{\bar{\varepsilon}}_p + r_s(T)\right]\|\alpha\|\beta_{11} \tag{5.19}$$

$$\dot{\beta}_{22} = \dot{\varepsilon}_{22}^p - \left[r_d(T)\dot{\bar{\varepsilon}}_p + r_s(T)\right]\|\alpha\|\beta_{22} \tag{5.20}$$

$$\dot{\beta}_{33} = \dot{\varepsilon}_{33}^p - \left[r_d(T)\dot{\bar{\varepsilon}}_p + r_s(T)\right]\|\alpha\|\beta_{33} \tag{5.21}$$

$$\dot{\beta}_{12} = \dot{\varepsilon}_{12}^p - \left[r_d(T)\dot{\bar{\varepsilon}}_p + r_s(T)\right]\|\alpha\|\beta_{12} \tag{5.22}$$

$$\dot{\beta}_{13} = \dot{\varepsilon}_{13}^p - \left[r_d(T)\dot{\bar{\varepsilon}}_p + r_s(T)\right]\|\alpha\|\beta_{13} \tag{5.23}$$

$$\dot{\beta}_{23} = \dot{\varepsilon}_{23}^p - \left[r_d(T)\dot{\bar{\varepsilon}}_p + r_s(T)\right]\|\alpha\|\beta_{23} \tag{5.24}$$

Plastic strain rate components can be written as

$$\dot{\varepsilon}_{11}^p = n_{11}\dot{\bar{\varepsilon}}_p \tag{5.25}$$

$$\dot{\varepsilon}_{22}^p = n_{22}\dot{\bar{\varepsilon}}_p \tag{5.26}$$

$$\dot{\varepsilon}_{33}^p = n_{33}\dot{\bar{\varepsilon}}_p \tag{5.27}$$

$$\dot{\varepsilon}_{12}^p = n_{12}\dot{\bar{\varepsilon}}_p \tag{5.28}$$

$$\dot{\varepsilon}_{13}^p = n_{13}\dot{\bar{\varepsilon}}_p \tag{5.29}$$

$$\dot{\varepsilon}_{23}^p = n_{23}\dot{\bar{\varepsilon}}_p \tag{5.30}$$

Plastic normal tensor components can be written as

$$n_{11} = \frac{3}{2}\frac{(\sigma_{11}^d - \alpha_{11})}{\|\boldsymbol{\sigma}-\boldsymbol{\alpha}\|} \tag{5.31}$$

$$n_{22} = \frac{3}{2}\frac{(\sigma_{22}^d - \alpha_{22})}{\|\boldsymbol{\sigma}-\boldsymbol{\alpha}\|} \tag{5.32}$$

$$n_{33} = \frac{3}{2}\frac{(\sigma_{33}^d - \alpha_{33})}{\|\boldsymbol{\sigma}-\boldsymbol{\alpha}\|} \tag{5.33}$$

$$n_{12} = \frac{3}{2}\frac{(\sigma_{12}^d - \alpha_{12})}{\|\boldsymbol{\sigma}-\boldsymbol{\alpha}\|} \tag{5.34}$$

$$n_{13} = \frac{3}{2}\frac{(\sigma_{13}^d - \alpha_{13})}{\|\boldsymbol{\sigma}-\boldsymbol{\alpha}\|} \tag{5.35}$$

$$n_{23} = \frac{3}{2}\frac{(\sigma_{23}^d - \alpha_{23})}{\|\boldsymbol{\sigma}-\boldsymbol{\alpha}\|} \tag{5.36}$$

Cauchy stress and Hooke's law can be written as

$$\boldsymbol{\sigma} = \begin{pmatrix} \sigma_{11} & \sigma_{12} & \sigma_{13} \\ \sigma_{21} & \sigma_{22} & \sigma_{23} \\ \sigma_{31} & \sigma_{32} & \sigma_{33} \end{pmatrix} \tag{5.37}$$

$$\boldsymbol{\sigma} = \boldsymbol{C}\colon(\boldsymbol{\varepsilon} - \boldsymbol{\varepsilon}^p) \tag{5.38}$$

Deviatoric stress components can be written as

$$\sigma_{11}^d = \sigma_{11} - \frac{1}{3}(\sigma_{11} + \sigma_{22} + \sigma_{33}) \tag{5.39}$$

$$\sigma_{22}^d = \sigma_{22} - \frac{1}{3}(\sigma_{11} + \sigma_{22} + \sigma_{33}) \tag{5.40}$$

$$\sigma_{33}^d = \sigma_{33} - \frac{1}{3}(\sigma_{11} + \sigma_{22} + \sigma_{33}) \tag{5.41}$$

$$\sigma_{12}^d = \sigma_{12} \tag{5.42}$$

$$\sigma_{13}^d = \sigma_{13} \tag{5.43}$$

$$\sigma_{23}^d = \sigma_{23} \tag{5.44}$$

The stress norm can be written as

$$\|\boldsymbol{\sigma} - \boldsymbol{\alpha}\| = \sqrt{\frac{3}{2}[(\sigma_{11}^d - \alpha_{11})^2 + (\sigma_{22}^d - \alpha_{22})^2 + (\sigma_{33}^d - \alpha_{33})^2 + 2(\sigma_{12}^d - \alpha_{12})^2 + 2(\sigma_{13}^d - \alpha_{13})^2 + 2(\sigma_{23}^d - \alpha_{23})^2]} \tag{5.45}$$

The first set of differential equations for plastic strain rate can be written as

$$e_a \frac{\partial^2 \boldsymbol{u}}{\partial t^2} + d_a \frac{\partial \boldsymbol{u}}{\partial t} = f \tag{5.46}$$

$$\boldsymbol{u} = \begin{bmatrix} \varepsilon_{11}^p & \varepsilon_{22}^p & \varepsilon_{33}^p & \varepsilon_{12}^p & \varepsilon_{13}^p & \varepsilon_{23}^p \end{bmatrix}^T \tag{5.47}$$

The source term can be written as

$$f = \begin{bmatrix} \dot{\varepsilon}_{11}^p & \dot{\varepsilon}_{22}^p & \dot{\varepsilon}_{33}^p & \dot{\varepsilon}_{12}^p & \dot{\varepsilon}_{13}^p & \dot{\varepsilon}_{23}^p \end{bmatrix}^T \tag{5.48}$$

The damping and mass coefficients can be written as

$$d_a = \begin{pmatrix} 1 & \cdots & 0 \\ \vdots & \ddots & \vdots \\ 0 & \cdots & 1 \end{pmatrix} \tag{5.49}$$

$$e_a = \begin{pmatrix} 0 & \cdots & 0 \\ \vdots & \ddots & \vdots \\ 0 & \cdots & 0 \end{pmatrix} \tag{5.50}$$

The second set of differential equations for isotropic hardening can be written as

$$e_a \frac{\partial^2 \boldsymbol{\varepsilon_{ss}}}{\partial t^2} + d_a \frac{\partial \boldsymbol{\varepsilon_{ss}}}{\partial t} = f \tag{5.51}$$

The source term can be written as

$$f = \dot{\varepsilon}_{ss} \tag{5.52}$$

The damping and mass coefficients can be written as

$$d_a = 1 \tag{5.53}$$

$$e_a = 0 \tag{5.54}$$

The third set of differential equations for kinematic hardening can be written as

$$e_a \frac{\partial^2 \boldsymbol{u}}{\partial t^2} + d_a \frac{\partial \boldsymbol{u}}{\partial t} = f \tag{5.55}$$

$$\boldsymbol{u} = [\beta_{11} \quad \beta_{22} \quad \beta_{33} \quad \beta_{12} \quad \beta_{13} \quad \beta_{23}]^T \tag{5.56}$$

The source term can be written as

$$f = \left[\dot{\beta}_{11} \quad \dot{\beta}_{22} \quad \dot{\beta}_{33} \quad \dot{\beta}_{12} \quad \dot{\beta}_{13} \quad \dot{\beta}_{23}\right]^T \tag{5.57}$$

The damping and mass coefficients can be written as

$$d_a = \begin{pmatrix} 1 & \cdots & 0 \\ \vdots & \ddots & \vdots \\ 0 & \cdots & 1 \end{pmatrix} \tag{5.58}$$

$$e_a = \begin{pmatrix} 0 & \cdots & 0 \\ \vdots & \ddots & \vdots \\ 0 & \cdots & 0 \end{pmatrix} \tag{5.59}$$

Thermal Component (Heat Transfer Module)

The definition of thermal conductivity is given by Fourier's law, which relates the heat flux to the temperature gradient. In this equation, the thermal conductivity is the proportional constant. The governing energy balance equation for heat transfer analysis can be written as

$$\rho C_p \frac{\partial T}{\partial t} + \rho C_p \boldsymbol{u_{transfer}} \cdot \nabla T = \nabla \cdot (k \nabla T) + Q \tag{5.60}$$

Where ρ is the density of the material, C_P is the specific heat, T is the temperature, Q is the internal heat generation rate, t is the time, k is the thermal expansion coefficient, and ∇ is the gradient operator.

Specific heat refers to the quantity that represents the amount of heat required to change one unit of mass of a substance by one degree. It has units of energy per mass per degree. This quantity is also called specific heat capacity.

Time dependent thermal insulation for the system (prescribed heat flux) can be written:

$$-\boldsymbol{n} \cdot (-k\nabla T) = \overline{\boldsymbol{q}} \tag{5.61}$$

Convection and radiation boundary conditions are applied to all free surfaces. Convective cooling is applied to the welding electrodes via water (room temperature) cooling system at 4 liters/minute. Heat convection takes place through the net displacement of a fluid, which translates the heat content in a fluid through the fluid's own velocity. In this case the fluid is water at room temperature.

The equation can be written as

$$\overline{\boldsymbol{q}} = h(T_{exterior} - T) \tag{5.62}$$

Heat transfer by radiation takes place through the transport of photons, which can be absorbed or reflected on solid surfaces. This includes surface-to-surface radiation, which accounts for effects of shading and reflections between radiating surfaces (it is not considered in this study being negligible).It also includes surface-to-ambient radiation where the ambient radiation can be fixed or given by an arbitrary function. The velocity gradient associated with the deformation gradient.

Emissivity is a dimensionless factor between 0 and 1 that specifies the ability of a surface to emit radiative energy. The value 1 corresponds to an ideal surface, which emits the maximum possible radiative energy.

$$\overline{\boldsymbol{q}} = \epsilon\sigma(T_{ambient}^4 - T^4) \tag{5.63}$$

Electrical Component (Electric Current Module)

The four equations for current conservation can be written can be written as

$$\nabla \cdot \boldsymbol{J} = Q_j \tag{5.64}$$

Equation (5.69) is the energy balance equation for electric current.

$$\boldsymbol{J} = \sigma \boldsymbol{E} + \frac{\partial \boldsymbol{D}}{\partial t} + \boldsymbol{J_e} \tag{5.65}$$

$$\boldsymbol{D} = \epsilon_0 \epsilon_r \boldsymbol{E} \tag{5.66}$$

$$\boldsymbol{E} = -\nabla V \tag{5.67}$$

Where $\boldsymbol{J}$ is the current density [$\frac{A}{m^2}$] and the potential was denoted by V (voltage).

Time dependent electrical insulation and the prescribed current density for the system can be written:

$$-\boldsymbol{n} \cdot \boldsymbol{J} = \bar{J} \tag{5.68}$$

Prescribed voltage for the system can be written:

$$V = \bar{V} \tag{5.69}$$

Ground for the system can be written:

$$V = 0 \tag{5.70}$$

Electrical conductivity is the inverse of electrical resistivity:

$$\sigma = \frac{1}{\rho} \tag{5.71}$$

The change in electrical resistivity is dependent upon temperature. It is linearly increasing with temperature [43]:

$$\rho = \rho_0 \ (1 + \alpha \Delta T) \tag{5.72}$$

Where ρ_0 is the electrical resistivity and the resistivity temperature coefficient was denoted by α.

COMSOL Results and Discussion

To capture the main welding process, a coupled thermo-electrical-mechanical analysis was created using COMSOL. In order to avoid compromising the study's focus, the post-heat process was not considered in this analysis. The thermal section included convective cooling, radiation and heat transfer on the entire assembly. The electrical part of this problem considered the potential, current, and insulation required for the welding application. The mechanical segment considered geometry, forces, and directions. All boundary conditions have been applied to correctly reproduce the experiments. Figure 5.5 illustrates the applied force and current during the welding process. These plots are snapshots from monitoring the welding process.

COMSOL MULTIPHYSICS has the capability to input step and analytical functions. Figures 5.6 show the current versus time, while figure 5.7 illustrates force versus time, respectively.

Temperature plots have been captured as shown in figure 5.8. Melting point for aluminum correlates with the fusion zone (FZ) in weld. Heat affected zone (HAZ) and base metal (BM) are showing on electron back scatter diffraction plot. Electric resistivity has been coded to increase with temperature and the plot maintained expected shape. Another simulation was run for steel sheets and the obtained temperature plot maintains the same shape while the melting point was reached. This software captured the multi-physics involved in this complex problem.

Figure 5.9 illustrates stress distribution in y-z and x-z planes, respectively. Weld nugget formation can be observed in both cases. The anisotropy of the aluminum rolling sheet was not considered for this study.

Figure 5.10 shows the isometric view for the temperature distribution at the end of the welding cycle.

Conclusions

The preliminary ABAQUS qualitative simulation results illustrate that the nugget shape and formation is in good correlation with the described experimental results described in the macrographs and microscopy analysis. In the future work, we plan to develop a coupled thermal-electrical-mechanical process to further investigate the effect of process parameters on the weld quality.

A very interesting result is the good correlation between the EBSD scan and the FEA temperature plots. The stress distribution in the welding nugget is realistic and is matching the experimental results.

The final goal for this combined experimental and simulation study is to create a double fully coupled mechanical-thermal-electrical FEA model (capturing the main weld along to the post-heat process) which can be implemented successfully in academia and industry to design and optimize the spot welding process by reducing expensive testing techniques.

Table 5.1 Material parameters C_i for the BCJ model.

Mechanism	Description	Term Definition
Yield Stress	Rate-Independent Yield Stress	$Y(T) = \frac{C_3(1 + \tanh[C_{19}(C_{20} - T)])}{2(C_{21} + \exp[-C_4/T])}$
	Magnitude of Rate-Dependence on yielding	$V(T) = C_1 \exp[-C_2/T]$
	Rate-Dependence on Initial Yielding	$f(T) = C_5 \exp[-C_6/T]$
Kinematic Hardening	Modulus	$h(T) = C_9 - C_{10}T$
	Dynamic Recovery	$r_d(T) = C_7 \exp[-C_8/T]$
	Static Recovery	$r_s(T) = C_{11} \exp[-C_{12}/T]$
Isotropic Hardening	Modulus	$H(T) = C_{15} - C_{16}T$
	Dynamic Recovery	$R_d(T) = C_{13} \exp[-C_{14}/T]$
	Static Recovery	$R_s(T) = C_{17} \exp[-C_{18}/T]$

Table 5.2 Material parameters for working plates and electrodes at room temperature.

Material	Welded Plates (Aluminum 6061-T6)	Copper Electrodes (MPB14ZCMW28-UNSC17200)
Density ( )	2,700	8,250
Heat Capacity at Constant Pressure [ )]	900	420
Relative Permittivity	1	1
Electrical Conductivity		
Thermal Conductivity	160	118
Young Modulus	70	128
Poisson Ratio	0.33	0.3
Thermal Expansion Coefficient		
Reference Electrical Resistivity		
Resistivity Temperature Coefficient	0.041	0.0043
Initial Temperature	294	294

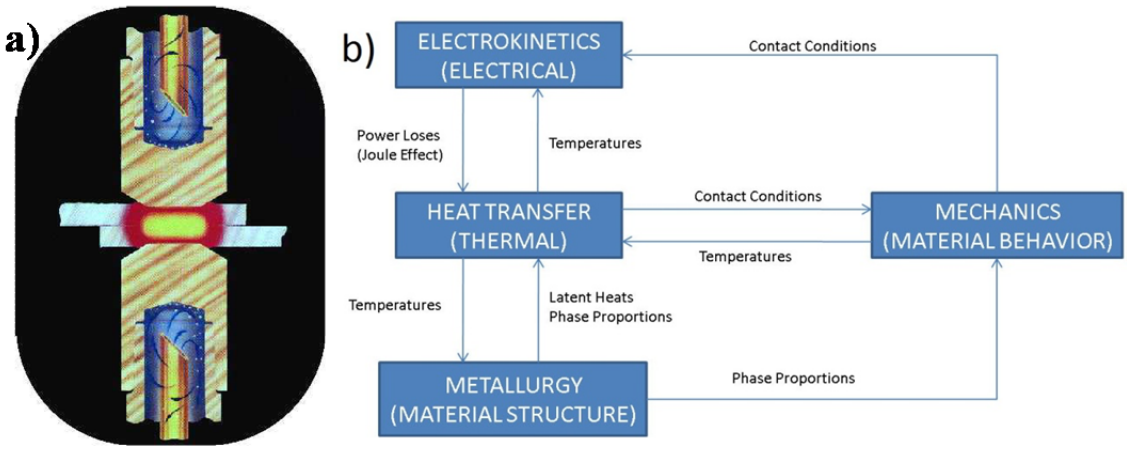

Figure 5.1 Coupled problem for resistance spot welding

It is shown: (a) welding joint along with welding electrodes and (b) overall view of resistance spot welding process.

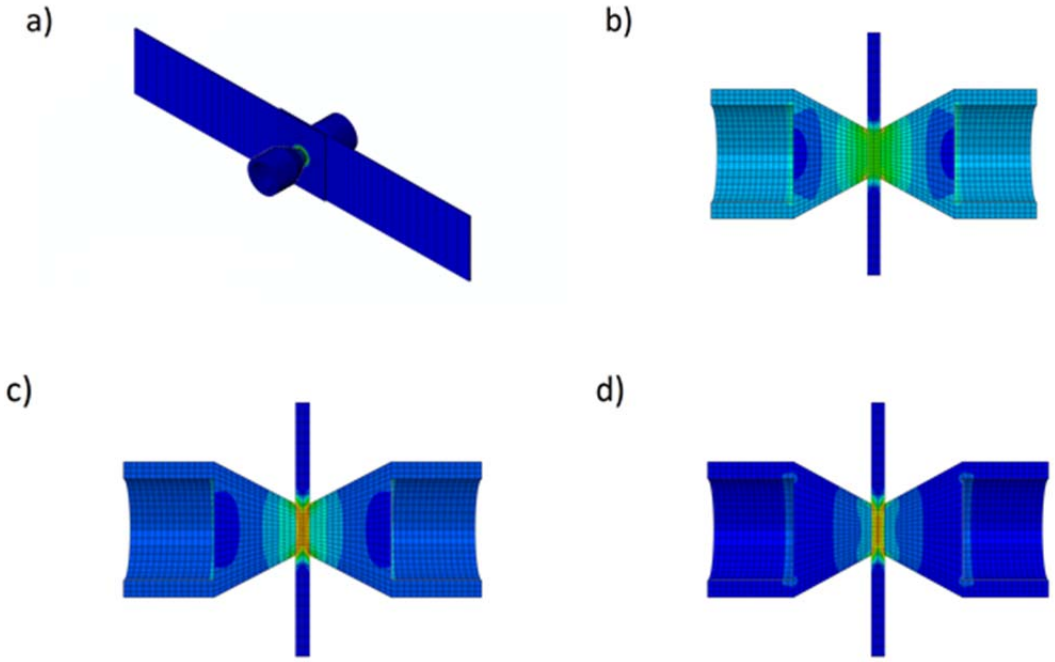

Figure 5.2 ABAQUS coupled thermo-electrical calculation of resistance spot welding.

It is illustrated (a) a perspective view of the mesh, (b) temperature distribution at $9 \cdot 10^{-6}$ s, (c) at $9 \cdot 10^{-3}$ s and (d) at 10^{-2} s respectively.

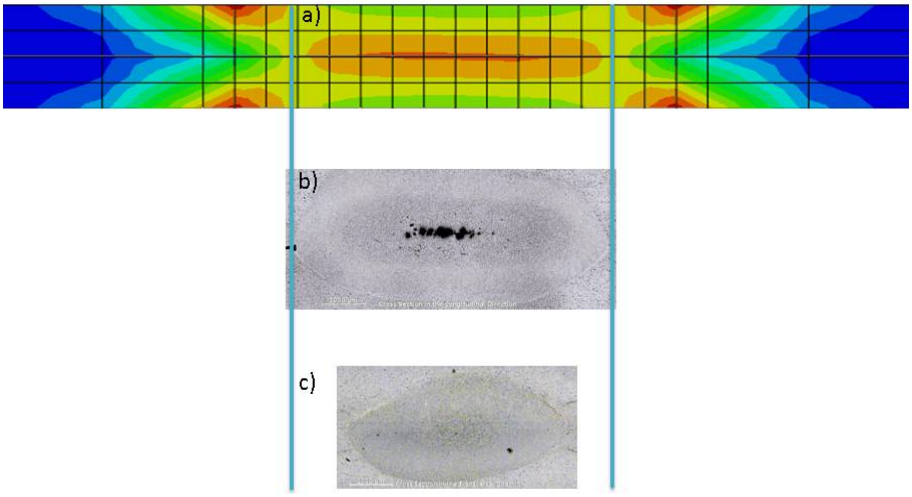

Figure 5.3 ABAQUS and experimental results.

It is shown (a) a cutaway for ABAQUS simulation for temperature gradients and (b, c) optical microscope images for cross sections of resistance spot welds in longitudinal and transversal directions.

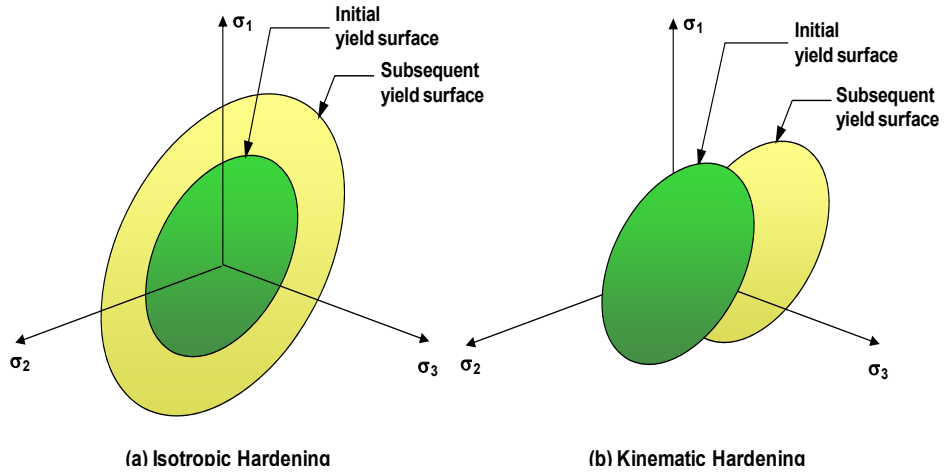

Figure 5.4 Isotropic (alpha=0) and kinematic hardening (kappa=0) schematic

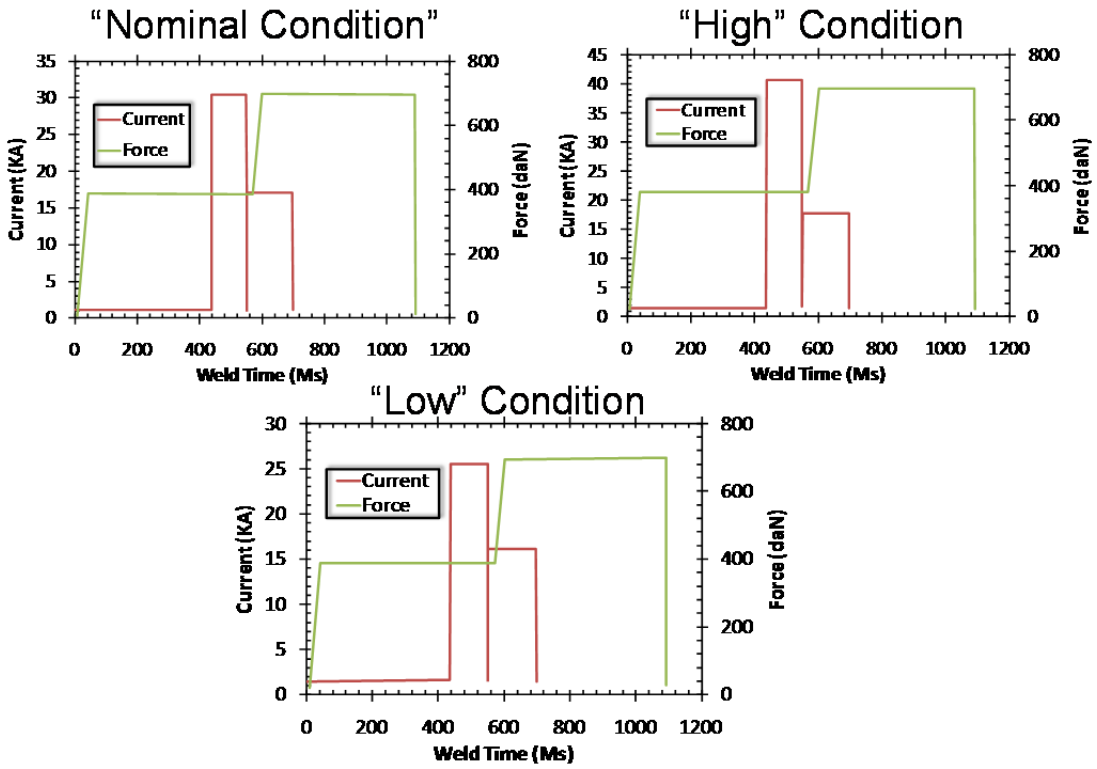

Figure 5.5 Weld parameter development (current and force traces) with corresponding microstructures for "nominal "high" and "low" conditions.

Main weld and post-heating process were performed to manufacture the specimens. Lap-shear coupons were produced by Edison Welding Institute to meet or exceed MIL-W-6858D Military Specification for "nominal condition where the minimum nugget size is 5.7 mm and minimum shearing force is 3.8 KN per weld. "Nominal" condition weld was used to determine the step functions in COMSOL.

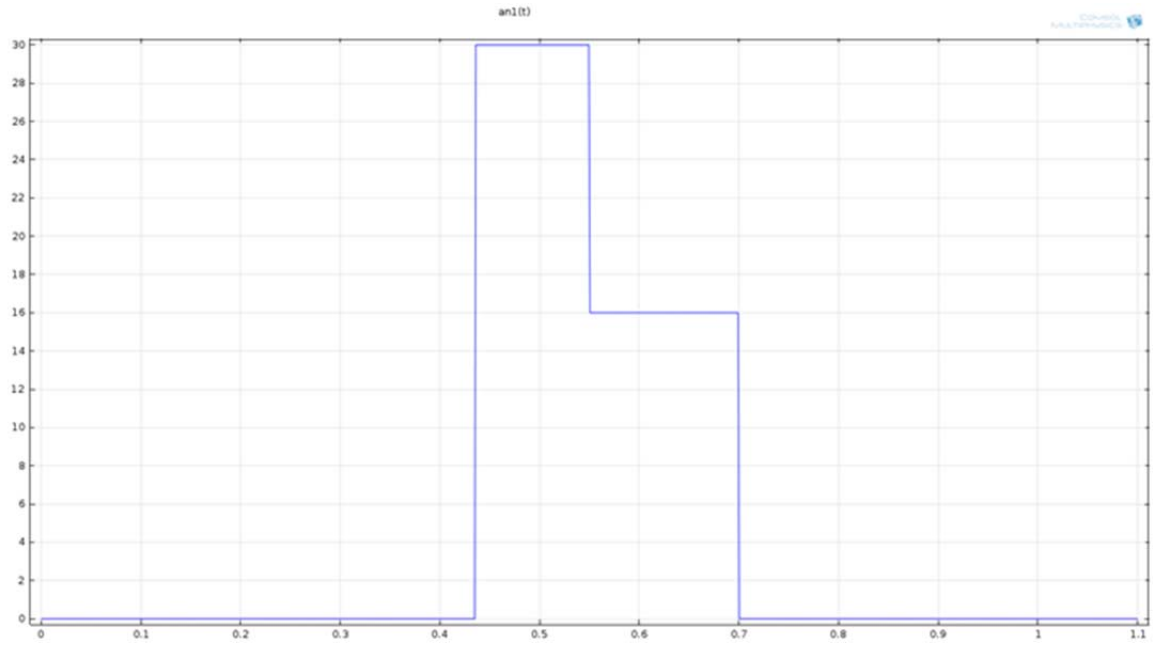

Figure 5.6 Current versus time for entire welding, annealing and cooling cycle.

This plot is created using COMSOL step and analytical functions.

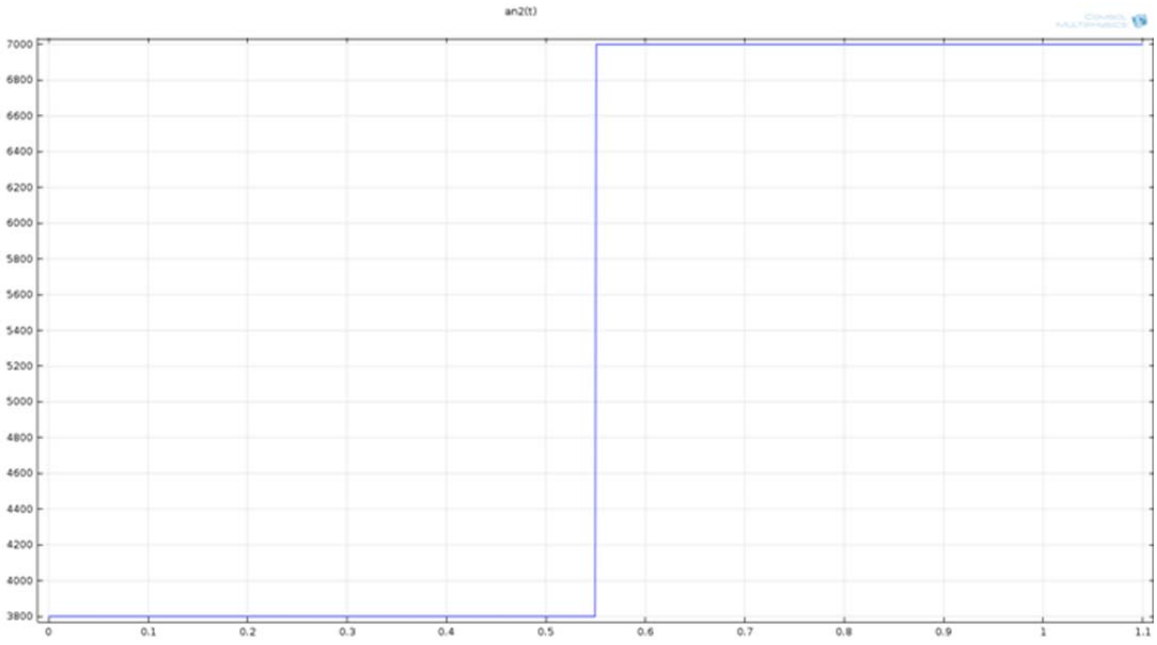

Figure 5.7 Force versus time for entire welding, annealing and cooling cycle.

This plot is created using COMSOL step and analytical functions.

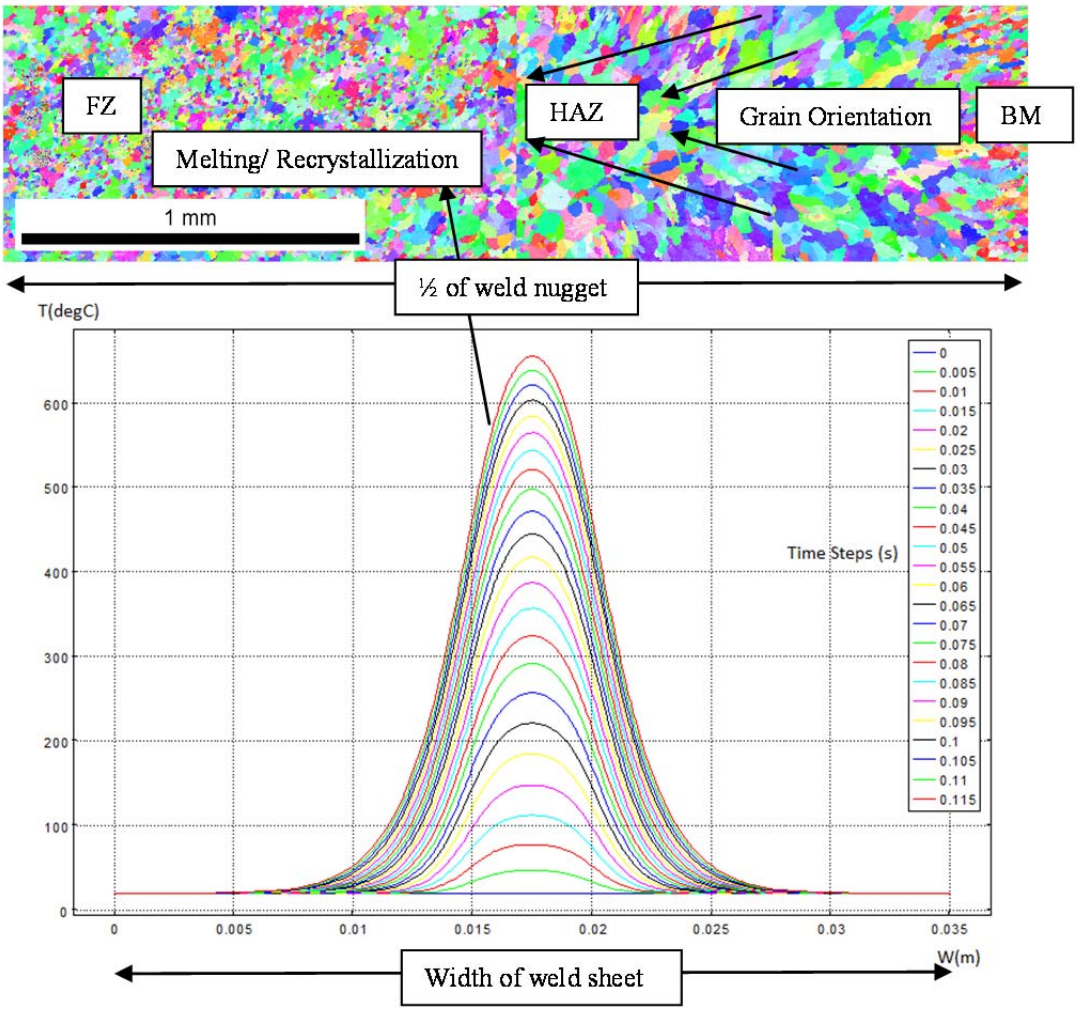

Figure 5.8 Electron back scatter diffraction grain size illustration and computer simulation (using COMSOL) temperature plots.

Melting point for aluminum correlates with the fusion zone (FZ) in weld. Heat affected zone (HAZ) and base metal (BM) are showing on electron back scatter diffraction plot.

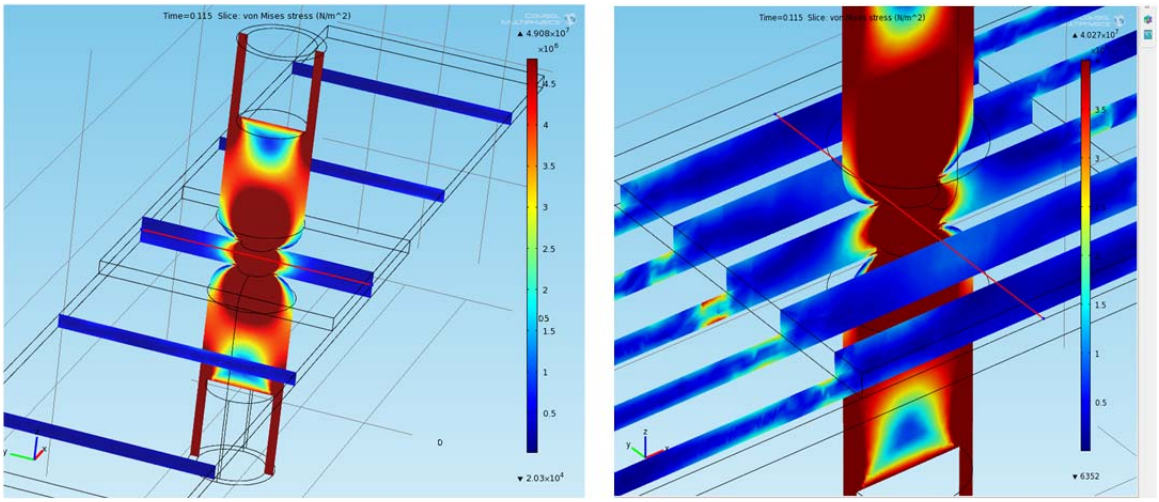

Figure 5.9 Stress distribution in y-z and x-z planes respectively.

Weld nugget formation can be observed.

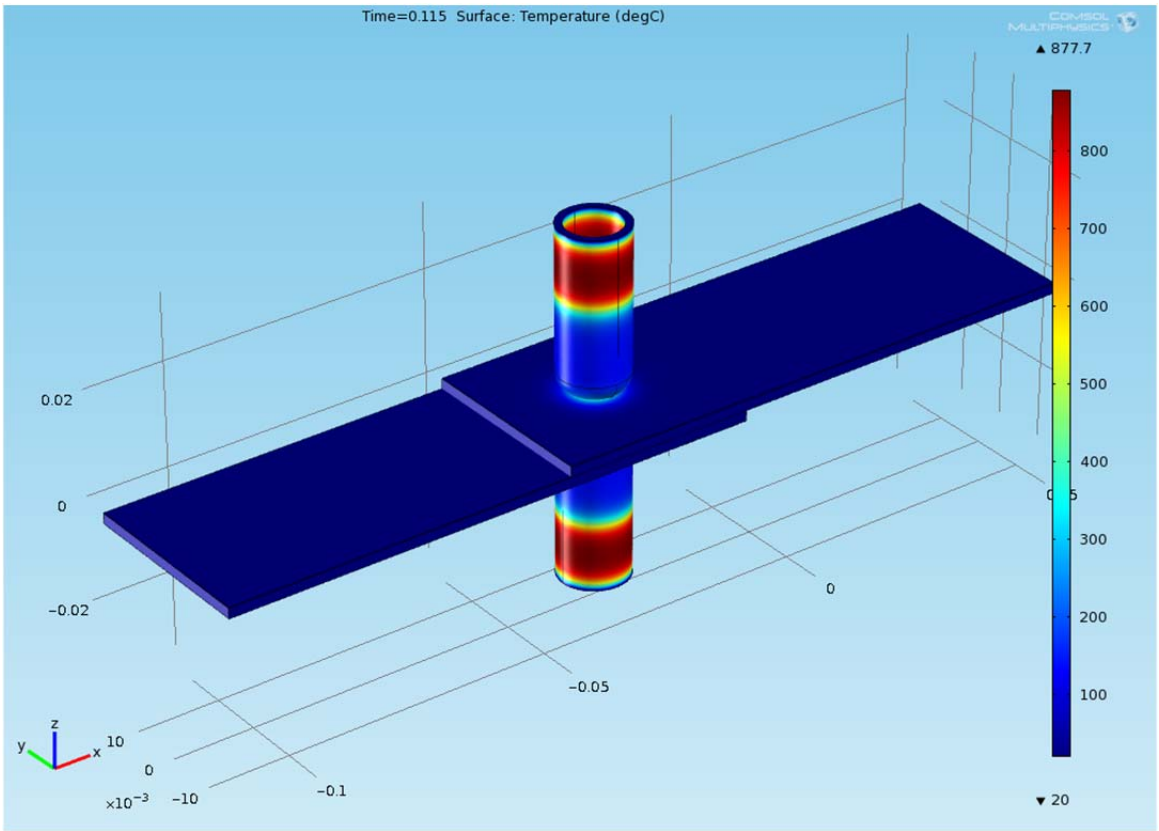

Figure 5.10 Isometric view with temperature distribution.

This plot is captured at the end of welding cycle.

References

[1] R. S. Florea et al. An experimental study of mechanical behavior of resistance spot welded aluminum 6061-T6 joints. ASME International Mechanical Engineering Congress and Exposition 2010: In Press.

[2] R. S. Florea et al. Failure Loads and Deformation in 6061-T6 Aluminum Alloy Spot Welds. TMS Supplemental Proceedings, 2: Materials fabrication, properties and characterization; February-March, 2011: 213-220.

[3] R. S. Florea et al. Resistance spot welding of 6061-T6 aluminum alloy-Failure loads and deformation. Materials & Design 2012, 34, 624-630.

[4] M. Jou. Experimental investigation of resistance spot welding for sheet metals used in automotive industry. JSME International Journal, Series C-Mechanical Systems, Machine Elements and Manufacturing 2001; 44: 544-552.

[5] S. Aslanlar, A. Ogur, U. Ozsarac, E. Ilhan. Welding time effect on mechanical properties of automotive sheets in electrical resistance spot welding. Materials & Design 2008; 29: 1427-1431.

[6] J. A. Khan., L. Xu, Y-J Chao, K. Broach. Numerical simulation of resistance spot welding process. Numerical Heat Transfer 2000; 37: 425-446.

[7] J. A. Khan, L. Xu, Y-J Chao. Prediction of nugget development during resistance spot welding using coupled electrical-thermal-mechanical model. Science and Technology of Welding and Joining 1999; 4: 201-207.

[8] X. Sun, P. Dong. Analysis of aluminum resistance spot welding processes using coupled finite element procedures. Welding Research Supplement 2000; August: 215-221.

[9] H. Eisazadeh, M. Hamedi, A. Halvaee. New parametric study on nugget size in resistance spot welding using finite element method. Materials and Design 2010; 31: 149-157.

[10] E. Feulvarch, V. Robin, J. M. Bergheau. Resistance spot welding simulation: a general finite element formulation of electro thermal contact conditions. Journal of Materials Processing Technology 2004; 153-154: 436-441.

[11] M. Asle Zaeem, M. R. Nami, M. H. Kadivar. Prediction of welding buckling distortion in thin wall aluminum T joint. Computational Materials Science 2007; 38: 588-594.

[12] S. Brauser, L. A. Pepke, G. Weber, M. Rethmeier. Deformation behavior of spot-welded high strength steels. Materials Science and Engineering A 2010; 527: 7099-7108.

[13] H. Eisazadeh, M. Hamedi, A. Halvaee. New parametric study of nugget size in resistance spot welding process using finite element method. Materials and Design 2010; 31: 149-157.

[14] H. Huh, W. J. Kang. Electrothermal analysis of electric resistance spot welding processes by a 3-D finite element method . Journal of Materials Processing Technology 1997; 63: 627-677.

[15] H. Zhigang, W. Yuanxun, L. Chunzhi, C. Chuanyao. A multi-coupled finite element analysis of resistance spot welding process . Acta Mechanica Solida Sinica 2006; 19 (1): 86-94.

[16] G. Buffa, J. Hua, R. Shivpury, L. Fratini. A continuum fem model for friction stir welding-model development . Materials Science and Engineering A 2006; 419: 389-396.

[17] M. Hamedi, H. Pashazadeh. Numerical study of nugget formation in resistance spot welding . International Journal of Mechanics 2008; 1 (2): 11-15.

[18] Z. Hou, I-S. Kim, Y. Wang, C. Li, C. Chen. Finite element analysis for the mechanical features of resistance spot welding process. Journal of Materials Processing Technology 2007; 1857: 160-165.

[19] Y. B. Li, Z. Q. Lin. Numerical analysis of magnetic fluid dynamics behaviors during resistance spot welding. Journal of Applied Physics 2007; 101 (053506): 1-10.

[20] D. Deng. FEM prediction of welding residual stress and distortion in carbon steel considering phase transformation effects. Materials and Design 2009; 30: 359-366.

[21] H. Murakawa, D. Deng, N. Ma, J. Wang. FEM prediction of buckling distortion induced by welding in thin plate panel structures. Computational Materials Science 2008; 43: 591-607.

[22] D. Deng, H. Murakawa. Application of inherent strain and interface element to simulation of welding deformation in thin plate structures. Computational Materials Science 2011; 51: 43-52.

[23] D. Deng, H. Murakawa. Finite element analysis of temperature field, microstructure and residual stress in multi-pass butt-welded 2.25Cr-1Mo steel pipes. Computational Materials Science 2008; 43: 681-695.

[24] D. Deng, H. Murakawa. Prediction of welding distortion and residual stress in a thin plate butt-welded joint. Computational Materials Science 2008; 43: 353-365.

[25] A. Traidia, F. Roger. Numerical and experimental study of arc and weld pool behavior for pulsed GTA welding. International Journal of Heat and Mass Transfer 2011; 54: 2163-2179.

[26] A. Traidia, F. Roger. A computational investigation of different helium supplying methods for the improvement of GTA welding. Journal of Materials Processing Technology 2011; 211: 1553-1562.

[27] A. Traidia, F. Roger, E. Guyot. Optimal parameters for pulsed gas tungsten arc welding in partially and fully penetrated weld pools. International Journal of Thermal Sciences 2011; 49: 1197-1208.

[28] Z. Moumni, F. Roger, N. T. Trinh. Theoretical and numerical modeling of the thermo-mechanical and metallurgical behavior of steel. International Journal of Plasticity 2011; 27: 414-439.

[29] ABAQUS Technology Brief. Welding simulation using ABAQUS. TB-05-WELD-1 2007; April: 1-3.

[30] www.comsol.com.

[31] M.F. Horstemeyer, D. J. Bammann. Historical review of internal state variable for inelasticity. International Journal of Plasticity 2010; 26: 1310-1334.

[32] D.J. Bammann, E. C. Aifantis. A damage model for ductile metals. Nuclear Engineering and Design 1989;116: 355-362.

[33] D.J. Bammann, G.C. Johnson. On the kinematics of finite-deformation plasticity. Acta Mechanica 1987; 70: 1-13.

[34] D. J. Bammann, V. C. Prantil, J.F. Lathrop. Model of phase transformation plasticity. Modeling of Casting, Welding and Advanced Solidification Processes 1995; 275-285.

[35] D. J. Bammann. Model of phase transformation plasticity. Modeling of Casting, Welding and Advanced Solidification Processes 1995; 275-285.

[36] D. J. Bammann. Modeling temperature and strain rate dependent large of metals. Applied Mechanics Reviews 1990: 43 (5): S312-S319.

[37] J. W. Foulk, A.R. Ortega, D. J. Bammann. The importance of modeling elevated temperature material response and large deformation in resistance upset welds. 7th International Numerical Analysis of Weldability Conference, Graz, Austria, September 30, 2003.

[38] J. J. Dike, J.A. Brooks, D. J. Bammann, M. Li. Finite element modeling of weld solidification cracking in 6061-T6 aluminum-applicability of strain based-failure criteria. The 2nd International Symposium on Thermal Stresses and Related Topics, Rochester Institute of Technology, Rochester, NY, June 8-11, 1997.

[39] W. S. Winters, A.A. Brown, D. J. Bammann, J. W. Foulk. Progress report for the ASCI AD resistance weld process modeling project AD2003-15. SAND2005-3000, May 2005.

[40] D. J. Bammann, V.C. Prantil, A. A. Kumar, J. F. Lanthrop, D. A. Mosher, M. Lusk, H. J. Jou, G. Krauss, W. H. Elliot. A material model for the low carbon steels undergoing phase transformations. Proceedings of the 2nd International Conference on Quenching and the Control of Distortion 1996: 367-376.

[41] J. J. Dike, J.A. Brooks, D. J. Bammann, M. Li. Thermal-mechanical modeling and experimental validation of weld solidification cracking in 6061-T6 aluminum. Proceedings of ASM International European Conference on Welding and Joining Science and Technology, Madrid, Spain, March 10-12, 1997.

[42] E. B. Marin, D. J. Bammann, R. A. Regueiro, G. C. Johnson. On the formulation, parameter identification and numerical integration of the EMMI model: plasticity and isotropic damage. SAND2006-0200, January 2006.

[43] D. R. Askeland and P.P. Phule. "The Science and Engineering of Materials" 4th Edition: 800-805.

CHAPTER VI

CONCLUSIONS AND FUTURE WORK

Publications and Summary

Peer-Reviewed Journals-Published

R.S. Florea, K.N. Solanki, D.J. Bammann, J.C. Baird, J.B. Jordon, M.P. Castanier. Resistance Spot Welding of 6061-T6 Aluminum: Failure Loads and Deformation, Materials & Design-Elsevier 2012; 34: 624-630.

R.S. Florea, C.R. Hubbard, D.J. Bammann, K.N. Solanki, W. R. Whittington, E. B. Marin. Residual Stresses in Resistance Spot Welding of 6061-T6 Aluminum Alloy Sheets via Neutron Diffraction Measurements, Journal of Materials Processing Technology-Elsevier 2012; 212: 2358-2370.

Peer-Reviewed Journals-Accepted

D.K. Francis, J. Deang, R.S. Florea, D. Gaston, N. Lee, S. Nouranian, C. Permann, J. Rudd, D. Seely, W. R. Whittington, M.F. Horstemeyer. Characterization and Failure Analysis of a Polymeric Clamp Hanger Component, Engineering Failure Analysis-Elsevier.

R.S. Florea, D.J. Bammann, A. Yedell, K.N. Solanki, Y. Hammi. Welding Parameters Influence on Fatigue Life and Microstructure in Resistance Spot Welding of 6061-T6 Aluminum Alloy, Materials and Design-Elsevier.

Peer-Reviewed Journals-Submitted

E.W. Jones, R.S. Florea, D.K. Francis. Failure of a Diesel Engine Front Gear Train, Engineering Failure Analysis-Elsevier.

R.S. Florea, L.B. Priddy, M. Asle Zaeem, A. Lowry, L. N. Williams, J. Liao, M.F. Horstemeyer . Damage Mechanisms in Blunt Carotid Artery Injuries, European Journal of Mechanics-A/Solids-Elsevier.

Peer-Reviewed Conference Papers

R.S. Florea, K.N. Solanki, D.J. Bammann, B.J. Jordon, M.P. Castanier. Failure Loads and Deformation in 6061-T6 Aluminum Alloy Spot Welds. TMS Annual Meeting 2011; 2: 213-220.

R.S. Florea, K.N. Solanki, D.J. Bammann, Y. Hammi, M.P. Castanier. An Experimental Study of Mechanical Behavior of Resistance Spot Welded Aluminum 6061-T6 Joints. ASME International Mechanical Engineering Congress and Exposition 2010, IMECE2010-39167: 37-43.

Peer-Reviewed Conference Posters

R.S. Florea, C. R. Hubbard, B. Cady, P. Cornwell, D.J. Bammann, E. Marin, M. Asle Zaeem. Neutron Diffraction Mapping for Residual Stresses in Resistance Spot Welding. ONSUM, Oak Ridge, TN, Nov, 2011 [In Press].

Peer-Reviewed Journals-In Preparation

R.S. Florea, D.J. Bammann, E.B. Marin, Y. Hammi. Numerical Analysis and Simulations of Resistance Spot Welded Joints for 6061-T6 Aluminum Alloy, Materials Science and Engineering A-Elsevier. [In Preparation]

H. Martin, R.S. Florea, E.B. Marin, M.P. Castanier, M.F. Horstemeyer. Corrosion Effects on the Tensile Strength of Resistance Spot Welded Joints for 6061-T6 Aluminum Alloy, Corrosion Science-Elsevier. [In Preparation]

R.S. Florea, C. R. Hubbard, D.J. Bammann. Welding Parameters Influence on Residual Stresses in Resistance Spot Welding of 6061-T6 Aluminum Alloy Sheets Measured via Neutron Diffraction, Journal of Materials Processing Technology -Elsevier. [In Preparation]

J. D. Bernard, R.S. Florea, H. R. Brown, M.F. Horstemeyer. Microstructure and Fatigue Properties for WELDOX and A572 Steel Plates: A Comparative Study, Materials Science and Engineering A -Elsevier. [In Preparation]

Summary

Chapter 1 is introduction, intellectual merit and an overview of the dissertation structure.

Chapter 2 of this study reveals that the welding process parameters have a great influence in the quality of the RSW joints. The optimum current, force and time for resistance spot welding 6060-T6 aluminum alloy were determined. Profilometer results clearly indicate that the larger the current, the deeper the weld imprints. As expected, the optimum quality of weld is at “nominal” condition. By slightly changing the process parameters from nominal, the profile appearances for the top and bottom of the produced welds are less than acceptable. Furthermore, it was found that the depth of the top part of the resistant spot welds varies linearly with respect to the applied electric current. Based on the quasi-static tests, we can conclude that if the welding parameters are correctly established, consistency in static failure loads is achieved. The EBSD scans for welds

show the strong dependency between the grain sizes and orientation function on the process parameters. Lower heat input created random microstructure and weaker welds, while the “nominal” and “high” conditions produced smooth transitions between the welding zones and larger failure loads. High values for the standard deviation in the “low” condition case indicate insufficient electric current and energy input to produce satisfactory welds.

In Chapter 3 is shown that the welding process parameters have a great influence upon the quality of the RSW of aluminum 6061-T6 alloy. By successive iterations and “witness samples” collected, the optimum current, force and welding time were determined. Process sensitivity was studied and summarized. The MIL-W-6858D Military Specification was met or exceeded for “nominal” and “high” welding conditions. Fatigue S-N curves is novel for this research field and can be used to characterize mechanical behavior for a 6061-T6 aluminum alloy welding joint at coupon level. The numbers of cycles to complete failure of a 2 mm lap joint were consistent at the same loading forces and ratios. Fatigue failure modes were the same when the loading conditions remained constant, but these modes changed significantly when the forces and loading ratios were changed. The welding current has a great influence on welding nugget dimensions and lap joint mechanical behavior. The number of cycles to failure ranged from approximate 6,000 to 2,000,000 cycles. Furthermore, the work presented here complements previous efforts, which together provide a good foundation for future research in the area of fatigue for aluminum resistance spot welding. No fatigue initiation sites were observed on porous area, formed from rapid solidification, in the center of the welds. All four fatigue initiation sites were experienced at the outside of the welding

button. Very visible striations next to the crack initiation sites were observed on this study. Brittle failure occurred through the center of the weld area at the end of specimen life. American Welding Society and Military standards can use data obtained from this study for extended the data base of 6061-T6 aluminum alloy resistance spot welding.

Chapter 4 describes the welding process parameters being correctly determined to meet MIL-W-6858D specifications, and the minimum shearing force of 3.8 kN was confirmed via quasi-static tensile testing. Microstructure (EBSD and OM) and neutron diffraction measurements were performed to characterize the microstructure-property relationship of resistance spot welded Al6061-T6 aluminum alloy joints. The EBSD and OM scans for welds show the grain size and orientation for the fusion zone, heat affected zone, and base metal. The above results were used to create a strong foundation for residual stress measurements of an acceptable resistance spot welded joint in compliance with mentioned specifications. The neutron diffraction residual stress (NDRS) measurements were successfully accomplished. The values of stresses did not exceed 120 MPa, which is less than half of 6061-T6 aluminum yield stress. It is significant to note that there were no significant values for residual stresses in the normal component (plain stress condition at the surface) and little variation in through thickness. Therefore, this stress component is not an engineering concern. This result is important because NDRS is a limited access, cost prohibitive, non-destructive technique which provides information about all three stresses. Although few, if any other techniques can determine σ_{33}, for this resistance spot welding application, only in-plane stress components (σ_{11}, σ_{22}) are significant. Thus, these stress components can be measured by alternate, less expensive techniques such as X-ray diffraction. No shear stresses were measured in this study. We

summarize that measurements of three-dimensional residual stresses in aluminum 6061-T6 resistance spot welded joints were performed. These reported results are unique for aluminum resistance spot welded joints due to the method used to determine bulk ("in-depth") residual stresses. Being negligible, σ_{33} stress can be disregarded in weld joint design. The results are indeed valuable to both industry and academia.

Chapter 5 is focused on theoretical and modeling workframe for resistance spot welded joints. Two finite element packages were used in order to analyze this complex problem: ABAQUS /STANDARD and COMSOL/MULTIPHYSICS.

Chapter 6 consists on conclusions, publications summary and future research directions.

Future Work

Verification and Validation of Resistance Spot Welding Coupled Multi-physics Finite Element Models

As lightweight materials such as aluminum are widely adopted in industrial use, their mechanical behavior and joining processes must be better understood and higher fidelity material models developed. The new avenues of understanding and research can be both experimental of computational. The main challenge is to verify and validate resistance spot welding models. At this time, at our best knowledge, these FEA packages cannot completely solve this welding coupled problem. According with the developers next releases will become more accurate with respect to model validation and verification. The final goal is to create a double fully coupled mechanical-thermal-electrical FEA model which can be implemented successfully in academia and industry to design and optimize the spot welding process by reducing expensive testing techniques.

Welding Parameters Influence on Residual Stresses in Resistance Spot Welding of 6061-T6 Aluminum Alloy Sheets Measured via Neutron Diffraction

The same experimental study needs to be performed for "high" and "low" welding condition. Chapter 4 quantifies residual stresses for "nominal" condition only. The data captured at Oak Ridge National Laboratory need further processing to quantify welding process parameters influence on residual stresses for RSW'ed joints.

Corrosion Effects on the Mechanical Properties of Resistance Spot Welded Joints for 6061-T6 Aluminum Alloy

Another future direction is to observe the corrosion effect on mechanical properties for welded joints such as quasi-static testing and three point bending. Currently, preliminary work was done to achieve this objective. The coupons were cut on the longitudinal direction on weld centerline in order to expose the welded material to corrosion environment.

The starting point was an immersion bath with 3.5 wt. % sodium chloride solution. The immersion exposure was 24 hours. No difference in weld strength was observed with respect to mechanical testing of specimens with no exposure at all to a corrosive environment.

Current experimentation is done with a more aggressive corrosion environment. It contains sodium chloride (5.0 wt. %), acetic acid (3.0 pH), hydrogen peroxide (0.3 vol. %) and 240 hours exposure time.

Future experiments will test some other environments and subsequent testing will be performed, such as: laser profilometry, optical microscopy and three point bending. Nondestructive testing will be periodically done after 24, 48, 96, 144, 240, and 336 hours (14 days) of exposure.

Microstructure Analysis for Fatigue Fracture Surfaces

Chapter 5 describes in detail the process development and mechanical behavior of RSW for 6061-T6 aluminum alloy. Only one sample, denoted as #36 for "nominal" condition, was analyzed with respect to fatigue failure fracture surface.

Several failure modes were observed during the fatigue experiments at different load ratios, maximum loads and three distinctive welding conditions denoted as "nominal", low" and "high". Scanning electron microscopy images need to be captured for both top and bottom welded sheets for fatigue failure sites identification. This analysis will give more information about fatigue life for these welds.